

DIPLOMA THESIS

# Coulomb scattering and ionization processes in strong laser fields

by

Sebastian Bauch

Kiel, 6th March 2008



Institut für  
Theoretische Physik und Astrophysik  
der Christian-Albrechts-Universität zu Kiel

*Supervisor/1st examiner:*

Prof. Dr. Michael Bonitz

*2nd examiner:*

---

# Contents

<b>1</b>	<b>Introduction</b>	<b>3</b>
1.1	Chapter overview . . . . .	4
<b>2</b>	<b>Atoms in laser fields</b>	<b>5</b>
2.1	Effects in laser field . . . . .	5
2.1.1	Field strengths . . . . .	5
2.1.2	Photoionization and resonant excitations . . . . .	6
2.1.3	Multi-photon ionization . . . . .	7
2.1.4	Above threshold ionization . . . . .	8
2.1.5	Strong field effects . . . . .	8
2.1.6	Higher harmonics generation . . . . .	9
2.2	Theoretical framework . . . . .	9
2.2.1	Atom-light-field interaction . . . . .	10
2.2.2	The dipole approximation . . . . .	11
2.3	Overview of theoretical approaches . . . . .	12
2.3.1	Perturbative methods . . . . .	12
2.3.2	Strong field approximation (SFA) . . . . .	13
2.3.3	Floquet states . . . . .	14
<b>3</b>	<b>Numerical method</b>	<b>15</b>
3.1	The numerical solution of the Schrödinger equation . . . . .	15
3.1.1	1D-Crank-Nicolson method . . . . .	16
3.1.2	Solving the two-dimensional Schrödinger equation . . . . .	17
3.1.3	Accuracy, stability and efficiency . . . . .	19
3.1.4	Boundary conditions . . . . .	20
3.1.5	Initial conditions . . . . .	21
3.2	Including the laser field . . . . .	23
3.2.1	The Kramers-Henneberger frame of reference . . . . .	24
3.2.2	Back and forward transformation of the Kramers-Henneberger frame . . . . .	25
3.3	Calculation of expectation values . . . . .	26
3.4	Energy spectra . . . . .	27
3.4.1	Free particle spectrum . . . . .	27
3.4.2	Detecting scattered particles . . . . .	27
3.4.3	Comparison between both methods . . . . .	28
3.5	Implementation in C . . . . .	29
<b>4</b>	<b>Numerical concepts and basic calculations</b>	<b>31</b>
4.1	Convergence behavior of the CN-Method . . . . .	31
4.1.1	1D harmonic oscillator . . . . .	31
4.1.2	2D harmonic oscillator . . . . .	34
4.2	Wave packet scattering . . . . .	34
4.2.1	Method . . . . .	34

## Contents

4.2.2	Simple application: the potential well . . . . .	35
4.3	The regularized Coulomb potential . . . . .	36
4.3.1	Transmission and reflection . . . . .	36
4.3.2	1D eigenstates . . . . .	37
4.3.3	2D eigenstates . . . . .	40
<b>5</b>	<b>Excitation and ionization in laser fields</b>	<b>43</b>
5.1	Weak laser fields . . . . .	43
5.1.1	Excitation of the harmonic oscillator . . . . .	43
5.1.2	Excitation and ionization phenomena of the 1D Coulomb potential . . . .	44
5.1.3	Angle-resolved electron spectra . . . . .	47
5.2	Above threshold ionization (ATI) . . . . .	54
5.2.1	TDSE solution for a 1D model atom . . . . .	54
5.2.2	Comparison with the strong field approximation (SFA) . . . . .	55
5.2.3	Angle-resolved 2D ATI spectra . . . . .	56
5.3	Scattering with slow electrons . . . . .	58
<b>6</b>	<b>Coulomb scattering</b>	<b>61</b>
6.1	Coulomb scattering in a one-dimensional model . . . . .	61
6.1.1	Single ion collisions . . . . .	62
6.1.2	Instantaneous Coulomb collisions . . . . .	64
6.1.3	Scattering on ion pairs: resonance phenomena . . . . .	65
6.1.4	Scattering on chains of Coulomb potentials . . . . .	67
6.2	Two-dimensional Coulomb scattering . . . . .	70
6.2.1	Coulomb scattering without a laser field . . . . .	71
6.2.2	Including laser fields . . . . .	74
6.2.3	Scattering on one ion in a strong laser field . . . . .	74
6.2.4	Scattering on an ion pair . . . . .	78
6.2.5	Scattering in a confined setup . . . . .	80
<b>7</b>	<b>Conclusions and outlook</b>	<b>85</b>
<b>A</b>	<b>Conversion of atomic units</b>	<b>89</b>
<b>B</b>	<b>Frequently used abbreviations</b>	<b>91</b>
<b>C</b>	<b>The Schrödinger equation in the Kramers-Henneberger coordinate frame</b>	<b>93</b>
<b>D</b>	<b>Strong field approximation for 1D Coulomb ionization</b>	<b>95</b>
<b>E</b>	<b>Proof of the 1D-non-degeneracy theorem</b>	<b>97</b>

# 1 Introduction

The effect of a laser (or light) field on atoms or, more general, matter is an intensively studied field in physics. It all started with the famous explanation of the photo effect by A. Einstein 1905 [1] who used the quantum hypothesis of Planck [2] - the birth of modern physics and quantum mechanics. With the construction of the first laser by Maiman in 1960, a high-intensity radiation source with monochromatic character became available which soon led to a wide range of applications and newly discovered effects resulting from the interaction between photons and any kind of matter exposed to it. Still this field shows a fast developing dynamics. Especially the improvements achieved in laser technology during the last decades [3] play an important role. The first experiments exploring non-linear optical effects due to multi-photon absorption mechanisms were performed in the early 1970s with nanosecond pulses where the pulse form could be described only on a statistical level [4]. In contrast, recently developed laser systems are able to produce pulses with only a few optical cycles with a well-defined, stabilized and controllable carrier-envelope (CE) phase [4, 5]. Powerful new high-intensity radiation sources, such as the X-ray free-electron laser (X-FEL), give access to new intensity regimes and the arising effects are far from being understood. State-of-the-art two-color photoemission experiments in pump-probe-like setups, where a few-cycle infrared (IR) pulse is combined with an extreme ultraviolet (XUV) pulse in the attosecond regime, allow for the investigation of time-dependent dynamics of electronic excitations [6, 7]. Recently, it became possible to measure the ionization and rescattering process of an electron time-resolved with the help of such attosecond pulse trains (APT) [8]. Furthermore widely used higher-harmonics generated (HHG) vacuum ultraviolet (VUV) pulses offer the possibility to investigate surface dynamics on the femtosecond scale which has been actively studied during the last years [9].

These newly developed techniques lead to an increasing interest for precise and time-resolved quantum theories. The objective of the present thesis is to implement a method based on the numerical solution of the time-dependent Schrödinger equation (TDSE). It allows for the investigation of ionization, emission and scattering processes in (strong) laser fields on a microscopic level within the one-particle picture. The first central part of the thesis at hand is dedicated to non-linear optical effects, e.g., the above threshold ionization in strong laser fields and the corresponding angle-resolved photoemission spectra. Secondly, Coulomb scattering in strong laser fields will be addressed. Both phenomena are strongly related as can be seen for instance in the mechanism of HHG. Being motivated by the work of H.-J. Kull et al. [10, 11, 12] and the prediction of anomalous high-intensity HHG by electron-ion collisions in plasmas [13], the aim is to find a mechanism to use correlated scattering processes on the nanometer scale to generate a distribution of laser-accelerated fast electrons. A mechanism recently used in table-top sources for the generation of fast electrons is known as wake field acceleration where electrons “surf” on the plasma wake field wave [14].

Finally, as a briefly mentioned outlook, the implemented techniques and acquired experiences can be used as a benchmark for further, more enhanced approaches, such as the non-equilibrium Green’s functions [15], which may help to explore correlated many-body effects like for instance the prominent rescattering knee observed in double-ionization spectra of Helium [16, 17].

## 1.1 Chapter overview

The present work is organized as follows:

- **Chapter 2** gives an overview on fundamental processes in strong laser fields and their theoretical treatment based on the classical field-atom-interaction Hamiltonian. Central are the discussion of the TDSE and the most common approximations for its analytical solution such as time-dependent perturbation theory and the strong field approximation (SFA).
- **Chapter 3** contains a detailed discussion of the numerical treatment of the TDSE on spatial grids by implementation of the Crank-Nicolson method and the alternating direction implicit technique. The treatment of the laser field, the calculation of observables and the construction of initial conditions are of special interest.
- **Chapter 4** introduces centrally used approaches as, e.g., the wave packet formalism and the representation of the Coulomb potential on numerical grids. In addition the convergence behavior of the implemented techniques presented in Chapter 3 is addressed.
- **Chapter 5** deals with one main topic of the present thesis: ionization and excitation processes in laser fields. Low-intensity as well as strong-field processes are discussed on the basis of one- and two-dimensional model systems where the latter gives access to angle-resolved photoemission spectra of single model atoms. The results of TDSE calculations are compared to other common approaches. The chapter ends with a discussion of scattering processes of slow electrons on ions which leads over to the next part.
- **Chapter 6** discusses a further central issue, the scattering of electrons on spatially correlated positively charged ions in the presence of a strong laser field with the objective to demonstrate the generation of fast electrons. The underlying mechanisms are illustrated in model systems in terms of single-ion collisions considering TDSE simulations and classical approaches. This helps construct improved scattering setups which finally leads to two-dimensional correlated electron scattering on ions in externally confined systems.
- **Chapter 7** gives a summary of the results. It further discusses questions that arose during the work on the thesis at hand. They form the starting point for future investigations.

## 2 Atoms in laser fields

This chapter introduces effects that occur if atoms are exposed to time-dependent electromagnetic radiation. The classification of the light field strength in terms of the Keldysh parameter  $\gamma$ , Eq. (2.5), is followed by a phenomenological introduction to ionization and excitation phenomena. First, weak fields and single-photon processes are considered being followed by a quantitative discussion of multi-photon (MP) processes, above threshold ionization (ATI) and related phenomena, such as higher harmonics generation (HHG).

The next section concentrates on the theoretical treatment of the electro-magnetic field and its coupling to the Hamilton operator. Different gauges and the dipole approximation are outlined. A discussion of several approximative approaches to ionization and excitation processes, i.e., the time-dependent perturbation theory for low-intensity pulses and the *strong field approximation* (SFA) developed by Keldysh, Faisal, Reiss and others, concludes this chapter. More special methods like quasi-energy states (QES) are briefly mentioned.

### 2.1 Effects in laser field

Atoms, i.e., bound electrons in an (ionic) Coulomb-like potential, react on external electric and magnetic fields due to their charge  $e$ . The following part will give an overview on the most prominent effects caused by this interaction.

#### 2.1.1 Field strengths

First of all it is important to characterize the different regimes of laser field strengths. Clearly, the ionization potential of the atom  $I_p$  (cf. Fig. 2.2) and the field induced external potential energy have to be connected. The latter one is the *ponderomotive* energy  $U_p$  which is defined as the energy a free electron contains in its quiver motion caused by a changing electric field. If this additional energy is small compared to the binding energy, the perturbing field is small, otherwise we speak of a strong field. The Newtonian equations of motion offer the simplest approach for an estimation of  $U_p$ . The result of a quantum calculation is given at the end of this chapter. The electrical force acting on an electron with mass  $m_e$  and charge  $e_0$  in a monochromatic electric field with the frequency  $\omega$  and the amplitude  $E_0$  is given by

$$m_e \frac{d^2}{dt^2} r(t) = e_0 E_0 \cos(\omega t). \quad (2.1)$$

By integration one obtains the quiver velocity

$$v(t) = \frac{e_0}{m_e} \cdot \frac{E_0}{\omega} \sin \omega t = v_0 \cdot \sin \omega t. \quad (2.2)$$

Thus the kinetic energy of the electron evaluates to

$$E_{\text{kin}}(t) = \frac{1}{2} m_e v(t)^2 = \frac{e_0^2}{2m_e} \frac{E_0^2}{\omega^2} \sin^2(\omega t). \quad (2.3)$$

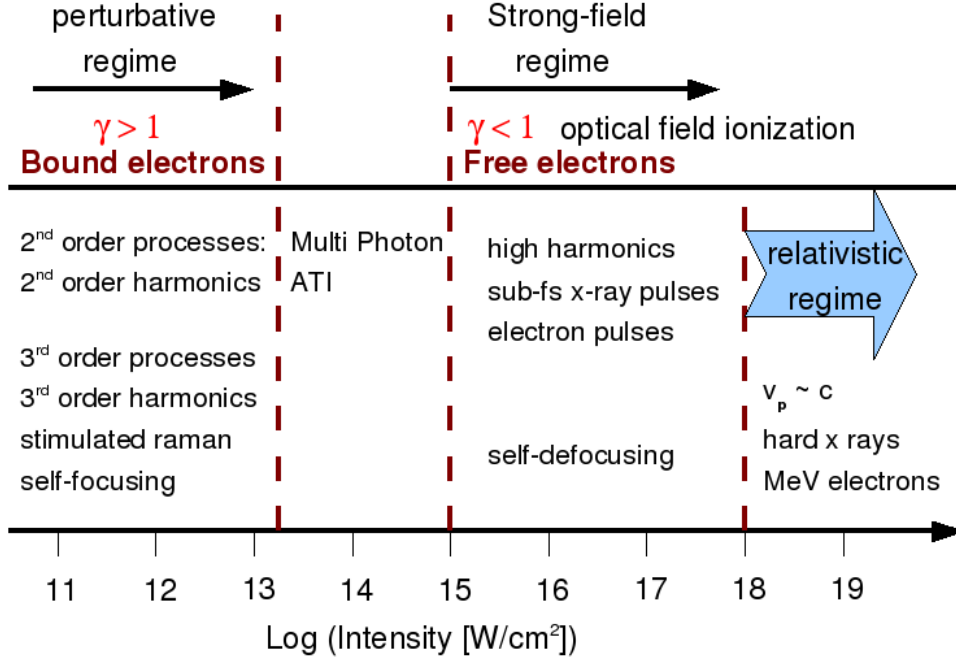


**Figure 2.1:** Overview of field strengths and the processes which occur in monochromatic light fields [3]

The ponderomotive potential  $U_P$  is determined by the kinetic energy averaged over an oscillation period

$$U_P = \langle E_{\text{kin}} \rangle = \frac{1}{4} \frac{e_0^2}{m_e} \frac{E_0^2}{\omega^2}. \quad (2.4)$$

Using this quantity we introduce the *Keldysh* (or adiabatic) parameter [18, 19]:

$$\gamma = \frac{\omega}{E_0} \sqrt{2I_p} \cdot \frac{\sqrt{m_e}}{e_0} = \sqrt{\frac{I_p}{2U_P}}. \quad (2.5)$$

In experiments the *intensity* of a pulse is usually the characterizing quantity. It is derived from the Poynting vector and is determined by

$$I = \frac{1}{8\pi} c E^2, \quad (2.6)$$

where  $c$  is the velocity of light in vacuum. Fig. 2.1 shows the appearing effects for different intensity regimes and the related Keldysh parameter. For  $\gamma \gg 1$  the field can be treated as a small perturbation of the atomic system, whereas for  $\gamma \ll 1$  the atom is a small perturbation of the strong laser field.

### 2.1.2 Photoionization and resonant excitations

First we mention effects in light fields for  $\gamma \gg 1$ . Experimentally, this region is covered by low-intensity pulses. The well-known effects which helped understand the electronic structure of atoms are the direct photoionization and the resonant absorption of photons (cf. Fig. 2.2). For intensities clearly in the perturbative regime the electron can absorb photons only

- if  $\Delta E = \hbar\omega$ , where  $\Delta E$  is the energy difference between two discrete levels (*Bohr* condition)

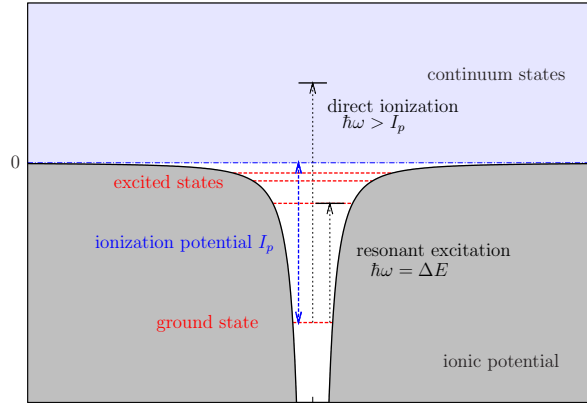


**Figure 2.2:** Schematic view of the model atom in a weak laser field. The energy levels (red dashed lines) in the Coulomb potential remain nearly unchanged. The discrete bound states ( $E_n < 0$ ) are coupled to a continuum with  $E > 0$ . Two processes can appear, depending on the photon energy  $\hbar\omega$  of the light field: The direct ionization into a free electron state ( $\hbar\omega > I_p$ ) and the resonant excitation ( $\hbar\omega = \Delta E$ ) into a higher bound state (linear effects).

- or if the photon energy is high enough ( $\hbar\omega > I_p$ ) and the electron is excited to the continuum (ionized).

These effects are so called *linear* effects.

### 2.1.3 Multi-photon ionization

The ionization of a quantum system is *non-linear* if the energy of one single irradiated photon is not sufficient to ionize the atom directly ( $\omega < I_p$ ) and at least two photons are needed. Clearly, this statement violates the well-known description of the atomic photo effect by Einstein which postulates the absorption of single quanta. But according to Heisenberg's principle the energy-time uncertainty of any process is given by  $\Delta E \cdot \Delta t > \hbar$ . Hence the transition from an initial state  $|0\rangle$  to a final state  $|v\rangle$  occurs within the energy width  $\Delta E$ . The electron stays in the state  $|v\rangle$  of the energy  $E_v = E_0 + \hbar\omega$  for a time  $\Delta t$ . Within this very small time it is able to absorb a second photon if the intensity of the external field is increased to about  $10^{14}$  W/cm<sup>2</sup> and higher. Such an energy level  $|v\rangle$  is called *virtual* state as it exists only for a very small time.

The electron can now climb a ladder of these intermediate virtual states  $|v_i\rangle$  until it reaches a final state  $|f\rangle$  with an energy  $E_f = n_{\text{thres}} \cdot \hbar\omega$  larger than the binding energy  $I_p$  [cf. Fig. 2.3 (a)]. This process is known as *multi-photon ionization* (MPI). The natural number  $n_{\text{thres}}$  is the minimal number of energy quanta (*threshold*) needed to raise the electron into the continuum.

If the final state  $|f\rangle$  is not a free state but a discrete atomic energy level which fulfills the resonance condition

$$n_{\text{thres}} \cdot \hbar\omega = E_f - E_0 \quad (2.7)$$

the analogous process of multi-photon *excitation* is possible. Eq. (2.7) can be regarded as an *extended* Bohr condition.

The MPI is a rather complex process and was theoretically first described by Keldysh [18] for short-range potentials. A discussion of his theory is given in Chapter 2.3.2. According to [21, 18] the rate of the MPI is determined by

$$w = \sigma^{(n_{\text{thres}})}(\omega, \rho)(I/\omega)^{n_{\text{thres}}} . \quad (2.8)$$

## 2 Atoms in laser fields

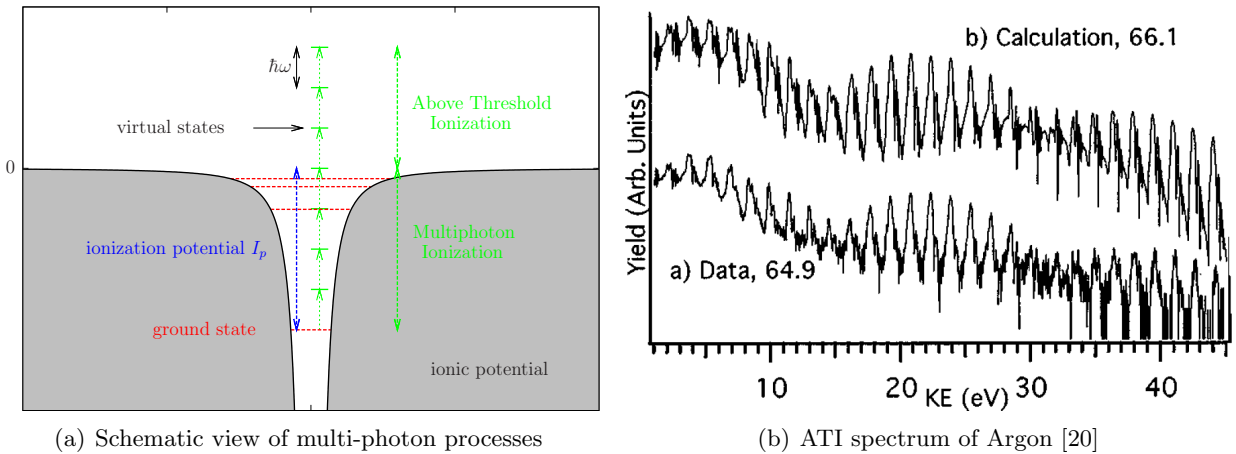


**Figure 2.3:** For pulses with sufficiently high intensity and  $\hbar\omega < I_p$  multi-photon processes occur. This non-linear effect allows an electron to absorb  $n_{\text{thres}}$  photons of the energy  $\hbar\omega$ . If the intensity is high enough, additional photons are absorbed which increase the kinetic energy of the free electron. Fig. (b) shows such an above threshold ionization spectrum measured on an Argon gas [lower curve in (b)] in comparison with a numerical solution of the one-particle time-dependent Schrödinger equation [upper curve in (b)]. The numbers give the intensity of the laser pulse in  $\text{TW}/\text{cm}^2$ .

$I$  is the intensity of the laser excitation and  $\sigma(\omega, \rho)$  denotes the multi-photon cross section.  $\rho$  is a parameter which describes the ellipticity of the radiation [21]. Notable is the power-law behavior on  $I$  and therefore on the electrical field strength  $E$ .

### 2.1.4 Above threshold ionization

An effect related to MPI is the above threshold ionization (ATI). Fig. 2.3 (b) shows a measurement and a calculation of a typical ATI spectrum of Argon atoms. For already ionized electrons, for instance by a MPI process, exists the probability to absorb  $k$  additional photons in high-intensity fields. Hence, the final energy of the electron is given by

$$E_f = (n_{\text{thres}} + k)\hbar\omega \quad k = 1, 2, 3, \dots \quad (2.9)$$

These additional photons increase the kinetic energy of the ionized electron. It is accelerated to a significant cut-off energy  $E_{\text{max}} = 8 \cdot U_p$ . For electrons below this energy the well-known *ATI-plateau* is formed. Although the ATI effect itself can be explained in terms of a perturbative theory, many effects need theories beyond this approach. The most prominent example is the *near threshold effect*: Some of the lower photon peaks ( $n_{\text{thres}}, n_{\text{thres}+1}, \dots$ ) disappear with increasing intensity. In contrast perturbation theory predicts a decrease in the intensity for an increasing number of absorption processes. The review books [19, 21] of Delone and Krainov and the review article of Eberly and Javanainen [22] give an comprehensive outline of this topic.

### 2.1.5 Strong field effects

We now switch to high-intensity laser pulses with  $\gamma \ll 1$ , hence the regime of electric field strengths where the electronic structure of the atom is strongly deformed. The boundary approximately corresponds to an intensity of  $I = 1 \text{ a.u.} = 3.4 \cdot 10^{16} \text{ W}/\text{cm}^2$ . The occurring effects are sketched in Fig. 2.4. The external potential becomes comparable to the atomic electric field strength or even larger. Modern laser systems easily reach intensities far beyond this threshold. Dominant effects are now tunneling processes and over barrier ionization (OBI). Again the first

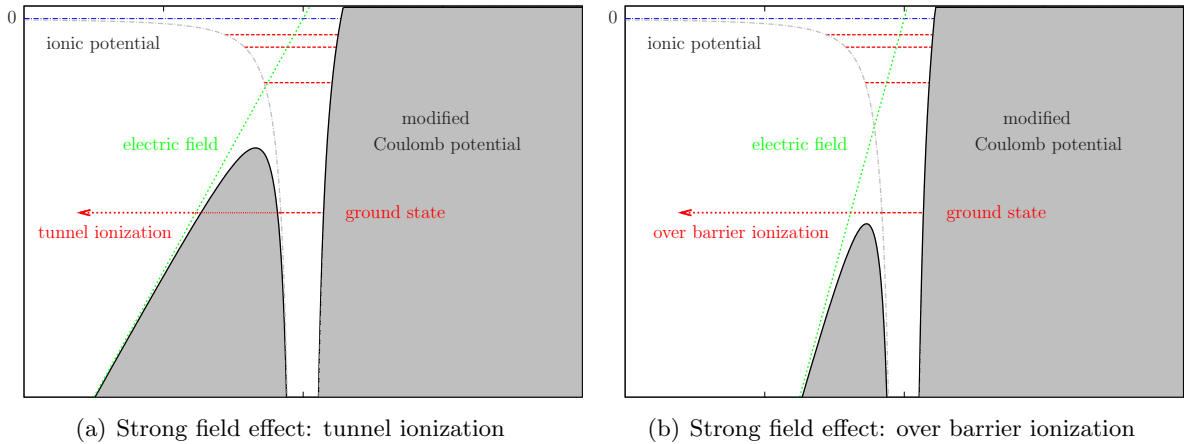


**Figure 2.4:** Optical field ionization: Modification of the ionic Coulomb potential due to the strong external field ( $\gamma \ll 1$ ). The atomic potential is strongly deformed and the ground state electron can leave its bound state by tunnel ionization (a) and/or over barrier ionization (b).

theory was given by Keldysh. The rates of the strong field ionization are [21, 18]

$$w \sim \exp\left(-\frac{2}{3} \frac{(2I_p)^{3/2}}{E}\right). \quad (2.10)$$

A comparison with Eq. (2.8) shows the significant difference to the MPI mechanism. The exponential function indicates a tunneling process. For slowly varying electric fields ( $\omega$  small), Eq. (2.10) describes the usual tunnel effect of an electron in a time-independent electric field. Thus the underlying physical mechanism is totally different from the MPI.

If the field strength gets even higher, a stabilization of the ionization rate is observed. The electron is then bound in quasi-states (very high-energy Rydberg states modified by the external potential). This effect is not in the focus of this introduction.

### 2.1.6 Higher harmonics generation

A direct consequence of multi-photon processes and strong field ionization (MPI, tunneling or OBI) is the generation of higher harmonics radiation. If the freed electron is driven back to its parent ion by the laser field it can recombine and during this scattering process it radiates a photon. Since the accelerated electron (by e.g. MP processes) lies high in the continuum this emitted photon exhibits very large energies. The resulting electro-magnetic radiation shows higher harmonics of the irradiated laser frequency and is used experimentally to create high-energy extreme ultraviolet (XUV) pulses. Fig. 2.5 visualizes the mechanism. A lot of theoretical and experimental work has been done on this topic [3].

## 2.2 Theoretical framework

The adequate theoretical tool for the investigation of ionization processes on a microscopic scale in the non-relativistic regime is the time-dependent Schrödinger equation (TDSE). The electro-magnetic field is treated classically within this work. No additional field quantization (QED) is applied. Thus effects like the spontaneous emission or absorption of photons and the corresponding life times and the decay of states cannot be described. However the classical treatment

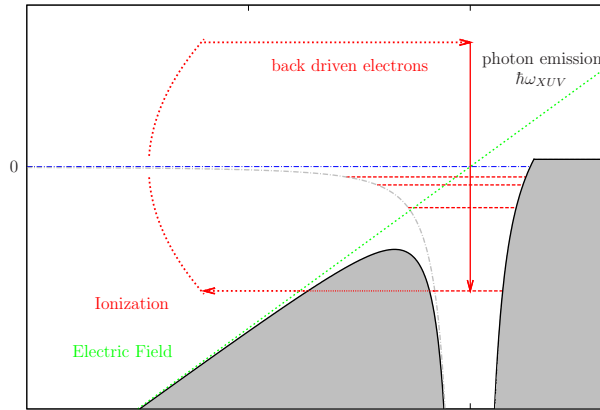


**Figure 2.5:** The mechanism for generation of higher harmonic radiation (HHG). The ionized electrons (MPI or optical field ionization) with large kinetic energies are driven back to the ion and undergo a complicated rescattering process. They emit photons with frequencies ( $\hbar\omega_{XUV}$ ) multiple times higher than the irradiated laser field. This process is widely used in experiments as a source for high-energy radiation.

includes the reaction of a system exposed to light fields very precisely since stimulated emission/absorption of photons exceeds the spontaneous effects by orders of magnitudes.

The vector potential  $\mathbf{A}(\mathbf{r}, t)$  and the scalar potential  $\phi(\mathbf{r}, t)$  characterize the electric field  $\mathbf{E}(\mathbf{r}, t)$  and the magnetic field  $\mathbf{B}(\mathbf{r}, t)$  by [23]:

$$\mathbf{E}(\mathbf{r}, t) = -\nabla\phi(\mathbf{r}, t) - \frac{1}{c} \frac{\partial \mathbf{A}(\mathbf{r}, t)}{\partial t} \quad \text{and} \quad \mathbf{B}(\mathbf{r}, t) = \nabla \times \mathbf{A}(\mathbf{r}, t) \quad (2.11)$$

which are determined by the solution of Maxwell's equations.

### 2.2.1 Atom-light-field interaction

The TDSE for one particle in an external potential  $V(\mathbf{r})$  interacting with a vector potential  $\mathbf{A}(\mathbf{r}, t)$  and a scalar potential  $\phi(\mathbf{r}, t)$  reads in atomic units ( $\hbar = m = e = 1$ , see Appendix A)

$$\frac{1}{2} \left( \hat{\mathbf{p}} + \frac{1}{c} \mathbf{A}(\mathbf{r}, t) \right)^2 \Psi(\mathbf{r}, t) - \phi(\mathbf{r}, t) \Psi(\mathbf{r}, t) + V(\mathbf{r}) \Psi(\mathbf{r}, t) = i \frac{\partial}{\partial t} \Psi(\mathbf{r}, t), \quad (2.12)$$

with the operator of momentum  $\hat{\mathbf{p}} = -i \nabla$ .  $V(\mathbf{r})$  denotes the one-particle potential, i.e., the ionic Coulomb potential.

As it is known from electro-dynamics, the observable fields  $\mathbf{E}(\mathbf{r}, t)$  and  $\mathbf{B}(\mathbf{r}, t)$  are not changed under a gauge transformation to new potentials  $\mathbf{A}'(\mathbf{r}, t)$  and  $\phi'(\mathbf{r}, t)$ :

$$\mathbf{A}'(\mathbf{r}, t) = \mathbf{A}(\mathbf{r}, t) + \nabla \Lambda(\mathbf{r}, t) \quad \text{and} \quad \phi'(\mathbf{r}, t) = \phi(\mathbf{r}, t) - \frac{1}{c} \frac{\partial \Lambda(\mathbf{r}, t)}{\partial t}, \quad (2.13)$$

where  $\Lambda(\mathbf{r}, t)$  is a scalar function. There exist an arbitrary number of different possible gauges. Concerning the matter-field interaction two gauges are mostly used in the literature: The *radiation* (also Coulomb or transversal) gauge and the *field* (also length or longitudinal) gauge. Since Eq. (2.12) contains the potentials  $\mathbf{A}$  and  $\phi$  the resulting phase of the wave function  $\Psi(\mathbf{r}, t)$  is changed by  $\exp(i e \Lambda / m c)$  under such a transformation. The observables of the quantum system are not changed (gauge-invariant).

For a source-free field ( $\rho(\mathbf{r}, t) = 0$ ) the scalar potential vanishes. Thus, only the vector potential  $\mathbf{A}$  is coupled to the system in Eq. (2.12). By expanding the brackets one obtains for the Hamiltonian (note:  $[\hat{\mathbf{p}}, \mathbf{A}(\mathbf{r}, t)] \neq 0$ ):

$$\hat{H} = \frac{1}{2} \left( \hat{\mathbf{p}} + \frac{1}{c} \mathbf{A}(\mathbf{r}, t) \right)^2 + V(\mathbf{r}) \quad (2.14)$$

$$= \underbrace{\frac{\hat{\mathbf{p}}^2}{2} + V(\mathbf{r})}_{\hat{H}_{\text{atom}}} + \underbrace{\frac{1}{2c} \mathbf{A}(\mathbf{r}, t) \cdot \hat{\mathbf{p}} + \frac{1}{2c} \hat{\mathbf{p}} \cdot \mathbf{A}(\mathbf{r}, t) + \frac{1}{2c^2} \mathbf{A}(\mathbf{r}, t)^2}_{\hat{H}_{\text{int}}} . \quad (2.15)$$

$\hat{H}_{\text{atom}}$  describes the atomic degrees of freedom, i.e., the energy levels of the ionic potential and is time-independent. The whole interaction with the electro-magnetic field is included in  $\hat{H}_{\text{int}}(t)$ . Up to this point everything is exact except for the classical treatment of the fields.

### 2.2.2 The dipole approximation

The exact Hamiltonian Eq. (2.15) explicitly contains the scalar products  $\hat{\mathbf{p}} \cdot \mathbf{A}$  and  $\mathbf{A} \cdot \hat{\mathbf{p}}$ . Things become much easier if the *dipole approximation* is introduced:

Usually the vector potential  $\mathbf{A}(\mathbf{r}, t)$  varies in space as

$$\mathbf{A}(\mathbf{r}, t) = \mathbf{A}_0 \cos(\mathbf{k} \cdot \mathbf{r} - \omega t) , \quad (2.16)$$

where  $\mathbf{k}$  is the wave vector. If the interaction region is small and the vector potential is not changing strongly within this area ( $\mathbf{k} \cdot \mathbf{r} \ll 1$ ), its spatial dependence can be neglected.

A Taylor expansion (up to first order) with respect to  $\mathbf{k} \cdot \mathbf{r}$  gives

$$\mathbf{A}(\mathbf{r}, t) = \underbrace{\mathbf{A}_0 \cos(\mathbf{k}_0 \mathbf{r}_0 - \omega t)}_{\mathbf{A}^{\text{dipole}}(\mathbf{r}_0, t)} - \underbrace{\mathbf{A}_0 \sin(\mathbf{k}_0 \mathbf{r}_0 - \omega t)(\mathbf{k} \mathbf{r} - \mathbf{k}_0 \mathbf{r}_0)}_{\mathbf{A}^{\text{quadrupole}}(\mathbf{r}, t)} + \dots \quad (2.17)$$

Therefore  $\mathbf{A}^{\text{dipole}}(\mathbf{r}_0, t)$  is independent of  $\mathbf{r}$  and the electric field shows according to

$$\mathbf{E}^{\text{dipole}}(\mathbf{r}, t) = -\frac{1}{c} \frac{\partial}{\partial t} \mathbf{A}^{\text{dipole}}(t) \equiv \mathbf{E}(t) \quad (2.18)$$

also only a time-dependent behavior. The main result is that  $\hat{\mathbf{p}}$  and  $\mathbf{A}^{\text{Dipole}}(t)$  commute:  $[\hat{\mathbf{p}}, \mathbf{A}(t)] = 0$ . Hence within the dipole approximation the interaction Hamiltonian, Eq. (2.15), is given by (radiation gauge)

$$\hat{H}_{\text{int}}^{\text{radiation}} = \frac{1}{c} \mathbf{A}(\mathbf{r}, t) \cdot \hat{\mathbf{p}} + \frac{1}{2c^2} \mathbf{A}(\mathbf{r}, t)^2 . \quad (2.19)$$

This representation of the interaction contains the vector potential and not the field itself. It is often useful for theoretical approaches like the strong field approximation (SFA) discussed later in this chapter. For numerical and practical reasons it is often better to use another gauge. The quantum mechanical observables are invariant under the phase transformation

$$\Psi'(\mathbf{r}, t) = \exp \left( -\frac{i}{c} \mathbf{A}(\mathbf{r}, t) \cdot \mathbf{r} \right) \Psi(\mathbf{r}, t) . \quad (2.20)$$

This is equivalent to a gauge transformation of the interaction Hamiltonian, Eq. (2.19). Using the TDSE (2.12) and inserting the new wave function  $\Psi'(\mathbf{r}, t)$  one resolves

$$i \frac{\partial}{\partial t} \Psi(\mathbf{r}, t) = \left( \frac{1}{2} \hat{\mathbf{p}}^2 + \mathbf{r} \cdot \mathbf{E}(t) + V(\mathbf{r}) \right) \Psi(\mathbf{r}, t) . \quad (2.21)$$

## 2 Atoms in laser fields

Thus the new interaction part of Eq. (2.15) is given by

$$\hat{H}_{\text{int}}^{\text{field}}(t) = \mathbf{r} \cdot \mathbf{E}(t) \quad (2.22)$$

which is the representation in *field* gauge. Eq. (2.22) is only correct within the dipole approximation. In the following the validity of this approximation shall be discussed.

The dispersion relation of a free electro-magnetic wave is given by

$$k = |\mathbf{k}| = \frac{\omega}{c}. \quad (2.23)$$

Therefore the product  $\mathbf{k} \cdot \mathbf{r}$  for the Taylor expansion Eq. (2.17) is of the order  $1/c \approx 1/137$  where a typical radius of  $r \approx 1\text{\AA}$  and a maximum energy of the exciting quantum of 1.0 a.u. is assumed. These atomic parameters give a good upper boundary. For wavelengths of visible light,  $1/k \approx 1000 - 10000 \text{\AA}$ , the product becomes even smaller:  $\mathbf{k} \cdot \mathbf{r} \approx 10^{-3} \dots 10^{-4}$ . Therefore the dipole approximation is applicable for standard laser sources and atoms. If dipole forbidden transitions become important (allowed for instance by quadrupole transitions or magnetic field induced transitions) it fails earlier. In strong fields this scenario may be realistic. For XUV pulses and/or larger geometries the product  $\mathbf{k} \cdot \mathbf{r}$  has to be evaluated and compared to  $1/c$ .

## 2.3 Overview of theoretical approaches

Since an exact analytical solution of the TDSE is not possible, many theoretical tools for its approximate solution have been developed in the last decades. While the perturbation theories for weak field effects were discovered very early in the history of quantum mechanics the accurate description of strong field effects especially for Coulomb-like long-range potentials is still actively studied [4, 24].

### 2.3.1 Perturbative methods

The best-known method to calculate transition probabilities induced by an external time-dependent field is the time-dependent perturbation theory. Its derivation is outlined in most textbooks on quantum mechanics, e.g. [25]. In [26] the focus lies especially on atomic systems.

The basic idea is to split the total Hamilton operator:

$$\hat{H} = \hat{H}_{\text{atom}} + \hat{H}_{\text{int}}(t). \quad (2.24)$$

$\hat{H}_{\text{atom}}$  is usually the unperturbed atomic system with known eigenenergies  $E_n$  and eigenfunctions  $|\phi_n\rangle$

$$\hat{H}_{\text{atom}}|\phi_n\rangle = E_n|\phi_n\rangle. \quad (2.25)$$

$\hat{H}_{\text{int}}(t)$  describes, as in the previous case, the interaction with the electro-magnetic radiation but is assumed to be small compared to  $\hat{H}_{\text{atom}}$ .

Let the system at the time  $t_0$  be in the eigenstate  $|\phi_n\rangle$ . Now the perturbation, i. e., the laser field is switched on. It induces transitions between the energy levels  $|\phi_n\rangle \leftrightarrow |\phi_m\rangle$ . By expanding the perturbed solution in terms of the complete orthonormal system of  $\hat{H}_{\text{atom}}$  one finally obtains for the probability amplitude to find the system in the state  $|\phi_m\rangle$

$$c_m(t) = \delta_{mn} - \frac{i}{\hbar} \int_{t_0}^t d\tau \langle \phi_m | \hat{H}_{\text{int}}(\tau) | \phi_n \rangle \exp[i(E_m - E_n)\tau]. \quad (2.26)$$

The Kronecker symbol  $\delta_{mn}$  indicates the initially populated state  $|\phi_n\rangle$ . Hence the probability to find the system in a different state  $|\phi_m\rangle$  is given by

$$p_m(t) = |c_m(t)|^2 = \frac{1}{\hbar^2} \left| \int_{t_0}^t d\tau \langle \phi_m | \hat{H}_{\text{int}}(\tau) | \phi_n \rangle \exp[i(E_m - E_n)\tau] \right|^2 \quad \text{for } m \neq n. \quad (2.27)$$

For perturbations with monochromatic character, i. e.,  $\hat{H}_{\text{int}}(t) = \hat{V}_0 \sin(\omega t)$  with the frequency  $\omega$  and a coupling to continuous states  $|\phi_m\rangle$ , the integral in Eq. (2.27) can be evaluated analytically and one determines in the limit  $t \rightarrow \infty$  the famous golden rule of Fermi:

$$P_{n \rightarrow m}^- = \frac{2\pi}{\hbar} \left| \langle \phi_m | \hat{V}_0 | \phi_n \rangle \right|^2 \delta(E_m - E_n + \hbar\omega) \quad \text{for } m < n, \quad (2.28)$$

$$P_{n \rightarrow m}^+ = \frac{2\pi}{\hbar} \left| \langle \phi_n | \hat{V}_0 | \phi_m \rangle \right|^2 \delta(E_m - E_n - \hbar\omega) \quad \text{for } m > n. \quad (2.29)$$

These equations describe the induced emission ( $P_{n \rightarrow m}^-$ ) and the induced absorption ( $P_{n \rightarrow m}^+$ ) of a photon with the energy  $\hbar\omega$ . The  $\delta$ -function assures energy conservation. Eqs. (2.28) and (2.29) can only be applied to transitions into continuous states.

### 2.3.2 Strong field approximation (SFA)

Keldysh was the first who described strong field processes on a non-perturbative level [18]. His approach gives access to ionization rates in a closed analytical form and demonstrates the treatment of high-intensity fields.

The transition probability amplitude of a system initially prepared in the state  $|\phi_i\rangle$  to a final state  $|\phi_f\rangle$  reads according to [24]

$$p_{i \rightarrow f} = -i \int_{-\infty}^{\infty} dt \langle \phi_f(t) | \hat{H}_{\text{int}}(t) | \phi_i(t) \rangle. \quad (2.30)$$

One recognizes the similarity to the time-dependent perturbation theory, Eq. (2.26). Again  $\hat{H}_{\text{int}}$  is determined by Eqs. (2.19) or (2.22). If the state  $|\phi_f\rangle$  is a full solution of the TDSE this expression is exact. But of course this solution is unknown, thus one has to make a reliable approximation for the final state. Keldysh used the wave function of a free electron in a changing electro-magnetic field, the so-called *Volkov* states:

$$\phi_f(\mathbf{k}, \mathbf{r}, t) = \frac{1}{(2\pi)^{3/2}} \exp(i\mathbf{k} \cdot \mathbf{r}) \exp\left(-i\frac{k^2}{2}t\right) \exp[i\delta(\mathbf{k}, \mathbf{r}, t)], \quad (2.31)$$

where  $\delta(\mathbf{k}, \mathbf{r}, t)$  is the Volkov phase

$$\delta(\mathbf{k}, \mathbf{r}, t) = \mathbf{A}^*(t) \cdot \mathbf{r} - \mathbf{k} \int_{\infty}^t dt' \mathbf{A}^*(t') - \frac{1}{2} \int_{\infty}^t dt' [\mathbf{A}^*(t')]^2. \quad (2.32)$$

$\mathbf{A}^*$  denotes the vector potential  $\mathbf{A}$  multiplied by  $c$ . Eq. (2.31) is the solution of the TDSE (2.12) without the atomic potential  $V(\mathbf{r})$ .

For the case of a monochromatic linearly polarized laser field with frequency  $\omega$  the Volkov state can be written as [cf. Eq. (D.3)]

$$\phi_f(\mathbf{k}, \mathbf{r}, t) = \exp(i\mathbf{k} \cdot \mathbf{r} - iE_V t + \delta_{\text{osz}}). \quad (2.33)$$

$\delta_{\text{osz}}$  indicates a time-dependent oscillating phase. The energy  $E_V$  is constantly shifted by the term  $U_p$ :

$$E_V = \frac{k^2}{2} + \frac{1}{4} \frac{E_0^2}{\omega^2} = \frac{k^2}{2} + U_p. \quad (2.34)$$

## 2 Atoms in laser fields

This additional energy is nothing else than the ponderomotive energy derived classically in Chapter 2.1.1, Eq. (2.4).

The initial state in Eq. (2.30) is given in terms of a bound electron state, i.e., an eigenfunction of the unperturbed Hamiltonian. Better accuracy can be achieved if the time-dependent Stark and Zeeman effects, which affect the electronic structure of atoms in laser fields, are included. Using circularly polarized light fields and the free Volkov states Keldysh was able to resolve the rates for MPI and tunnel ionization, Eqs. (2.8) and (2.10). The generalization to linearly polarized fields was given by Reiss [27]. Faisal derived similar expressions earlier with the use of another gauge [28]. Therefore the SFA is also known as Keldysh-Faisal-Reiss (KFR) theory.

The Volkov states cannot accurately describe the transition rates for long-range potentials like the Coulomb potential. Since the final state has a plane-wave character no correction due to the additional ionic potential is included. Such effects are called *Coulomb* effects. Recent works use distorted wave approximations where the final Volkov states are multiplied with a Coulomb-induced distorting function. The most commonly used method is based on the first Born approximation [24] and is referred to as *Coulomb-Volkov-Approximation* (CVA). Many comparisons between those approaches and benchmarking numerical full TDSE solutions are available in the literature, e.g. in [4, 29, 30] — an example is presented in Chapter 5.2.2.

### 2.3.3 Floquet states

Quasi-energy-states (QES) offer another important tool for the evaluation of ionization rates in intense laser fields. This shall be mentioned only briefly, although it is a widely used and powerful approach. Delone and Krainov give a broad outline of this method in [19]. A short introduction can be found in [26].

For a monochromatic external field with frequency  $\omega$ , the Hamilton operator possesses a periodic time dependence with the period  $T = 2\pi/\omega$ . Thus a possible ansatz for the solution of the TDSE is

$$\Psi(t) = \exp(iEt) \Phi_E(t) \quad \text{with} \quad \Phi_E(t+T) = \Phi_E(t), \quad (2.35)$$

and therefore leads to a solution with the same period except for the phase. By inserting this ansatz into the TDSE one obtains the defining equation for  $\Phi_E$ :

$$\left( \hat{H} - i \frac{\partial}{\partial t} \right) \Phi_E(\mathbf{r}, t) = E \Phi_E(\mathbf{r}, t). \quad (2.36)$$

This is an eigenvalue problem for the operator  $\hat{H} - i\partial/\partial t$ . The eigenenergies are *quasi* energies and the corresponding eigenstates  $\Phi_E$  are *Floquet* states. For this problem time-*independent* perturbation theory is applicable. Applications and detailed calculations of ionization rates can be found in the monograph of Manakov [31].

## 3 Numerical method

This chapter deals with the numerical solution of the one-particle time-dependent Schrödinger equation (TDSE). As discussed before in Chapter 2.2 this gives the opportunity to study ionization and scattering processes on a microscopic scale within the one-particle picture without any further approximations.

The first part contains a detailed description of the numerical solution of the TDSE in terms of an implementation of the *Crank-Nicolson* procedure on spatial grids. Different types of boundary conditions are discussed. Afterwards we address the construction of initial conditions. Two techniques, namely the imaginary time stepping and the shooting method are mentioned. As the focus of this thesis lies on effects in laser fields the transformation of the TDSE to an adapted coordinate frame [*Kramers-Henneberger* (KH) frame] is introduced. The following paragraph deals with the computation of observables and energy spectra. One central problem is the modelling of a detector for scattered parts of the wave function (fast electrons). Finally this chapter closes with a description of the implementation scheme in the programming language C.

### 3.1 The numerical solution of the Schrödinger equation

In spatial coordinate representation, the Schrödinger equation for a single particle reads

$$i\hbar \frac{\partial}{\partial t} \Psi(\mathbf{r}, t) = \hat{H} \Psi(\mathbf{r}, t) . \quad (3.1)$$

$\hat{H}$  is the Hamilton operator which is defined as:

$$\hat{H} = -\frac{\hbar^2}{2m} \Delta + V(\mathbf{r}, t) , \quad (3.2)$$

and  $V(\mathbf{r}, t)$  denotes the potential energy which includes all time-dependent external excitations such as laser fields or static (time-independent) ionic potentials. Additional confinement potentials can also be treated with this term.

In the atomic system of units ( $\hbar = m = e = 1$ ) Eq. (3.1) transforms into

$$i \frac{\partial}{\partial t} \Psi(\mathbf{r}, t) = -\frac{1}{2} \Delta \Psi(\mathbf{r}, t) + V(\mathbf{r}, t) \Psi(\mathbf{r}, t) . \quad (3.3)$$

The numerical solution of the TDSE is a widely studied subject. There exist many different approaches. Each computational technique has its own range of applicability. One has to choose the best fitting procedure according to the system of investigation. This may enormously affect the resulting efficiency and accuracy. For an overview see e.g. [32].

The central systems investigated throughout this work are scattering situations in one and two dimensions. Spatial cartesian coordinates become apparent to be the optimal choice for the representation of the TDSE. The numerical schemes best adapting these types of systems are grid methods based on finite differences.

### 3 Numerical method

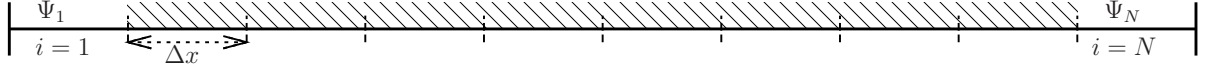


**Figure 3.1:** Schematic view of the one-dimensional grid. The TDSE is solved within the marked region.  $i = 1$  and  $i = N$  are given by the boundary conditions.

#### 3.1.1 1D-Crank-Nicolson method

The TDSE is a complex diffusion-like initial value problem supplemented by boundary conditions. In order to construct a stable differencing scheme it is necessary to use a fully implicit second order method since explicit schemes are not assuring the unitarity of the wave function [33].

The one-dimensional version of Eq. (3.3) reads

$$i \frac{\partial}{\partial t} \Psi(x, t) = -\frac{1}{2} \frac{d^2}{dx^2} \Psi(x, t) + V(x) \Psi(x, t). \quad (3.4)$$

Its formal solution is well-known:

$$\Psi(x, t) = e^{-i\hat{H}t} \Psi_0(x). \quad (3.5)$$

$\Psi_0(x)$  represents the initial wave function for  $t = 0$ .  $\hat{H}$  is assumed to be time-independent. This is true even for time-dependent external potentials because only the time evolution for very small times  $\Delta t$  is important while the external perturbation is supposed to be nearly constant. A differencing scheme in time which leads to the *Crank-Nicolson* procedure is based on Cayleys form of the operator  $e^{-i\hat{H}t}$  [33]:

$$e^{-i\hat{H}t} \approx \frac{1 - \frac{1}{2}i\hat{H}\Delta t}{1 + \frac{1}{2}i\hat{H}\Delta t}. \quad (3.6)$$

This expansion implies a *unitary* time evolution, hence the normalization of the wave function

$$\int_{-\infty}^{\infty} |\Psi(x, t)|^2 dx$$

is assured to be one for all times  $t$ . Using Eq. (3.6) one resolves for the time propagation of  $\Delta t$  of a state  $\Psi(x, t) \equiv \Psi_i^n$  to the state  $\Psi(x, t + \Delta t) \equiv \Psi_i^{n+1}$

$$\left(1 + \frac{1}{2}i\hat{H}\Delta t\right) \Psi_i^{n+1} = \left(1 - \frac{1}{2}i\hat{H}\Delta t\right) \Psi_i^n. \quad (3.7)$$

The index  $i$  indicates the spatial discretization with the step size  $\Delta x$  whereas the superscript  $n$  denotes discretization in time with time step  $\Delta t$ . Now, the Hamiltonian  $\hat{H}$  is replaced by a finite difference approximation. Throughout this work a second-order expression for the derivatives is used:

$$\partial_x^2 \Psi_i^n \equiv \frac{d^2}{dx^2} \Psi(x, t) \approx \frac{\Psi_{i+1}^n - 2\Psi_i^n + \Psi_{i-1}^n}{(\Delta x)^2}. \quad (3.8)$$

Combining Eqs. (3.7) and (3.8) with the notations

$$\alpha = \frac{1}{4} i \frac{\Delta t}{(\Delta x)^2} \quad (3.9)$$

### 3.1 The numerical solution of the Schrödinger equation

and

$$a_i = -\alpha = c_i, \quad b_i = 1 + 2\alpha + \frac{1}{2}i\Delta t V_i^{n+1}, \quad i = 2 \dots N-1 \quad (3.10)$$

yields for the left hand side of Eq. (3.7):

$$\left(1 + \frac{1}{2}i\Delta t \hat{H}_i\right) \Psi_i^{n+1} = a_i \Psi_{i-1}^{n+1} + b_i \Psi_i^{n+1} + c_i \Psi_{i+1}^{n+1}. \quad (3.11)$$

Analogously the right hand side of Eq. (3.7) transforms into

$$\left(1 - \frac{1}{2}i\hat{H}\Delta t\right) \Psi_i^n = \Psi_i \left(1 - 2\alpha - \frac{1}{2}i\Delta t V_i^n\right) + \alpha \Psi_{i-1}^n + \alpha \Psi_{i+1}^n \equiv r_i^n, \quad (3.12)$$

$$i = 2 \dots N-1.$$

Expressing the combination of Eq. (3.11) and Eq. (3.12) in matrix form one obtains a tridiagonal system of linear equations for the unknown variable  $\Psi_i^{n+1}$ :

$$\begin{pmatrix} b_1 & c_1 & 0 & 0 \\ a_2 & b_2 & c_2 & 0 \\ \cdot & \cdot & \cdot & \cdot \\ 0 & 0 & a_N & b_N \end{pmatrix} \cdot \begin{pmatrix} \Psi_1^{n+1} \\ \Psi_2^{n+1} \\ \cdot \\ \Psi_N^{n+1} \end{pmatrix} = \begin{pmatrix} r_1^n \\ r_2^n \\ \cdot \\ r_N^n \end{pmatrix}. \quad (3.13)$$

The elements  $b_1$ ,  $c_1$  and  $r_1^n$  are defined by the boundary conditions at the left edge of the grid, see Chapter 3.1.4. In analogy,  $b_N$ ,  $c_N$  and  $r_N^n$  are defined at the right edge. Eq. (3.13) can be solved very efficiently, for instance with algorithms found in [33], Chapter 2.6. Unfortunately, in the most common numerical libraries (e.g. GNU scientific library, NAG) no specialized routines are implemented.

#### 3.1.2 Solving the two-dimensional Schrödinger equation

In the following section a generalization of the one-dimensional Crank-Nicolson procedure to 2D grids is presented. It is based on the *operator splitting* technique.

Already expanded by the usage of Cayleys form, the TDSE in two spatial coordinates reads [cf. Eq. (3.7)]:

$$\left(1 + \frac{1}{2}i\Delta t \hat{H}\right) \Psi(x, y, t + \Delta t) = \left(1 - \frac{1}{2}i\Delta t \hat{H}\right) \Psi(x, y, t). \quad (3.14)$$

Similar to the 1D case, a finite differencing scheme for the 2D Hamilton operator

$$\hat{H} = -\frac{1}{2} \left( \frac{d^2}{dx^2} + \frac{d^2}{dy^2} \right) + V(x, y) \quad (3.15)$$

has to be derived. The wave function  $\Psi(x, y, t)$  and  $\hat{H}$  are replaced by their discretized versions  $\Psi_{i,j}^n$  and  $\hat{H}_{i,j}$ . The indices  $i, j$  denote the spatial grid coordinates  $x$  and  $y$  (Fig. 3.2). Again,  $n$  denotes the discretization in time.

Since the potential energy operator  $\hat{V}$  is diagonal in the spatial coordinate representation its replacement by a discrete function  $V_{i,j}$  is simple:

$$V(x, y) \Psi(x, y, t) \rightarrow V_{i,j} \Psi_{i,j}^n. \quad (3.16)$$

The differential operators are approximated in second order [cf. Eq. (3.8)] by

$$\frac{d^2}{dx^2} \Psi(x, y, t) \approx \frac{\Psi_{i+1,j}^n - 2\Psi_{i,j}^n + \Psi_{i-1,j}^n}{(\Delta x)^2} \equiv \partial_x^2 \Psi_{i,j}^n, \quad i, j = 2 \dots N-1 \quad (3.17)$$

### 3 Numerical method

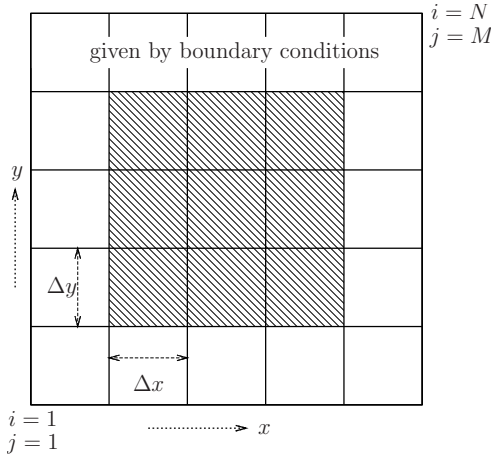


**Figure 3.2:** Schematic view of the two-dimensional grid. The white region is defined by the boundary conditions (values fixed). Within the central region the tridiagonal equation system is solved via the operator splitting method. Usually  $\Delta x = \Delta y$  is chosen.

$$\frac{d^2}{dy^2}\Psi(x, y, t) \approx \frac{\Psi_{i,j+1}^n - 2\Psi_{i,j}^n + \Psi_{i,j-1}^n}{(\Delta y)^2} \equiv \partial_x^2 \Psi_{i,j}^n, \quad i, j = 2 \dots N-1 \quad (3.18)$$

$\Delta x$  and  $\Delta y$  are the parameters of the spatial grid in the  $x$  and  $y$  direction. For simplicity  $\Delta x = \Delta y$  is chosen. Hence the discretized version of Eq. (3.14) becomes with

$$\hat{H} \rightarrow H_{i,j} = -\frac{1}{2} (\partial_x^2 + \partial_y^2) + V_{i,j} : \quad (3.19)$$

$$\left(1 + \frac{1}{2}i\Delta t \hat{H}_{i,j}\right) \Psi_{i,j}^{n+1} = \left(1 - \frac{1}{2}i\Delta t \hat{H}_{i,j}\right) \Psi_{i,j}^n. \quad (3.20)$$

Comparing Eq. (3.20) with its one-dimensional analogon, Eq. (3.7), one recognizes the additional index  $j$ . The straightforward solution leads to a system of equations which has additional diagonal elements. It is obviously not tridiagonal (*tridiagonal with fringes*). Since the solution of such systems requires a lot more computational effort as well as storage memory for the matrix elements an alternative procedure has been chosen: The *alternating direction implicit* (ADI) method.

The basic idea is to perform the finite differencing steps independently in the  $x$  and  $y$  direction. An additional step is done for the potential  $V$ . To ensure the same accuracy as in the one-dimensional case the size of the time step is decreased by a factor of three. The underlying mathematical treatment is given by the operator splitting technique [33].

Hence, the whole propagation scheme can be expressed as

$$\left(1 - \frac{1}{4}i\frac{\Delta t}{3}\partial_x^2\right) \Psi_{i,j}^{n+\frac{1}{3}} = \left(1 + \frac{1}{4}i\frac{\Delta t}{3}\partial_x^2\right) \Psi_{i,j}^n, \quad (3.21)$$

$$\left(1 - \frac{1}{4}i\frac{\Delta t}{3}\partial_y^2\right) \Psi_{i,j}^{n+\frac{2}{3}} = \left(1 + \frac{1}{4}i\frac{\Delta t}{3}\partial_y^2\right) \Psi_{i,j}^{n+\frac{1}{3}}, \quad (3.22)$$

$$\left(1 + \frac{1}{2}i\frac{\Delta t}{3}V_{i,j}\right) \Psi_{i,j}^{n+1} = \left(1 - \frac{1}{2}i\frac{\Delta t}{3}V_{i,j}\right) \Psi_{i,j}^{n+\frac{2}{3}}. \quad (3.23)$$

The first two equations belong to the spatial dimensions  $x$  and  $y$  whereas the third step involves the potential. The major advantage is that each individual sub step in  $x$  and  $y$  direction can be evaluated similar to the 1D case.

Thus, the first step gives for the left hand side of Eq. (3.21)

$$\left(1 - \frac{1}{12}i\frac{\Delta t}{(\Delta x)^2}\partial_x^2\right) \Psi_{i,j}^{n+\frac{1}{3}} = a_i\Psi_{i-1,j}^{n+\frac{1}{3}} + b_i\Psi_{i,j}^{n+\frac{1}{3}} + c_i\Psi_{i+1,j}^{n+\frac{1}{3}}. \quad (3.24)$$

### 3.1 The numerical solution of the Schrödinger equation

And for the right hand side analogously

$$\left(1 + \frac{1}{12} \frac{\Delta t}{(\Delta x)^2} i \partial_x^2\right) \Psi_{i,j}^n = \alpha \Psi_{i+1,j}^n + (1 - 2\alpha) \Psi_{i,j}^n + \alpha \Psi_{i-1,j}^n \equiv r_i^n \quad (3.25)$$

with the notations

$$\alpha = \frac{1}{12} i \frac{\Delta t}{(\Delta x)^2}, \quad a_i = -\alpha = -c_i, \quad b_i = (1 + 2\alpha). \quad (3.26)$$

Like in the 1D case this is a tridiagonal system of equations for the unknown variable  $\Psi_{i,j}^{n+\frac{1}{3}}$ :

$$a_i \cdot \Psi_{i-1,j}^{n+\frac{1}{3}} + b_i \cdot \Psi_{i,j}^{n+\frac{1}{3}} + c_i \cdot \Psi_{i+1,j}^{n+\frac{1}{3}} = r_i^n. \quad (3.27)$$

During this step, only the  $x$ -direction is propagated. The solution for the  $y$ -direction is calculated in the same manner and yields

$$a_j \cdot \Psi_{i,j-1}^{n+\frac{2}{3}} + b_j \cdot \Psi_{i,j}^{n+\frac{2}{3}} + c_j \cdot \Psi_{i,j+1}^{n+\frac{2}{3}} = r_j^{n+\frac{1}{3}} \quad (3.28)$$

with

$$r_j^{n+\frac{1}{3}} = \alpha \Psi_{i,j+1}^{n+\frac{1}{3}} + (1 - 2\alpha) \Psi_{i,j}^{n+\frac{1}{3}} + \alpha \Psi_{i,j-1}^{n+\frac{1}{3}}. \quad (3.29)$$

Finally, the last sub step for the potential, Eq. (3.23), gives

$$\Psi_{i,j}^{n+1} = \left(1 - i \frac{\Delta t}{6} V_{i,j}\right) \Psi_{i,j}^{n+\frac{2}{3}} \cdot \left(1 + i \frac{\Delta t}{6} V_{i,j}\right)^{-1} = \frac{(1 - \beta)}{(1 + \beta)} \Psi_{i,j}^{n+\frac{2}{3}} \quad (3.30)$$

with  $\beta = i \Delta t V_{i,j} / 6$ .

## Beyond two dimensions

Obviously, this procedure can easily be extended to 3D systems involving four sub steps. It is also usable to solve the multi-particle Schrödinger equation since it is basically a  $d \times N$ -dimensional problem.  $d$  denotes the spatial degrees of freedom and  $N$  the number of particles. The many-body Hamiltonian can be applied in terms of the operator splitting method for each sub dimension of the  $d \times N$  dimensional Hilbert space. Of course, with each additional dimension of the system the computation time and the memory usage increase enormously. Hence, for more than two particles this method is not applicable and one has to use theoretical many-body approaches like non-equilibrium Green's functions (NEGF) or time-dependent density functional theory (TDDFT).

### 3.1.3 Accuracy, stability and efficiency

The Crank-Nicolson procedure is an unconditionally stable differencing scheme. Thus it assures the normalization to unity of the wave function as mentioned above independently of the grid parameter  $\Delta x$  and the time step size  $\Delta t$ . The accuracy of the calculated solution of course does depend on those parameters. Numerical convergence tests on simple example systems are demonstrated in the next chapter. As the method is second order in time and space the accuracy increases by a factor of four if the step sizes are halved.

The numerical effort depends most on the algorithm which solves the tridiagonal system of linear equations. For each time step such a system with some ten thousand unknowns has to be computed. Efficient algorithms [33] based on the  $LU$  decomposition scale with  $\mathcal{O}(N)$  where  $N$

### 3 Numerical method

dim	$\Psi$	coefficient in equation system
1	$\Psi_{i=1}^n = 0$ $\Psi_{i=N}^n = 1$	$a_1 = a_N = 0$ $b_1 = b_N = 1 + i$ $c_1 = c_N = 0$ $r_1 = r_N = 0$
2	$\Psi_{i=1, j=1\dots M}^n$  $\Psi_{i=N, j=1\dots M}^n$ $\Psi_{i=1\dots N, j=1}$ $\Psi_{i=1\dots N, j=M}^n$	$a_{1, j=1\dots M} = a_{N, j=1\dots M} = 0$ $b_{1, j=1\dots M} = b_{N, j=1\dots M} = 1 + i$ $c_{1, j=1\dots M} = c_{N, j=1\dots M} = 0$ $r_{1, j=1\dots M} = r_{N, j=1\dots M} = 0$ analogous

**Table 3.1:** Dirichlet boundary conditions and the “edge” coefficients in the tridiagonal system of equations.

is the number of grid points. Thus the Crank-Nicolson method allows for a very fast algorithm for solving diffusion-like partial differential equations.

For 2D systems the total computation time and needed memory scales with  $\mathcal{O}(N \times M)$ . The maximum grids available for computations on common computer hardware are therefore limited to  $\approx 6000 \times 6000$  grid points. For long simulation runs of several ten thousand time steps even this size exceeds the capacity of usual personal computers. A recently developed high order method promises to enhance the accuracy enormously [34] allowing for larger time steps. However it was not implemented during this work.

#### 3.1.4 Boundary conditions

The initial value problem of the TDSE is supplemented by boundary conditions. Several possibilities are available. The best-known are Dirichlet and von Neumann boundary conditions which close the partial differential equation mathematically. Within this work only the first one is considered. The second one can be used to introduce flows at the grid edges by setting the derivative of the wave function to a finite value. The central calculations during this thesis concern problems where effects of the finite numerical grids have to be avoided. There exist some numerical useful approaches to minimize these boundary effects. A mathematical non-rigorous method in terms of imaginary absorbing potentials is discussed below.

#### Dirichlet boundary conditions

The conditions

$$\lim_{x \rightarrow \infty} \Psi(x, t) \rightarrow 0 \quad \text{and} \quad \lim_{x \rightarrow -\infty} \Psi(x, t) \rightarrow 0 \quad (3.31)$$

create a simulation box with reflecting grid boundaries. It assures the conservation of the normalization for all times if no dissipation is artificially included (e.g. absorbing potentials, see below). Eq. (3.31) can be fulfilled if the wave function vanishes for all times  $t$  at the grid edges. This can be assured by setting the first and the last elements in the tridiagonal system of equations according to Table 3.1. Obviously, this type of boundary conditions requires very large grids in order to allow for long simulation runs without influence of reflected parts of the wave function.

### Periodic boundary conditions

The solution of the TDSE with periodic boundary conditions  $\Psi_{i=0}^n = \Psi_{i=N}^n$  is also possible. But the occurring system of linear equations is not tridiagonal. Two additional elements  $d$  and  $e$  appear in the matrix of the coefficients. Such systems are called *cyclic* tridiagonal equation systems and have the form

$$\begin{pmatrix} b_1 & a_1 & 0 & d \\ a_2 & b_2 & a_2 & 0 \\ \cdot & \cdot & \cdot & \cdot \\ e & 0 & a_N & b_N \end{pmatrix} \cdot \begin{pmatrix} \Psi_1^{n+1} \\ \Psi_2^{n+1} \\ \cdot \\ \Psi_N^{n+1} \end{pmatrix} = \begin{pmatrix} r_1^n \\ r_2^n \\ \cdot \\ r_N^n \end{pmatrix}.$$

Reference [33] again gives an algorithm to solve this problem.

### Absorbing boundary conditions

Pure Dirichlet boundary conditions require very large grids to allow for long calculations without any disturbance from edge-reflecting parts of the wave function. To overcome this limitation absorbing boundary conditions are useful. There are basically two methods to be found in the literature.

The first one is especially important for one-dimensional calculations. It is based on a mathematical theory which allows to absorb the wave function at a specific grid point exactly [35]. Its computational implementation is difficult and for high-dimensional systems not applicable [36]. Thus it is not used within this work. The second method uses additional potentials in the system and enables a rather simple implementation.

If an imaginary part is added to the potential  $V(x)$  in the system the wave function  $\Psi(x, t)$  is damped during time propagation over this region. This can be explained in terms of the equation of continuity since this imaginary part of  $V$  acts like a dissipation term. One finds that this damping increases with higher energies of the propagated particle. Thus the faster, for instance, a wave packet like an electron travels the more it can be efficiently absorbed by the potential. This becomes important for situations where fast electrons are produced by scattering processes (Chapter 6). It has to be mentioned that those absorbing potentials have to be chosen carefully.

Every change in the potential, no matter if real or imaginary, leads also to a reflected part of the wave function. This can be minimized by using potentials which slowly vary in space. In this work only linear absorber potentials of the form

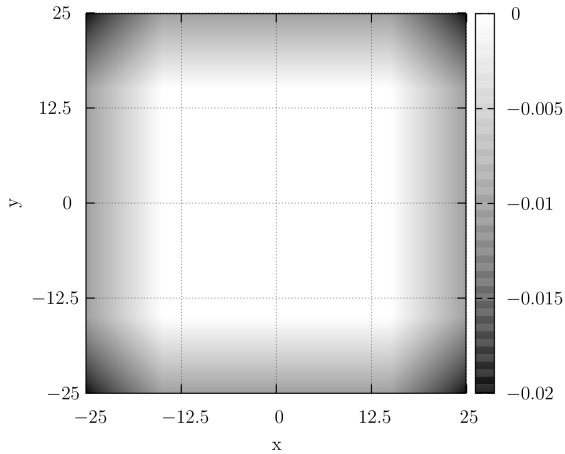
$$V(x) = i(a \cdot x - V_0) \tag{3.32}$$

are used. The parameters for good damping and negligible reflection  $V_0$  and  $a$  are chosen by experience. It appears that both have to be small (of the order  $0.1 \dots 0.01$ ). If grid sizes do *really* matter more efficient potentials are available in the literature [37, 38]. Fig. 3.3 (a) shows the implemented linear absorbing potential for a 2D grid. Fig. 3.3 (b) displays the absorption of a one-dimensional wave packet. Only a very small fraction ( $10^{-7}$ ) survives the damping and is reflected. These kinds of boundaries are of course not boundary conditions in a mathematical sense. The equation system (3.13) still has to be closed by usual Dirichlet conditions.

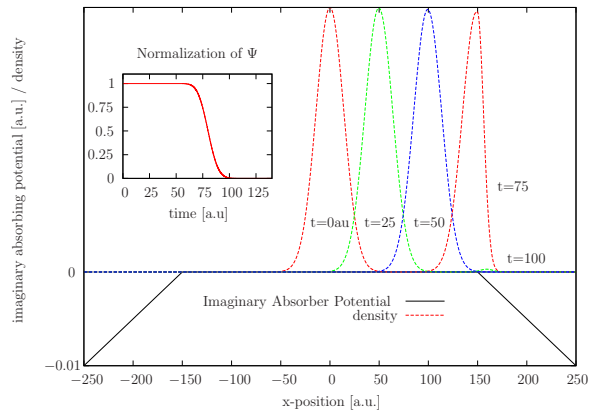
#### 3.1.5 Initial conditions

The time propagation of the TDSE needs an initial state  $\Psi_0(\mathbf{r}) = \Psi(\mathbf{r}, t = 0)$ . It describes the system before excitation (for example a laser field) is turned on. Two different situations are distinguished: Either the system is in an eigenstate of the ionic potential (bound electron) or the wave function represents a moving particle (e.g. Gaussian wave packet, see Chapter 4.2).

### 3 Numerical method



(a) 2D imaginary absorbing potential



(b) Absorption of a 1D wave packet,  $k = 2.0$  a.u. Only a fraction smaller than  $10^{-7}$  is reflected.

**Figure 3.3:** The implemented linear imaginary absorbing potential  $iV(x)$

In the following two different procedures to construct eigenstates are discussed: The solution of the time-independent Schrödinger equation by a symplectic scheme and the iteration of the TDSE in imaginary time direction. The first one is rather efficient for one- and special two-dimensional systems whereas the latter can be applied to arbitrary potentials and dimensions.

#### Solving the stationary Schrödinger equation

The eigenstates  $\psi_n$  of a 1D system with the potential  $V$  are given by the stationary Schrödinger equation

$$-\frac{1}{2} \frac{d^2}{dx^2} \psi_n(x) + V(x) \psi_n(x) = E_n \psi_n(x), \quad (3.33)$$

where  $E_n$  are the corresponding energy eigenvalues. One simple method to solve Eq. (3.33) is the *shooting* method [39]. This is a special case of the so called *Two Boundary Value Problem*. The idea is to probe for each energy  $E$  if it is an allowed eigenvalue  $E_n$ . This is only true for functions  $\psi_n(x)$  which satisfy all given boundary conditions. In most cases the wave function has to disappear at infinity.

The algorithm reads:

1. select an arbitrary energy  $E$
2. integrate Eq. (3.33) from the left with boundary conditions  $\psi(x \rightarrow -\infty) = 0$  and  $\frac{d}{dx} \psi(x)|_{x \rightarrow -\infty} \neq 0$
3. if boundary condition  $\psi(x \rightarrow \infty) = 0$  is satisfied, an eigenvalue  $E$  is found, if  $\psi(x \rightarrow \infty) \rightarrow \infty$  try another energy

The usage of the bisection method in the vicinity of the eigenvalues enhances this method. The shooting algorithm is only applicable for two-dimensional problems if the wave function  $\psi(x, y)$  can be separated into a product  $\psi(x, y) = \phi_1(x) \cdot \phi_2(y)$ . Then the shooting algorithm can be applied for each dimension individually.

### Imaginary time propagation (ITP)

If a time propagation code already exists, it can easily be used to calculate stationary states by replacing the time step  $\Delta t$  by an imaginary time  $i\Delta t$  [36]. An arbitrary state can be written as a superposition

$$|\Psi(t)\rangle = \sum_j c_j \exp(-iE_j t) |\psi_j\rangle, \quad (3.34)$$

with  $|\psi_j\rangle$  describing the stationary states. Now if the imaginary time is inserted, one obtains

$$|\Psi(t)\rangle = \sum_j \langle \psi_j | \Psi(t) \rangle \exp(E_j t) |\psi_j\rangle \quad (3.35)$$

and the corresponding states are exponentially decaying or increasing during the TDSE propagation depending on the sign of the energy eigenvalue. Only the ground state survives because it decays less or increases much faster than the other states. Of course this scheme does not conserve the normalization of the wave function thus the wave function has to be renormalized at each time step.

Excited states are also available. The orthogonalization of  $|\psi(t)\rangle$

$$|\psi_{n+1}^\perp\rangle = |\psi_{n+1}\rangle - \sum_{i=0}^n \langle \psi_{n+1} | \psi_i \rangle \cdot |\psi_i\rangle \quad (3.36)$$

which is, in coordinate representation,

$$\psi_{n+1}^\perp(\mathbf{r}) = \psi_{n+1}(\mathbf{r}) - \sum_{i=0}^n \left( \int_{-\infty}^{\infty} d^3\mathbf{r} \psi_{n+1}^*(\mathbf{r}) \psi_i(\mathbf{r}) \right) \cdot \psi_i(\mathbf{r}) \quad (3.37)$$

at each time step will force the wave function to converge to the next unknown eigenfunction.

During the imaginary iteration procedure several convergence indicators can be used. The total energy appears to be an improper criterion especially for higher excited states. Its convergence is very fast but not sensitive to density changes. Thus a density based quantity such as

$$\Delta\xi = \int_{-\infty}^{\infty} |\Psi(x, t) - \Psi(x, t + \Delta t)|^2 dx \quad (3.38)$$

seems to be of higher accuracy. Fig. 4.8 shows a comparison between the shooting method and the imaginary time propagation applied to the one-dimensional Coulomb potential. The big advantage of the ITP is that it works as well for higher dimensions (cf. Fig. 4.10).

## 3.2 Including the laser field

Chapter 2.2.1 describes the different possibilities to represent the laser field. Two gauges were introduced, the length gauge and the radiation gauge. The numerical treatment of the TDSE is performed within the field gauge in dipole approximation:

$$-\frac{1}{2} \frac{d^2}{dx^2} \Psi(x, t) + V_{\text{atom}}(x) \Psi(x, t) + f(t) E_0 x \sin(\omega t) \Psi(x, t) = i \frac{\partial}{\partial t} \Psi(x, t). \quad (3.39)$$

The laser parameters are the frequency  $\omega$ , the electrical field strength  $E_0$  and the shape (or envelope) function  $f(t)$ . The laser field is updated at each complete time step  $n \rightarrow n + 1$ .

### 3 Numerical method

#### 3.2.1 The Kramers-Henneberger frame of reference

Additionally a second powerful method is implemented which can decrease the needed spatial grid sizes. It is convenient to describe processes in laser fields not only in the usual laboratory frame of reference [Eq. (3.39)] but in a transformed frame, the so called Kramers-Henneberger (KH) coordinate frame [40, 41, 42]. In the following the TDSE in the new coordinate representation will be derived.

The Schrödinger equation in the laboratory frame reads in minimal coupling:

$$\frac{1}{2} \left( \frac{1}{i} \nabla - \frac{1}{c} \mathbf{A}(t) \right)^2 \Psi^{\text{lab}}(\mathbf{r}, t) + V(\mathbf{r}) \Psi^{\text{lab}}(\mathbf{r}, t) = i \frac{\partial}{\partial t} \Psi^{\text{lab}}(\mathbf{r}, t). \quad (3.40)$$

Now, we can introduce a new wave function  $\Psi^{\text{KH}}(\mathbf{r}, t) = \hat{U} \Psi^{\text{lab}}(\mathbf{r}, t)$  which is generated by the unitary transformation

$$\hat{U} = \exp \left( i \int_{-\infty}^t \hat{H}_{\text{int}}(\tau) d\tau \right) = \exp \left[ i \int_{-\infty}^t \left( \frac{i}{c} \mathbf{A}(\tau) \cdot \nabla + \frac{1}{2c^2} \mathbf{A}^2(\tau) \right) d\tau \right]. \quad (3.41)$$

$\hat{H}_{\text{int}}$  includes the field part of the Hamiltonian, hence

$$\hat{H}_{\text{int}} = \frac{1}{2} \left( \frac{1}{i} \nabla - \frac{1}{c} \mathbf{A} \right)^2 + \frac{1}{2} \Delta. \quad (3.42)$$

Since the dipole approximation is used ( $\mathbf{A}$  is independent of  $\mathbf{r}$ ) we can split the transformation operator

$$\hat{U} = \hat{U}^{\text{transl}} \cdot \hat{U}^{\text{phase}} = \exp \left( - \int_{-\infty}^t \frac{1}{c} \mathbf{A}(\tau) \cdot \nabla d\tau \right) \cdot \exp \left( \frac{i}{2c^2} \int_{-\infty}^t \mathbf{A}^2(\tau) d\tau \right). \quad (3.43)$$

The operator  $\hat{U}^{\text{transl}}$  is simply a translation operator. Its action on an arbitrary function  $f(\mathbf{r})$  is given by

$$\hat{U} f(\mathbf{r}) = f \left( \mathbf{r} - \int_{-\infty}^t \frac{1}{c} \mathbf{A}(\tau) d\tau \right). \quad (3.44)$$

In Appendix C, it is shown that  $\Psi^{\text{KH}}(\mathbf{r}, t)$  satisfies

$$-\frac{1}{2} \Delta \Psi^{\text{KH}}(\mathbf{r}, t) + V[\mathbf{r} + \boldsymbol{\alpha}(t)] \Psi^{\text{KH}}(\mathbf{r}, t) = i \frac{\partial}{\partial t} \Psi^{\text{KH}}(\mathbf{r}, t), \quad (3.45)$$

with  $\boldsymbol{\alpha} = - \int_{-\infty}^t \frac{1}{c} \mathbf{A}(\tau) d\tau$ . This is the Schrödinger equation in the Kramers-Henneberger frame. An interpretation is straightforward: For a vanishing scalar potential  $\phi$  one determines the electrical field from the relation  $\mathbf{E} = -\frac{1}{c} \frac{\partial}{\partial t} \mathbf{A}$  and hence

$$\frac{\partial^2}{\partial t^2} \boldsymbol{\alpha} = -\frac{1}{c} \frac{\partial}{\partial t} \mathbf{A}(t) = \mathbf{E}(t) \quad (3.46)$$

holds. Thus the atomic potential is shifted by the *classical* free electron displacement. This can be interpreted as the observer “sitting” on the electron which performs the classical quiver motion in the external electric field. The big advantage of the KH frame is the vanishing potential at large distances from the center of the grid. In field gauge the Schrödinger equation contains  $V(x) = Ex \sin(\omega t)$  which produces large potential energies far away from the atomic potential. Within the KH frame the electron behaves like a free particle in regions far away from the ion.

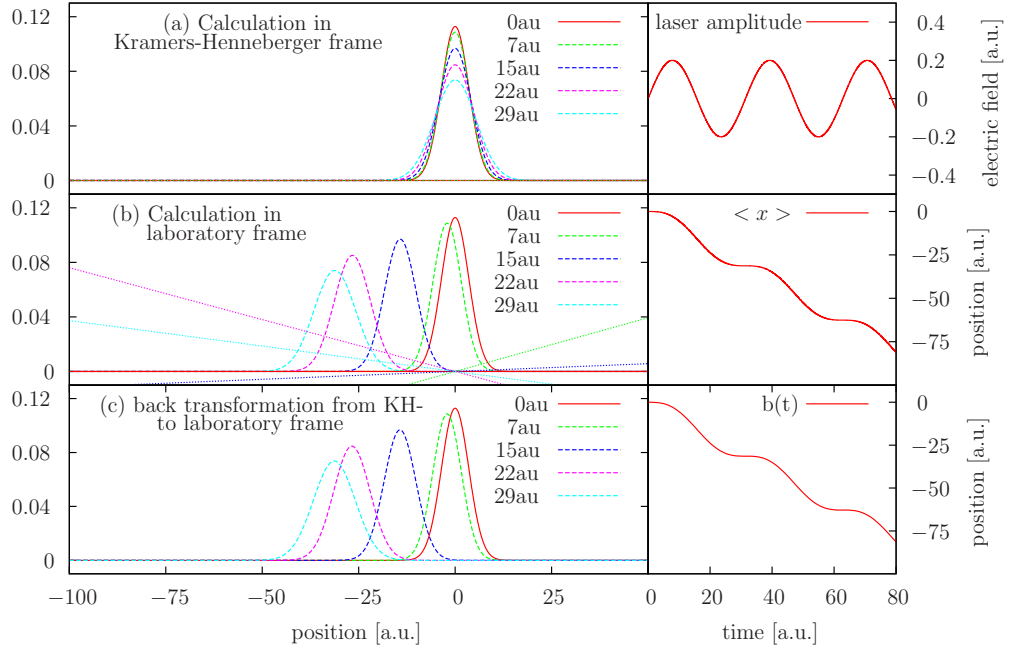


**Figure 3.4:** Behavior of a wave packet in a laser field. No additional potentials are included. Shown is a comparison between the calculation in the KH (a) and the laboratory frame (b). (a) can be transformed into (b) by applying a shift with  $b(t)$  which corresponds to the classical movement of the electron (c). The left figures show the density  $|\Psi(t)|^2$  for different times. The right figures display the laser excitation, the expectation value of  $x$  in the laboratory frame and the transformation function  $b(t)$  given by Eq. (3.50)

### 3.2.2 Back and forward transformation of the Kramers-Henneberger frame

The transformation to the KH frame is given by Eq. (3.43). The backward transformation to the laboratory frame can therefore be written as

$$\hat{U}^{-1} = \exp\left(\int_{-\infty}^t \frac{1}{c} \mathbf{A}(\tau) d\tau \nabla\right) \cdot \exp\left(-\frac{i}{2c^2} \int_{-\infty}^t \mathbf{A}^2(\tau) d\tau\right). \quad (3.47)$$

A free electron in a laser field  $E(t) = E_0 \cdot \sin(\omega t)$  illustrates the advantage of the KH-frame. First of all the vector potential  $\mathbf{A}$  for the chosen electric field is calculated:

$$\mathbf{A}(t) = -c \int_0^t \mathbf{E}(\tau) d\tau = \frac{cE_0}{\omega} [\cos(\omega t) - 1]. \quad (3.48)$$

The transformation operator  $\hat{U}_1$  evaluates to

$$\hat{U}_1 = \exp\left[-\frac{E_0}{\omega} \left(\int_0^t \cos(\omega\tau) d\tau - t\right) \nabla\right] = \exp\left[-\left(\frac{E_0}{\omega^2} \sin(\omega t) - \frac{E_0}{\omega} t\right) \nabla\right], \quad (3.49)$$

which corresponds to a shift of the density

$$b(t) = \frac{E_0}{\omega^2} \sin(\omega t) - \frac{E_0}{\omega} t. \quad (3.50)$$

$b(t)$  is exactly the classical shift of the electron. The phase transformation of the wave function is not important in this example. By applying the translation operator  $\hat{U}_1$  with the function  $b(t)$  both calculations yield the same results, as shown in Fig. 3.4. The mean value  $\langle x \rangle(t)$  calculated within the laboratory frame has exactly the same behavior as the translation function  $b(t)$ .

### 3.3 Calculation of expectation values

Several physical observables can be calculated from the wave function  $\Psi(t)$ . In the following, only 1D calculations are shown. The same methods apply to 2D systems if an additional integration variable for the  $y$ -direction is included. Diagonal operators are the simplest to calculate:

- normalization  $\Gamma$  of  $\Psi(x, t)$ :

$$\Gamma(t) = \int_{-\infty}^{\infty} |\Psi(x, t)|^2 dx \approx \sum_{i=1}^N |\Psi_i^n|^2 \cdot \Delta x, \quad (3.51)$$

- potential energy  $E_{\text{pot}}(t)$  with respect to the ionic potential (no laser field energy included):

$$E_{\text{pot}}(t) = \langle V \rangle(t) = \int_{-\infty}^{\infty} |\Psi(x, t)|^2 V(x) dx \approx \sum_{i=1}^N |\Psi_i^n|^2 V_i \cdot \Delta x, \quad (3.52)$$

- expectation value of  $x$

$$\langle x \rangle(t) = \int_{-\infty}^{\infty} |\Psi(x, t)|^2 x dx \approx \sum_{i=0}^n |\Psi_i^n|^2 x_i \cdot \Delta x. \quad (3.53)$$

Non-diagonal operators require more computational effort. For example the kinetic energy is calculated using two different methods:

First, it is obvious to use the relation

$$E_{\text{kin}}(t) = \left\langle -\frac{1}{2} \frac{d^2}{dx^2} \right\rangle_{\Psi(x,t)} = -\frac{1}{2} \langle \Psi | \Psi''(x, t) \rangle. \quad (3.54)$$

The main numerical task is to calculate the second derivative of  $\Psi(x, t)$ . The easiest way is the approximation by two applications of the difference quotient

$$f'(x) \approx \frac{f(x) - f(x + \Delta x)}{\Delta x}, \quad (3.55)$$

which is not very accurate.

An alternative procedure uses the wave function in momentum representation  $\Psi(k, t)$  which can be obtained via a Fourier transform of  $\Psi(x, t)$  with respect to the  $x$ -coordinate (Chapter 3.4.1). Within this representation the operator of the kinetic energy is diagonal thus no derivative is needed and its calculation is easy:

$$E_{\text{kin}}(t) = \left\langle \frac{k^2}{2} \right\rangle_{\Psi(k,t)} = \frac{1}{2} \int_{-\infty}^{\infty} dk |\Psi(k, t)|^2 k^2. \quad (3.56)$$

Since the fast Fourier transform (FFT) scales with  $\mathcal{O}(N \log N)$  this is the method of choice especially for large 2D systems.

Finally, an important value is the energy that is introduced into the system by an external laser field  $E_{\text{field}}$ . This quantity is of particular interest for testing the total energy conservation of the numerical scheme in dependence on the parameters  $\Delta x$  and  $\Delta t$ .  $E_{\text{field}}$  should be equal

to the energy gain  $\Delta E(t) = E_0 - E_{\text{kin}} - E_{\text{pot}}$  where  $E_0 = E(t = 0)$ . From the relation  $dW/dt = -\langle \dot{x} \rangle E(t)$  one obtains by integration by parts

$$E_{\text{field}}(t) = - \int_{t_0}^t d\bar{t} \langle x(\bar{t}) \rangle \left( \frac{\partial}{\partial \bar{t}} E \right) (\bar{t}) . \quad (3.57)$$

$E_{\text{field}}$  describes the energy being absorbed by the particle in the laser field. Thus the total energy of the whole system is given by

$$E_{\text{tot}} = E_{\text{kin}} + E_{\text{pot}} + E_{\text{field}} , \quad (3.58)$$

which should be constant during time propagation.

## 3.4 Energy spectra

For many situations the energy distribution of the propagated wave function is an interesting quantity. Two different methods are presented. The first can be applied easily to 1D systems and the second shows its advantages in at least two-dimensional systems.

### 3.4.1 Free particle spectrum

In one dimension, the energy spectrum can be obtained by transforming the wave function into momentum space via the Fourier transform with respect to the  $x$ -coordinate:

$$\Psi(k, t) = \frac{1}{2\pi} \int_{-\infty}^{\infty} dx \exp(ikx) \Psi(x, t) . \quad (3.59)$$

Using the free particle dispersion relation

$$E = \frac{k^2}{2m} \quad (3.60)$$

one can calculate the energy distribution  $\Psi(E)$  of the wave function. Now one big advantage of the KH-frame comes into play: The potential energy vanishes for regions outside the interaction, thus the particles are considered to be free and Eq. (3.60) can be applied. The direction of scattering is indicated by the sign of the energy. Scattering to the left is defined to give negative energies and scattering to the right results in positive energies.

This method obviously runs into problems if calculations are performed on a two-dimensional grid. One has to choose one-dimensional lines on the grid and calculate one-dimensional FFT spectra on those lines. But in this case interpolating routines have to be used. Within this work an alternative procedure is chosen.

### 3.4.2 Detecting scattered particles

A different way which allows to calculate angle-resolved spectra in two (and more) dimensions is to model a detector. This is simply done by storing the time-dependent wave function on selected grid points. To resolve an energy spectrum, a Fourier transform with respect to the time has to be performed:

$$\Psi(x, E) = \frac{1}{2\pi} \int_{-\infty}^{\infty} dt \exp(iEt) \Psi(x, t) . \quad (3.61)$$

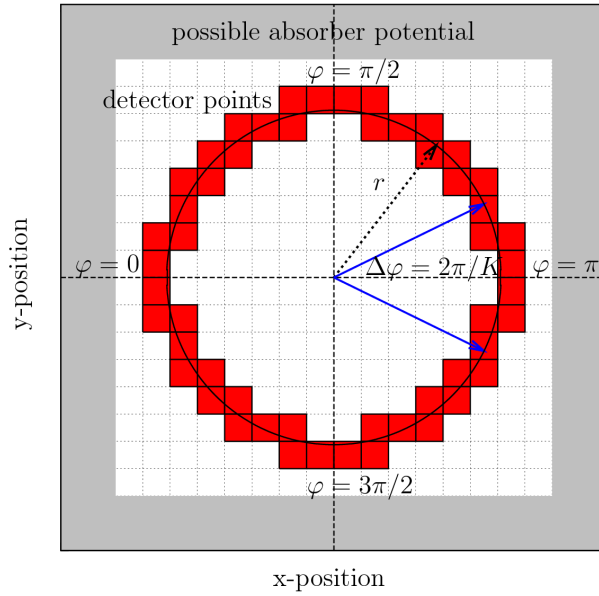


**Figure 3.5:** Geometry of the 2D detector. The wave function on the red marked grid points is stored during the simulation for all time steps. A Fourier transform with respect to time allows for the calculation of an angle and energy-resolved electron spectrum. The parameter  $K$  adjusts the angular resolution of the detector.  $K = 1$  represents the whole sphere and larger values of  $K$  increase the resolution  $\Delta\varphi$ . The angle  $\varphi$  denotes the direction of scattered particles.  $\varphi = 0$  and  $\varphi = \pi$  correspond to the  $x$ -axis to the left and right, respectively. The grey marked region displays the optional imaginary absorbing potential.

Fig. 3.5 shows the setup of a 2D circular detector. The radius  $r$  has to be large enough such that near field effects are excluded and an experimental situation is imitated. The variable  $K$  selects the detector resolution according to

$$\Delta\varphi = \frac{2\pi}{K} . \quad (3.62)$$

The introduced angle  $\varphi$  describes the direction of scattering:

$\varphi = 0$  indicates scattering to the left (negative  $x$  values),  $\varphi = \pi$  scattering to the right. A big advantage of this procedure is that the grid sizes can be much smaller if absorbing boundary conditions are included. No fully spatial resolution of the wave function is needed. Only some selected points of the detector are stored during the time propagation. However the amount of data to be saved and processed to gather information about all angles is large and can easily increase up to 20 GB for typical scattering simulations in two dimensions.

### 3.4.3 Comparison between both methods

A simple test of both detection methods is the calculation of a free particle energy spectrum. The 1D wave function of a free particle with  $k_0 = 1.0$  a.u. is propagated in time (Fig. 3.6). During its movement it runs over the detector. The time series on this specified grid point is recorded (lower figure). Applying both methods described above gives the same results and shows a maximum at the expected value of  $E = k_0^2/2 = 0.5$  a.u. The width of the energy distribution results from the finite time series as well as the finite spatial width of the wave packet. It agrees with Heisenberg's principle.

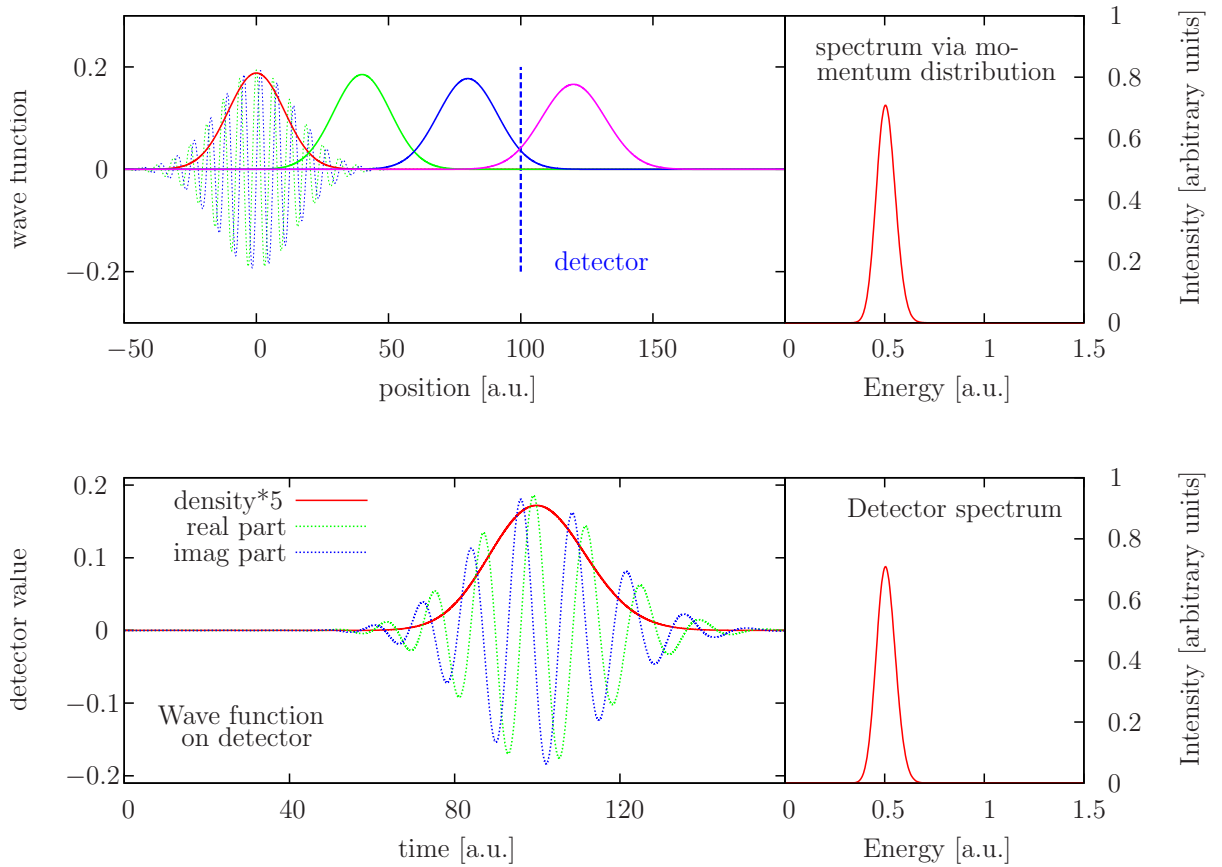


**Figure 3.6:** Energy spectrum of a free particle ( $k = 1.0$  a.u.). The upper left figure shows the time evolution on the spatial grid. The dashed blue line indicates the detector grid point at  $x = 100$  a.u. The lower left figure displays the time-dependent value on this selected grid point. The right figures give the energy spectrum of the particle: in the upper picture calculated via the momentum distribution (FFT with respect to the  $x$ -coordinate) and the free particle dispersion relation, Eq. (3.60), and in the lower figure via the detected wave function (FFT with respect to time  $t$ ). Both methods agree perfectly with the theoretical value  $k_0^2/2 = 0.5$  a.u.

### 3.5 Implementation in C

The methods described above are implemented in the programming language C. Fig. 3.7 shows the flow diagram of the main program parts. The input file *inp.ini* contains all information needed for a simulation run. A user manual and a commented input file come with the program package. The code compiles under Linux with the GNU g++ compiler. Due to a live-gnuplot viewing feature no other operating systems are supported. The FFT routines are taken from the GNU scientific library (gsl). Thus it is needed for successful linking. An additional analysis program (*analyse.out*) is available. It calculates the detector spectra and other expectation values after the simulation run. The compiling and linking is done simultaneously with the main program.

### 3 Numerical method

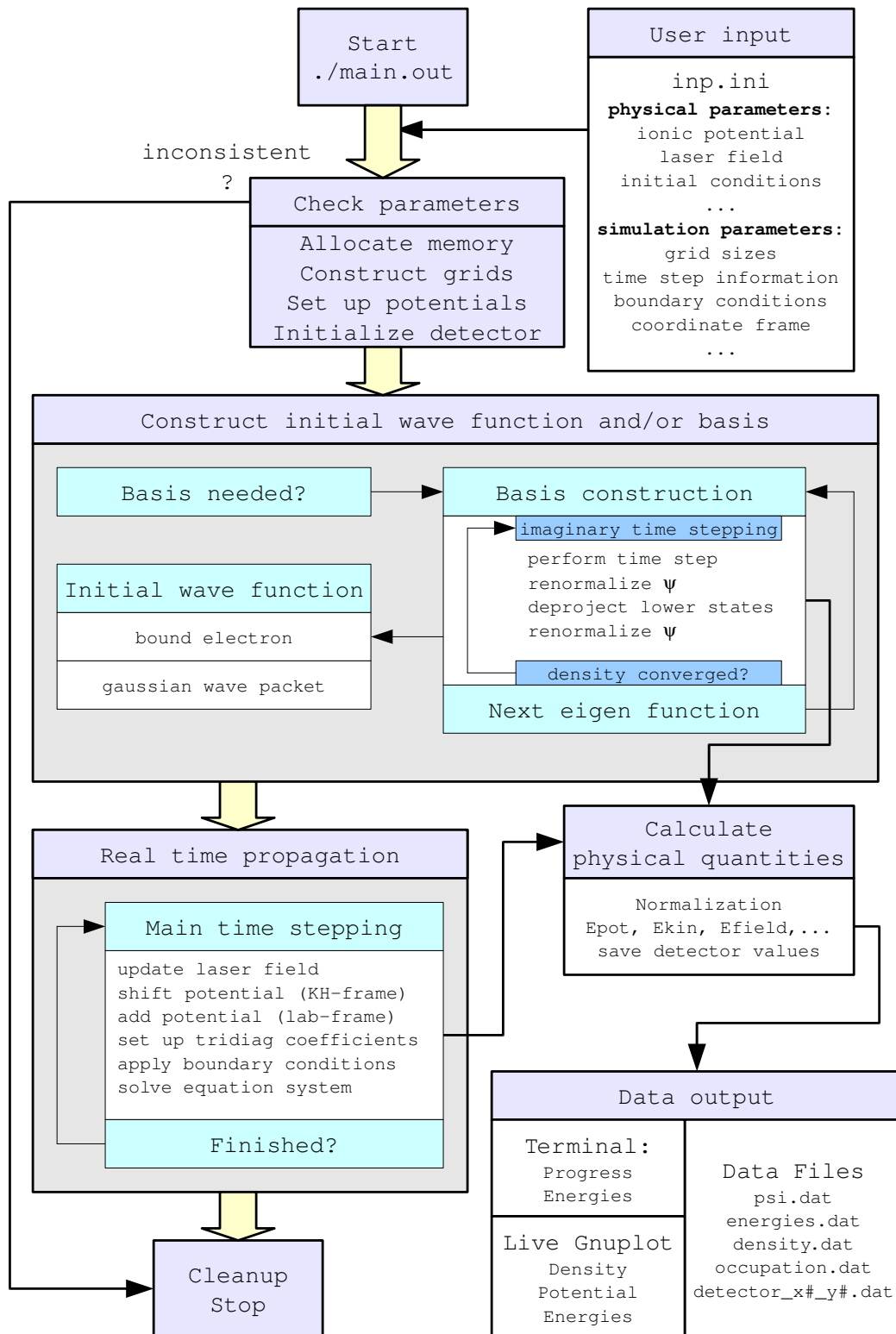


Figure 3.7: Flow chart of the C-program

## 4 Numerical concepts and basic calculations

This chapter begins with a discussion of selected numerical tests for the program introduced and described previously. The convergence behavior of the Crank-Nicolson algorithm depending on the parameters  $\Delta t$  and  $\Delta x$  is analyzed. Additionally, it was extensively tested on various other systems [43, 44]. All the results obtained agree with the well-known solutions for simple one-dimensional systems as well as for more complex multi-dimensional situations.

The second part of this chapter deals with useful concepts for numerical solutions of the TDSE like the wave packet scattering formalism. It closes with a discussion of the one- and two-dimensional Coulomb potential and its computational treatment in terms of a regularized soft-core potential.

### 4.1 Convergence behavior of the CN-Method

The convergence behavior of the Crank-Nicolson grid method concerning the spatial grid resolution  $\Delta x$  and the discretization in time  $\Delta t$  is essential. These two (user chosen) values are the free parameters of the numerical algorithm. They surely affect the accuracy of the solution and the efficiency of the algorithm. This kind of simulations always requires a compromise between running time and accuracy of the solution. As an example, well-known simple quantum systems are studied. The comparison of their analytical solution with the numerical treatment of the TDSE gives estimations of the optimal parameter ranges.

#### 4.1.1 1D harmonic oscillator

The first example checks the  $\Delta x$  and  $\Delta t$  dependence of the one-dimensional Crank-Nicolson procedure. A coherent state is prepared in a harmonic confinement,  $\Omega = 0.25$  a.u. (Fig. 4.1),

$$V(x) = \frac{1}{2}m\Omega^2x^2. \quad (4.1)$$

The first eigenstate [45]

$$\psi_0 = \frac{1}{\sqrt{\sigma}\sqrt{\pi}} \exp\left(-\frac{1}{2}\frac{x^2}{\sigma^2}\right), \quad (4.2)$$

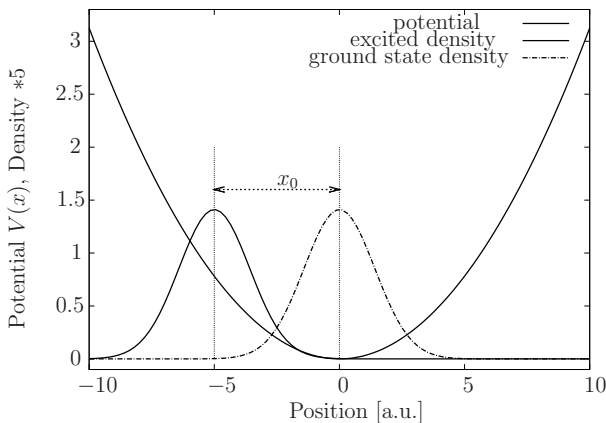


**Figure 4.1:** Convergence tests: Schematic view of the system. The ground state  $\psi_0$  of a harmonic oscillator,  $\Omega = 0.25$  a.u., is displaced to the position  $x_0 = 5.0$  a.u. (coherent state)

#### 4 Numerical concepts and basic calculations

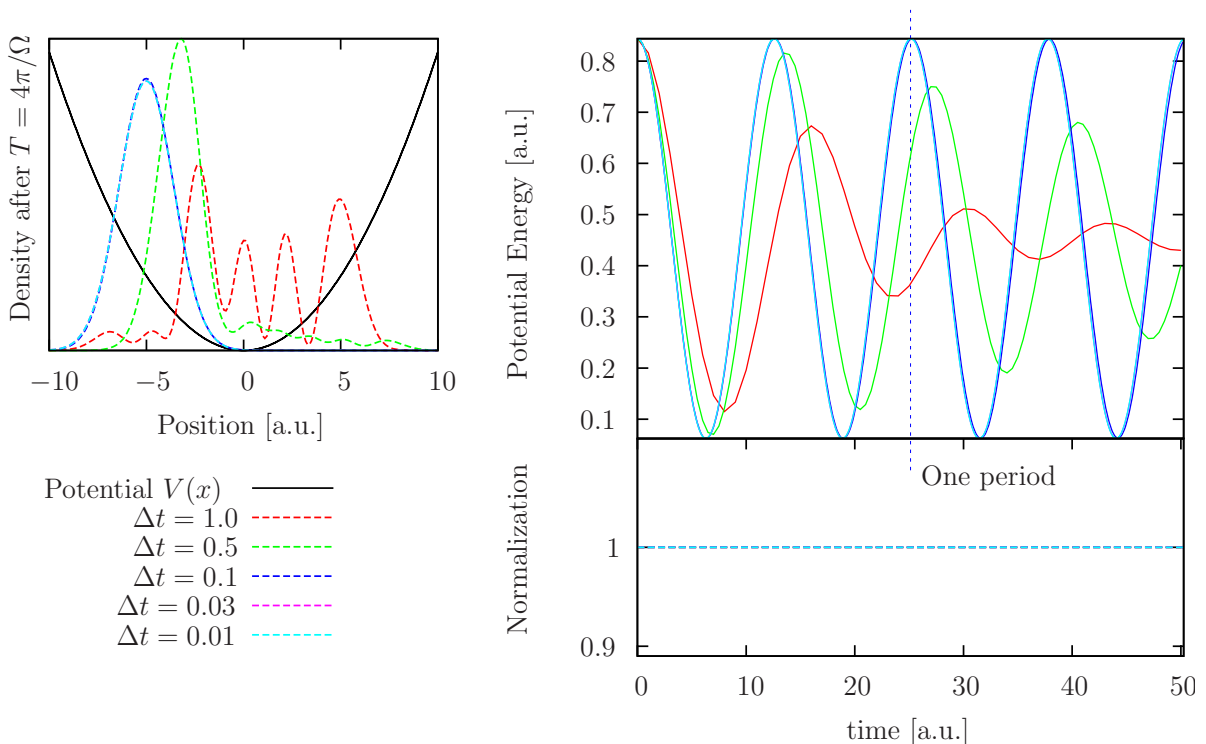


**Figure 4.2:** Behavior of the one-dimensional Crank-Nicolson method for different  $\Delta t$ .  $\Delta x = 0.1$  is fixed. The left figure shows the density of a coherent state in a harmonic confinement after two complete oscillations ( $T = 4\pi/\Omega$ ). The time evolution of the potential energy and normalization is shown in the right panel. The blue dashed line indicates the expected accurate period.

with  $\sigma = 1/\sqrt{\Omega} = 2.0$  a.u. is displaced to  $x_0 = -5.0$  a.u. from the center of the trap. It performs a harmonic oscillation with the frequency  $\Omega$  of the external potential without any deformation of its initial Gaussian shape. The potential energy  $E_{\text{pot}}$  oscillates with twice the trap frequency, i.e., a period of  $T = \pi/\Omega = 4\pi$ . Figure 4.2 shows the behavior of the TDSE solution for different time step sizes  $\Delta t$  for a fixed spatial grid resolution ( $\Delta x = 0.1$ ).

The final density after  $T = 4\pi/\Omega$  and the oscillation of the potential energy show a strong dependence on  $\Delta t$ . For large time steps it is deformed due to an occurring decoherency of the state. Furthermore, the potential energy shows a strong damping and a shift of its period. This is a direct result of insufficient numerical accuracy. The influence of the spatial step size is not as dramatic although for very large  $\Delta x$  the spatial oscillations of the wave function are too fine for the chosen accuracy. Since the Crank-Nicolson method is unconditionally stable and unitary, the normalization of the wave function equals one for all  $\Delta t$  and  $\Delta x$ . Therefore this observable does not have any practical information concerning the accuracy of the simulation.

Figure 4.3 shows the error in the total energy depending on  $\Delta t$  and  $\Delta x$  after a time propagation for two complete oscillations. Decreasing the spatial step size increases the accuracy of the simulation with a power law behavior (second order). The dependence on  $\Delta t$  shows a different behavior. The accuracy cannot be increased below a significant step size depending on  $\Delta x$ . Hence if the time-dependent characteristics are resolved accurately enough, only the spatial step size affects the total result. For the specific problem shown above,  $\Delta t = 0.03$  and  $\Delta x = 0.1$  are a good compromise between computational effort and accuracy.

An analogous calculation for the behavior of externally excited systems (eigenstate in a dipole laser field) leads to the same values for  $\Delta t$  and  $\Delta x$ . Calculations with these parameters are shown in Chapter 5. This check does of course not imply universality. The obtained parameters

#### 4.1 Convergence behavior of the CN-Method

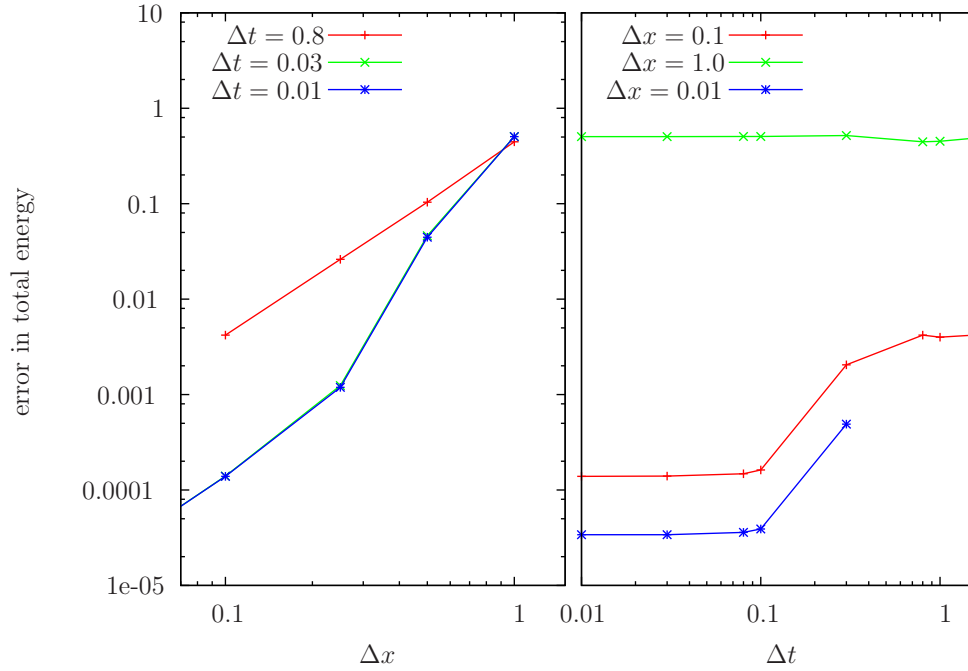


**Figure 4.3:** Error in the total energy depending on  $\Delta x$  (left figure) and  $\Delta t$  (right figure) for an oscillating coherent state in a harmonic confinement (cf. Figs. 4.1 and 4.2) after time propagation of the TDSE for two complete periods. In the left (right) picture  $\Delta t$  ( $\Delta x$ ) is fixed for each curve.

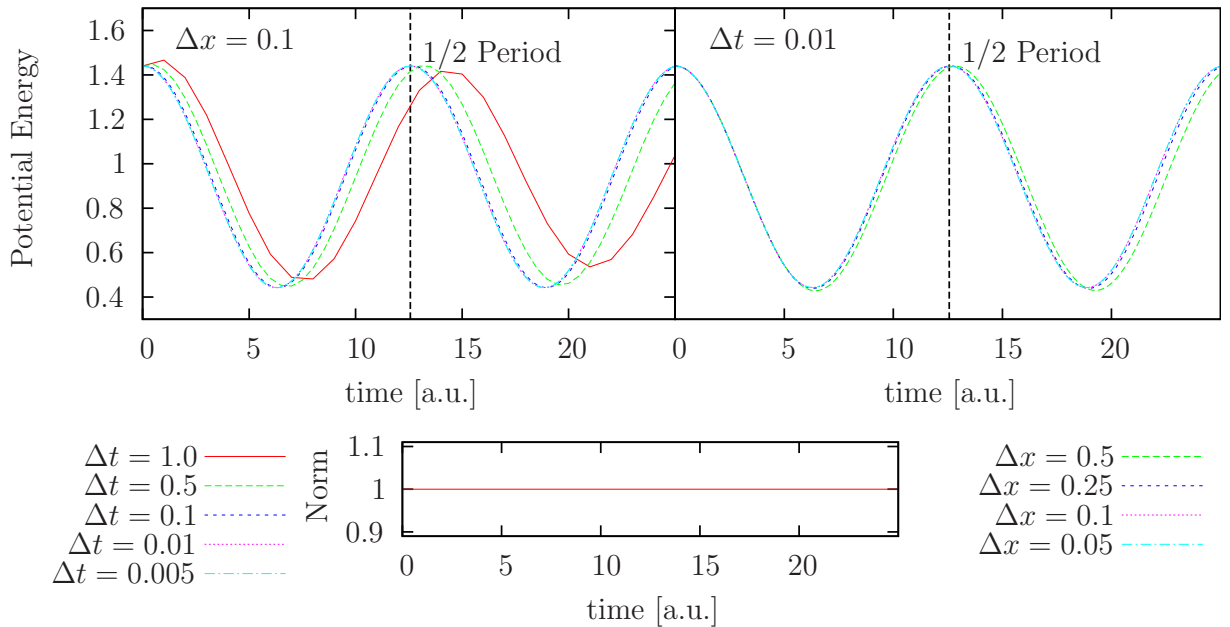


**Figure 4.4:** Convergence behavior of the 2D operator splitting method for a coherent state in a harmonic oscillator potential. The potential energy for different  $\Delta t$  (left figure) and  $\Delta x$  (right figure) is shown. The dashed line denotes the correct period. The normalization for all  $\Delta x, \Delta t$  is given in the lowest figure.

## 4 Numerical concepts and basic calculations

give only a possible range. The convergence behavior, e.g. spectral features independent of  $\Delta t$  and  $\Delta x$  etc., should be tested separately for each system studied. Otherwise, numerical artefacts may influence the physical solution.

### 4.1.2 2D harmonic oscillator

The TDSE in more than one dimension is solved via the operator splitting method (cf. Chapter 3.1.2). Therefore a different dependence on the simulation parameters is expected. The time propagation of a coherent state in a two-dimensional harmonic oscillator potential

$$V(x, y) = \frac{1}{2}m\Omega^2(x^2 + y^2), \quad (4.3)$$

$\Omega = 0.25$  a.u., is investigated. The dynamics of the first eigenstate excited to  $(x_0, y_0) = (-3.0, 0.0)$  for one oscillation period  $T = 2\pi/\Omega = 8\pi$  again depend on  $\Delta x = \Delta y$  and  $\Delta t$ . As in the one-dimensional example the potential energy oscillates with twice the trap frequency. Figure 4.4 shows the time evolution of the potential energy and the normalization for different parameters. A strong dependence on the time step size is visible. The potential energy oscillates with a wrong frequency and undergoes a damping for large  $\Delta t$  (decoherency effect like in the 1D case). The influence of the spatial grid resolution  $\Delta x$  is smaller. The optimal parameter for the spatial resolution can be identified as  $\Delta x = \Delta y = 0.1$ . Since the operator splitting method performs two independent one-dimensional steps in each direction this result agrees with the 1D harmonic oscillator. For the time step size  $\Delta t = 0.01$  is derived. This is no surprising result because the two-dimensional method consists of three sub steps where each one is calculated with a step size of  $\Delta t/3$ .

## 4.2 Wave packet scattering

A central method used widely in this work is based on wave packet scattering. In the following a short introduction to this formalism and its results compared to usual quantum approaches are given. Although many calculations, especially for packets of Gaussian shape, can be performed analytically, in this work all results have been resolved by using the numerical solution of the TDSE since this method can be applied to arbitrary scattering geometries.

### 4.2.1 Method

The main focus of this work lies on wave packets with a Gaussian shape. In the 1D case it is given by

$$\Psi(x, 0) = \frac{1}{\sqrt{2\pi}\sigma} \exp\left(-\frac{(x-x_0)^2}{2\sigma^2}\right) \exp(ik_0x). \quad (4.4)$$

The parameters are:

- $\sigma$ : initial width of the wave packet
- $k_0$ : initial momentum of the wave packet
- $x_0$ : initial position of the wave packet center

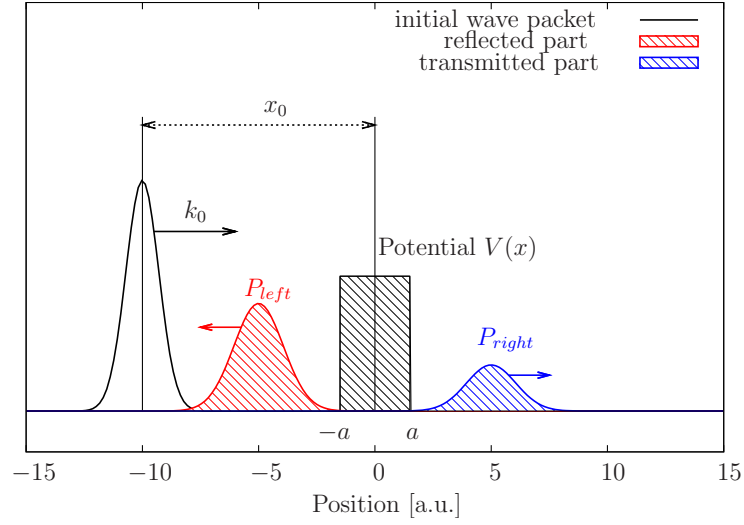


**Figure 4.5:** Wave packet scattering setup. The initial packet with the width  $\sigma$  is located at  $x_0$  left of a potential whose scattering features are analyzed. It has the initial momentum  $k_0$  travelling to the right towards the potential. After the scattering process the wave packet has separated into a reflected and a transmitted part.

Central properties of potentials in quantum systems are the transmission and the reflection coefficient - especially for scattering situations. These fundamental values can be calculated using wave packets via

$$P_{\text{left}}(t^*) = \int_{-\infty}^{-a} |\Psi(x, t^*)|^2 dx, \quad P_{\text{right}}(t^*) = \int_a^{\infty} |\Psi(x, t^*)|^2 dx, \quad (4.5)$$

where  $P$  describes the probability of finding the particle left or right of the scattering region (Fig. 4.5). These probabilities directly correspond to the transmission/reflection coefficients, if  $\Psi$  is normalized to one and the time  $t^*$  is chosen long enough after the scattering process. An important free parameter is the width of the wave packet which plays an important role for the energy resolution of the values. This can be illustrated with the next example.

### 4.2.2 Simple application: the potential well

The best-known system from standard quantum mechanics is the potential well. Figure 4.6 (b) illustrates the system and introduces the used parameters. The analytical result for the transmission coefficient of the potential well describes resonances in the region of the eigenstates of the infinite-depth potential well. Their energies are calculated via

$$E_n = \frac{n^2 \pi^2}{8a^2} - V_0. \quad (4.6)$$

$V_0$  is the depth of the potential well of width  $2a$ . The corresponding momentum of a wave packet is given by

$$k_n = \sqrt{2E_n} = \sqrt{2 \left( \frac{n^2 \pi^2}{8a^2} - V_0 \right)}. \quad (4.7)$$

The transmission coefficient shows resonance maxima for initial momenta  $k_0$  around  $k_n$ . In the calculations  $V_0 = 2.88$  and  $a = 2.5$  are used ( $\Delta x = 0.1$ ,  $\Delta t = 0.03$ ). The variation of  $\sigma$  for the initial wave packet results in different energy resolutions [Fig. 4.6 (a)] since the spatial width

## 4 Numerical concepts and basic calculations

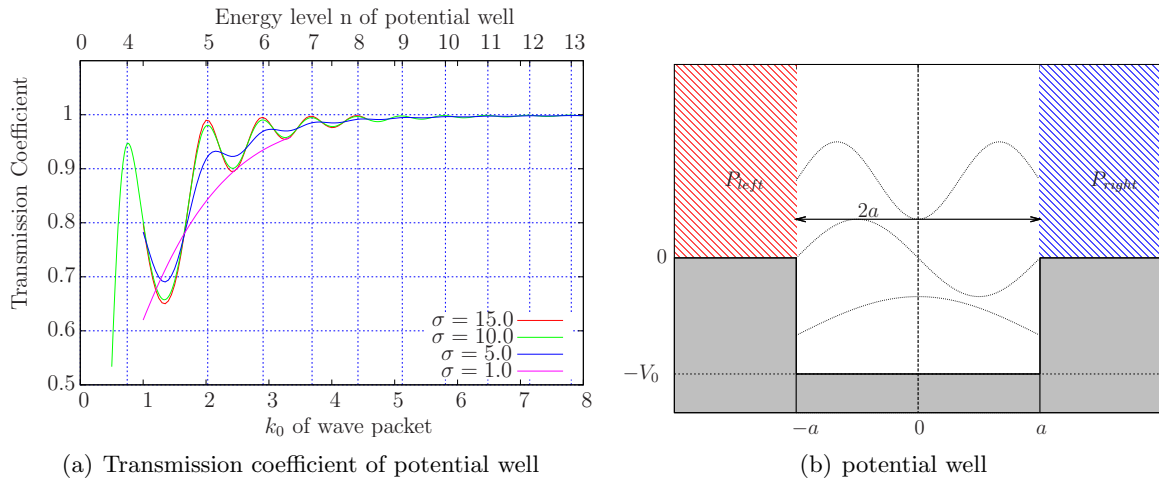


**Figure 4.6:** Transmission coefficient of potential well calculated via wave packet scattering. The width  $\sigma$  of the wave packet has been varied. The influence on the energy resolution is obvious. The smaller the wave packet on the spatial grid the lesser is the energy resolution. Finally, all resonance peaks (analytical calculation) are disappearing ( $\sigma = 1.0$ ). Note: The abscissa displays  $k_0$  and not  $E$  as usual.

of the wave packet is connected with its momentum spreading. Thus its energy uncertainty depends on  $\sigma$  via a Fourier transform (Heisenberg principle). Therefore the expected sharp resonance peaks of the transmission coefficient are smeared out within the wave packet scattering approach. The smaller  $\sigma$  the less significant details of energy-dependent scattering properties can be resolved. This is truly a fundamental limiting factor especially for large two-dimensional systems. The wave packet has to be chosen as small as possible to reduce the computation time and large enough to gain a sufficient energy resolution.

### 4.3 The regularized Coulomb potential

The Coulomb potential plays an important role throughout this work. Thus, it is essential to investigate its properties very carefully. For computational reasons the *regularized* Coulomb potential

$$V(x) = -\frac{Z}{\sqrt{x^2 + \kappa^2}} \quad \text{resp.} \quad V(x, y) = -\frac{Z}{\sqrt{x^2 + y^2 + \kappa^2}} \quad (4.8)$$

is introduced. It avoids numerical divergences at the location of the ion but leads to some non-trivial complications concerning the eigenstates and eigenenergies.  $Z$  is the atomic number of the ion and  $\kappa$  a small cut-off parameter.  $\kappa$  prevents the singularity at  $x = 0$  which occurs in the pure Coulomb case. Fig. 4.7 (a) shows the potential for different  $\kappa$ . The minimum of the potential energy at the origin  $x = 0$  is obviously  $-1/\kappa$ .

#### 4.3.1 Transmission and reflection

Using the wave packet scattering method it is possible to calculate the transmission and reflection properties of the potential. Fig. 4.7 (b) shows the reflection coefficient for different regularization parameters. Obviously, the reflection increases enormously if the potential is tuned to be more Coulomb-like. Secondly, one recognizes that this value monotonically depends on  $k_0$  of the incident wave packet: The faster the particle, the less probable it will be reflected by the potential. This becomes an important statement for the understanding of multiple scattering

### 4.3 The regularized Coulomb potential

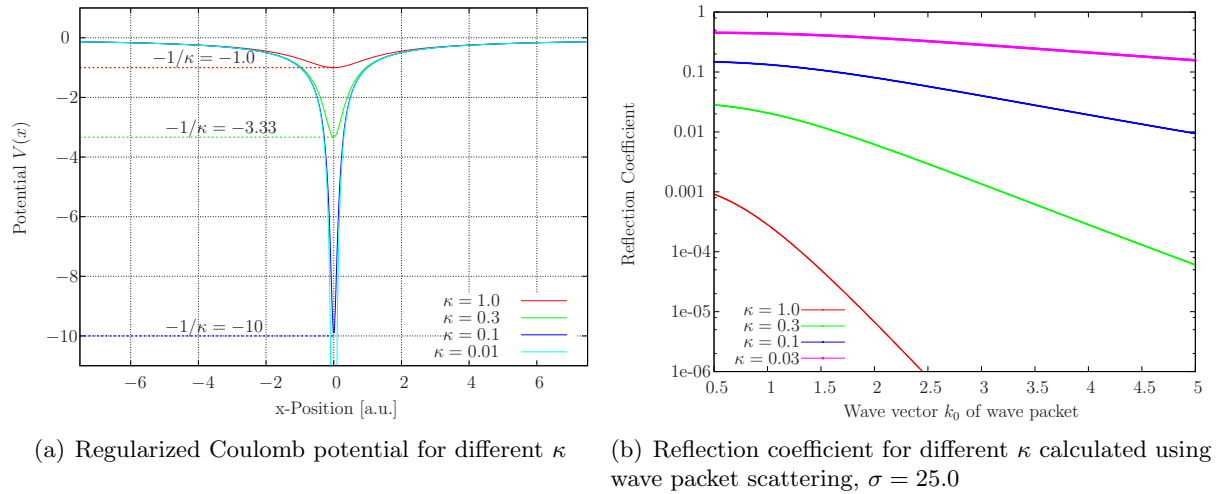


**Figure 4.7:** The regularized 1D Coulomb potential for  $Z = 1.0$  and different  $\kappa$ .

events in the presence of more than one Coulomb potential and the probability of these multiple scattering events (Chapter 6).

#### 4.3.2 1D eigenstates

To understand the underlying problem for the regularized Coulomb potential, Eq. (4.8), it is a good starting point to investigate the properties of the pure one-dimensional Coulomb potential

$$V(x) = -\frac{Z}{|x|}. \quad (4.9)$$

The important aspect here is the modulus function which results in a reflection symmetry around the singularity at  $x = 0$ . The eigenfunctions can be calculated as usual, starting from the one-dimensional time-independent Schrödinger equation

$$-\frac{1}{2} \frac{d^2}{dx^2} \psi_n(x) - \frac{1}{|x|} \psi_n(x) = E_n \psi_n(x). \quad (4.10)$$

This equation has to be solved for the regions  $x > 0$  and  $x < 0$  separately. The main problem now is the combination of the two solutions in the singular point of the potential. A basic discussion of the form of the total wave function can be given in terms of quantum mechanical arguments.

In order to be able to construct even and odd wave functions, i.e., forming a complete set of eigenfunctions, there have to exist solutions that are of even and of odd parity [ $\psi_{\text{even}}(x) = \psi_{\text{even}}(-x)$  and  $\psi_{\text{odd}}(x) = -\psi_{\text{odd}}(-x)$ ]. By introducing a small cut-off parameter [for example as in Eq. (4.8)] one can start from the Sturm-Liouville theorem. It states that a one-dimensional potential has a nodeless even ground state wave function. The excited states are alternating between odd and even parity and are not degenerate, as can be proven for any non-singular one-dimensional potential (see Appendix E). But if now the cut-off tends to zero ( $\kappa \rightarrow 0$ ) even and odd states are affected differently: For odd states,  $\psi_{\text{odd}}(0)$  vanishes so there is no influence of the singular behavior of  $V(x)$ . But for the even states, since  $\psi_{\text{even}}(0)$  is finite, the second derivative has to be infinite and the slope of the even wave functions has to be discontinuous. Now, the even and the odd wave states are constructed from the same functions but are connected differently at the singular point of the potential. This creates a degeneracy of even and

#### 4 Numerical concepts and basic calculations

odd states in the pure Coulomb case. The ground state wave function plays a different role: It is non-degenerate and its density forms a  $\delta$ -distribution at the origin.

Finally, the eigenstates of the one-dimensional pure Coulomb potential can be calculated explicitly. The mathematical treatment is rather involved, details can be found in [46]. The final solution has been calculated via a limiting process by using the regularized Coulomb potential  $V(x) = -Z/(\alpha + |x|)$  which shows the same features as the potential used within this work. The wave functions are given in atomic units,  $L_n^1$  denotes the associated *Laguerre* polynomial  $L(n-1, x)$ :

- odd normalized states:

$$\psi_n(x) = \sqrt{\frac{2}{n^5(n!)^2}} \exp\left(-\frac{|x|}{n}\right) x L_n^1(2|x|n), \quad (4.11)$$

- even normalized states:

$$\psi_n(x) = \sqrt{\frac{2}{n^5(n!)^2}} \exp\left(-\frac{|x|}{n}\right) |x| L_n^1(2|x|n), \quad (4.12)$$

- ground state:

$$\psi = \lim_{\alpha \rightarrow 0} \frac{1}{\sqrt{\alpha}} \exp\left(-\frac{|x|}{\alpha}\right), \quad (4.13)$$

which leads to a density localized at  $x = 0$ :

$$|\psi(x)|^2 = \delta(x). \quad (4.14)$$

This state has an infinite binding energy and clearly no physical meaning. However it appears to be present in the numerical calculations for the regularized potential with  $\kappa \neq 0$ .

The energy eigenvalues (in atomic units) of the pure Coulomb potential follow a Balmer-like law:

$$E_n = -\frac{1}{2} \frac{1}{n^2}. \quad (4.15)$$

Hence, the first two eigenfunctions ( $E_1 = -0.500$  a.u.) besides the ground state read:

- first odd wave function, Eq. (4.11) with  $n = 1$ :

$$\psi(x) = \sqrt{2} \exp(-|x|) \cdot x \cdot L_1^1(2x) = \sqrt{2} \exp(-|x|) \cdot x, \quad (4.16)$$

- first even wave function, Eq. (4.12) with  $n = 1$ :

$$\psi(x) = \sqrt{2} \exp(-|x|) \cdot |x| \cdot L_1^1(2x) = \sqrt{2} \exp(-|x|) \cdot |x|. \quad (4.17)$$

These two functions are displayed in the upper right picture in Fig. 4.8 (b).

In order to construct the correct bound states for excitation processes, the eigenfunctions of the regularized potential have been investigated with the imaginary time stepping and the shooting method. The results are given in Figs. 4.8 and 4.9. The behavior of the eigenvalues and the wave functions discussed above becomes clearly visible. For small cut-off parameters

### 4.3 The regularized Coulomb potential

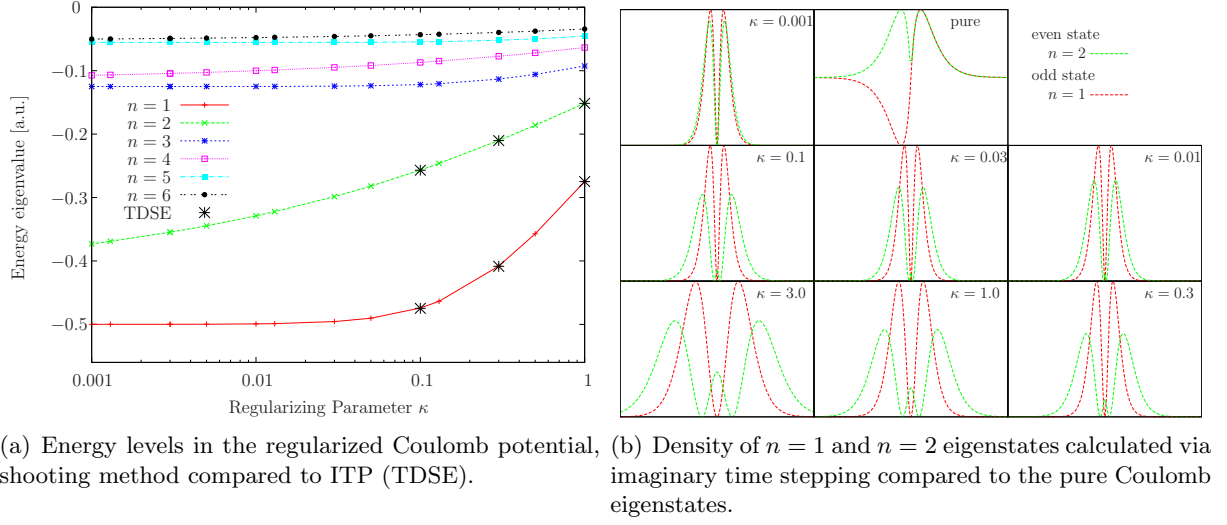


**Figure 4.8:** Behavior of the eigenstates of the 1D regularized Coulomb potential depending on  $\kappa$ . The occurring degeneracy of the odd and even wave functions becomes clearly visible for small  $\kappa$ . The analytical energy eigenvalues calculated with Eq. (4.15) are

n	0	1,2	3,4	5,6	7,8
$E_n$	$-\infty$	-0.500	-0.125	-0.0555	-0.03125

and in perfect agreement with the numerical results for the eigenvalues of the odd wave functions with very small  $\kappa$ . The pure Coulomb eigenfunctions are given by Eqs. (4.16) and (4.17).

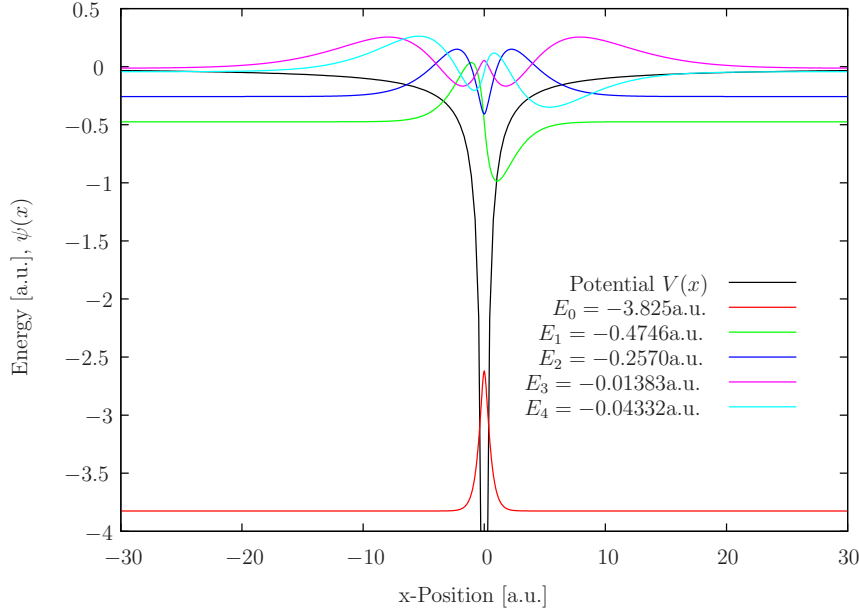


**Figure 4.9:** First five eigenfunctions of the regularized Coulomb potential ( $\kappa = 0.1$ ) calculated with the imaginary time stepping method. The deeply bound ground state wave function is an artefact of the regularization. Each odd wave function is followed by an even wave function with a weaker binding energy and a non-vanishing probability amplitude in the center of the potential. In the pure Coulomb case each pair has the same binding energy.

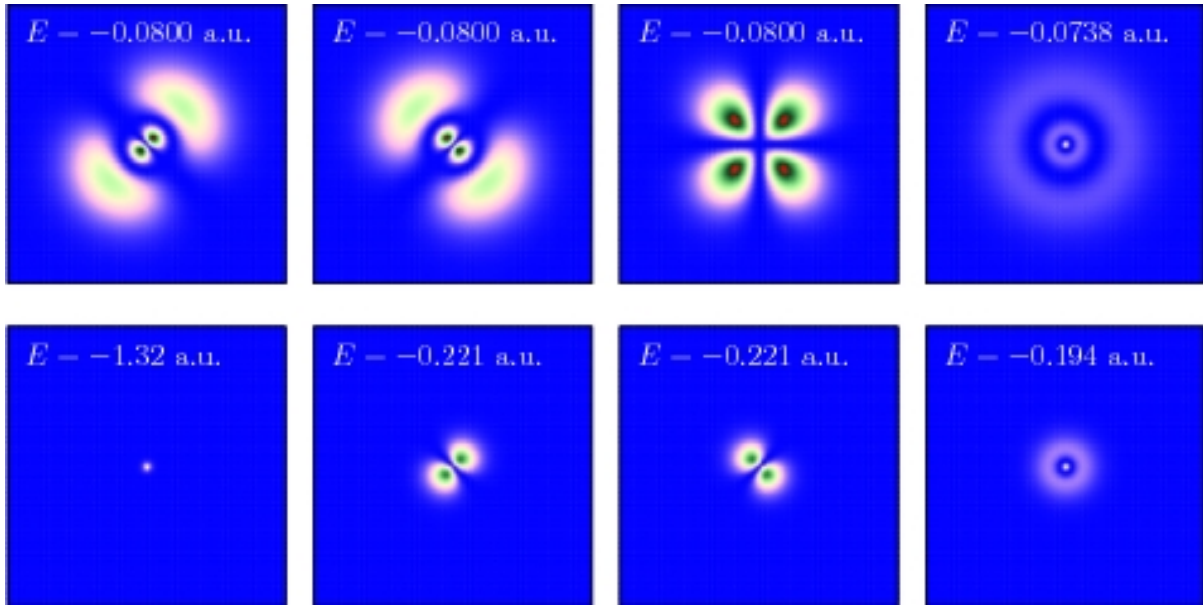


**Figure 4.10:** First eight eigenfunctions (density plot) of the 2D regularized Coulomb potential,  $\kappa = 0.1$ , calculated via the 2D imaginary time stepping algorithm. The structure of the eigenfunctions and the broken degeneracy of the  $s$ - and  $p$ -orbitals ( $n = 2$ ) and of the  $s$ -,  $p$ - and  $d$ -orbitals ( $n = 3$ ) due to the regularization is visible. The topology of the eigenfunctions is nearly the same as for the 3D hydrogen atom. From bottom left to top right (decreasing binding energy): deeply bound, unphysical ground state ( $E = -1.32$  a.u.) being followed by  $p_x$ - and  $p_y$ -like orbitals (perfectly degenerate,  $E = -0.221$  a.u.). With slightly smaller binding energy ( $E = -0.194$  a.u.) the  $s$ -wave function is located, exhibiting a non-vanishing density at the center. In the upper row, again the two  $p_x$ - and  $p_y$ -like states and additionally a  $d$ -state is found. These three states show a perfect degeneracy ( $E = -0.0800$  a.u.). Finally, the energetically higher  $s$ -state, again with a finite probability distribution at the center, is given.

$\kappa$  the eigenfunctions appear in pairs with nearly degenerate energies. In  $\kappa$  regions used for calculations later in this work ( $\kappa = 0.1$ ), these eigenfunctions have to be treated independently. They represent two eigenstates of a bound electron with completely different binding energy. In the following the first *odd* state (state with the lowest energy besides the artificial ground state) will be treated as the physical ground state although it is not a nodeless wave function as it is claimed by the Sturm-Liouville theorem.

### 4.3.3 2D eigenstates

Investigating ionization and scattering processes in more than one dimension requires to know the eigenstates of the 2D Coulomb potential. Again, it is essential for the numerical treatment to use the regularized potential [cf. Eq. (4.8)]. Like in the 1D case this produces a characteristic behavior of the eigenvalues and eigenfunctions. Especially the ordering of the energies and the degeneracy of the eigenfunctions are affected.

The construction of the wave functions is done with the ITP-procedure described in Chapter 3.1.5. The shooting method cannot be applied to this problem. Fig. 4.10 shows the first eight eigenfunctions (density plot) of the two-dimensional regularized Coulomb potential ( $\kappa = 0.1$ ). The first state is, as in the 1D case, a non-physical  $\delta$ -like artefact state of the regularization with a very high binding energy. The energetically higher states show a hydrogen-like structure but without the well-known perfect degeneracy. First the two-fold degenerated  $p$ -like states occur ( $p_x$ - and  $p_y$ -like states) being followed by a higher energetic non-degenerate  $s$ -state. In the true

### 4.3 The regularized Coulomb potential

Coulomb case these orbitals should all have the same binding energy. The explanation of this behavior can be given in analogy to the one-dimensional regularized Coulomb potential: The non-vanishing probability to find the electron at the core (finite potential energy at the origin) for the  $s$ -state leads to a significant difference to the  $p$ -states where the wave function vanishes at the potential minimum (singularity in the pure Coulomb case). The calculations have been performed on a  $750 \times 750$  grid with  $i \cdot \Delta t = 0.01$  and  $\Delta x = \Delta y = 0.1$  using the density as a convergence indicator with  $\Delta \xi = 1 \cdot 10^{-7}$ , cf. Eq. (3.38). The convergence of the total energy is *not* sufficient in this case.

## 4 *Numerical concepts and basic calculations*

# 5 Excitation and ionization in laser fields

In this chapter excitation and ionization processes of model atoms in dipole laser fields are discussed. In the first part effects in the perturbative regime are presented. Numerical TDSE calculations are compared to analytical results based on perturbation theories (Fermi's golden rule) and dipole matrix arguments. Both 1D and 2D systems are considered. The second part is dedicated to multi-photon processes and above threshold ionization in strong laser fields. A comparison between TDSE calculations and the strong field approximation (SFA) is given. The last part focuses on scattering processes with slow electrons ( $k_0 = 0$ ) which also leads over to the next chapter "Coulomb scattering" in laser fields.

## 5.1 Weak laser fields

First we want to study the influence of a weak laser field, i.e., low-intensity pulses, on electrons in bound states of simple model systems. For that purpose it is useful to consider the time-dependent occupation numbers. The TDSE is solved on a spatial grid as described in Chapter 3 and the resulting wave function  $\Psi(t, x)$  is projected onto the eigenstates of the ionic potential at each time step. The set of eigenstates is constructed using the imaginary time stepping algorithm. Then the occupation number for the state  $n$  is simply given by

$$\text{occ}(n, t) = |\langle \psi_n | \Psi(t) \rangle|^2 = \left| \int_{-\infty}^{\infty} d^3\mathbf{r} \psi_n^*(\mathbf{r}) \cdot \Psi(\mathbf{r}, t) \right|^2. \quad (5.1)$$

Since the calculations are performed on a spatial grid, a good representation of the continuum states is available. This is especially important for ionization problems, for instance in the case of the Coulomb potential. The calculations in the natural orbital representation of the binding potential can lead to problems concerning the representation of free electron states.

For all the simulations presented in the following, a Gaussian shaped laser excitation of the form

$$V_{\text{laser}}(t, x) = E_0 x \cos \omega t \cdot \exp\left(-\frac{1}{2} \frac{(t - t_0)^2}{(\Delta t)^2}\right) \quad (5.2)$$

is used. The electrical field is linearly polarized along the  $x$ -direction.  $E_0$  denotes its amplitude and  $\omega$  the light frequency. The pulse is centered around the time  $t_0$  where the pulse exhibits its maximum (cf. Fig. 5.1). The parameter  $\Delta t$  adjusts the pulse duration. According to Chapter 2.2.2, Eq. (5.2) corresponds to an interaction Hamiltonian in field gauge within the dipole approximation.

### 5.1.1 Excitation of the harmonic oscillator

The one-dimensional harmonic oscillator gives the opportunity to study the reaction of a simple quantum system to time-dependent external excitations. A trap frequency of  $\Omega = 1/8$  is chosen and the system is initially prepared in the ground state. The energy levels are all equidistant and separated by the energy  $\Omega$ . Fig. 5.1 shows the excitation behavior for two different laser pulses. Both are centered at  $t_0 = 240.0$  a.u. with  $\Delta t = 50$  and an amplitude  $E_0 = 0.01$  a.u. but

## 5 Excitation and ionization in laser fields

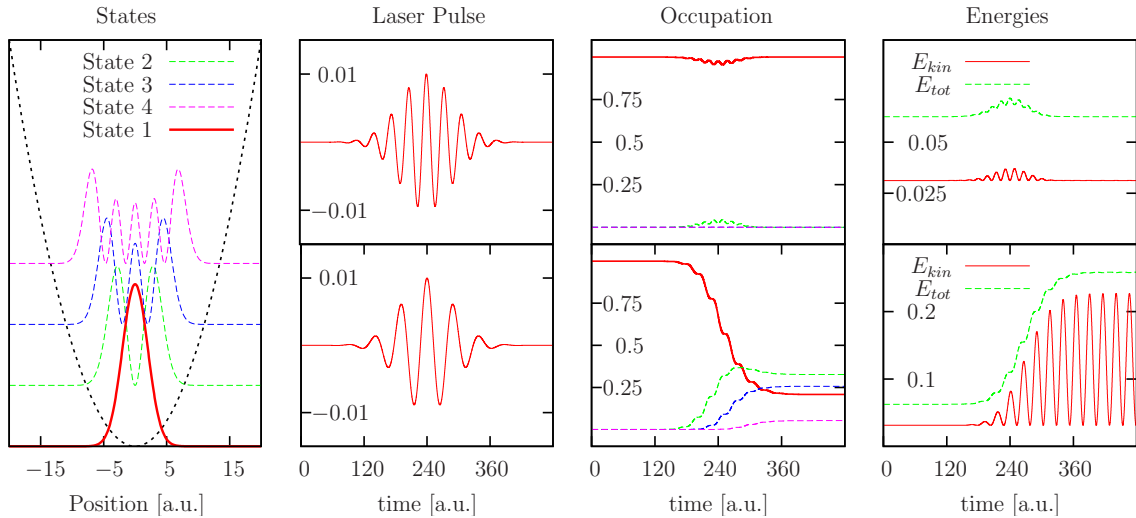


**Figure 5.1:** Laser excitation of the ground state of a one-dimensional harmonic oscillator (trap frequency  $\Omega = 0.125$ ). The first four states are shown in the left figure. Two different Gaussian shaped laser pulses are used: one resonant pulse with  $\omega = \Omega$  (lower figures) and one off-resonant pulse with  $\omega = 0.1875$  (upper figures). The right figures display the time-dependent properties during the excitation: the occupation numbers and the energies in the system.

differ in frequency.

The first one ( $\omega = 0.1875 \neq \Omega$ ) is not able to excite the system (upper figures) although during the pulse a small change in the occupation numbers and the energies can be observed. The laser field accelerates the particle in the potential but after one cycle it acts against this motion and decelerates it again thus the total energy gain after the symmetric pulse is zero and the final state has exactly the same shape as initially prepared.

For the second pulse ( $\omega = \Omega$ ) the situation is totally different. The dipole field acts resonantly and stores energy during each cycle of the pulse. Hence the total energy is increased. After the excitation, the system is in a superposition of energetically higher states and the density performs a harmonic oscillation because the dipole-field can only couple to the center of mass (c.m.) motion. The Gaussian shape of the initial wave function is not distorted during this process. The time-dependent behavior of the occupation numbers is of special interest. Since only dipole transitions<sup>1</sup> are allowed, we expect that the energy levels are filled subsequently one after another starting with the first excited state. The TDSE calculations clearly verify this result. At the beginning the ground state is depopulated while the first excited state is filled. Then the electron can be lifted from this level to the next higher one and so on.

### 5.1.2 Excitation and ionization phenomena of the 1D Coulomb potential

To include ionization features we now turn our attention to the one-dimensional Coulomb potential. We concentrate on the regularized potential [cf. Eq. (4.8)] with  $\kappa = 0.1$ . The expected processes differ from the excitation in the harmonic oscillator. The energy levels are not equidistant and also continuum states are accessible. Fig. 5.2 shows the TDSE calculations for three laser pulses ( $t_0 = 240$  a.u.,  $\Delta t = 50$ ,  $E_0 = 0.01$  a.u.) with different frequencies  $\omega$ . The system is prepared in the physical ground state which means the first odd wave function (cf. Chapter 4.3)

<sup>1</sup>The matrix elements for the dipole operator  $\hat{x}$  in the oscillator basis  $|m\rangle$  can be calculated by:

$$\langle n|\hat{x}|m\rangle = 1/\sqrt{2}\langle n|(\hat{a}^\dagger + \hat{a})|m\rangle = 1/\sqrt{2}(\sqrt{m+1}\langle n|m+1\rangle + \sqrt{m}\langle n|m-1\rangle) = 1/\sqrt{2}(\sqrt{m+1}\delta_{n,m+1} + \sqrt{m}\delta_{n,m-1})$$

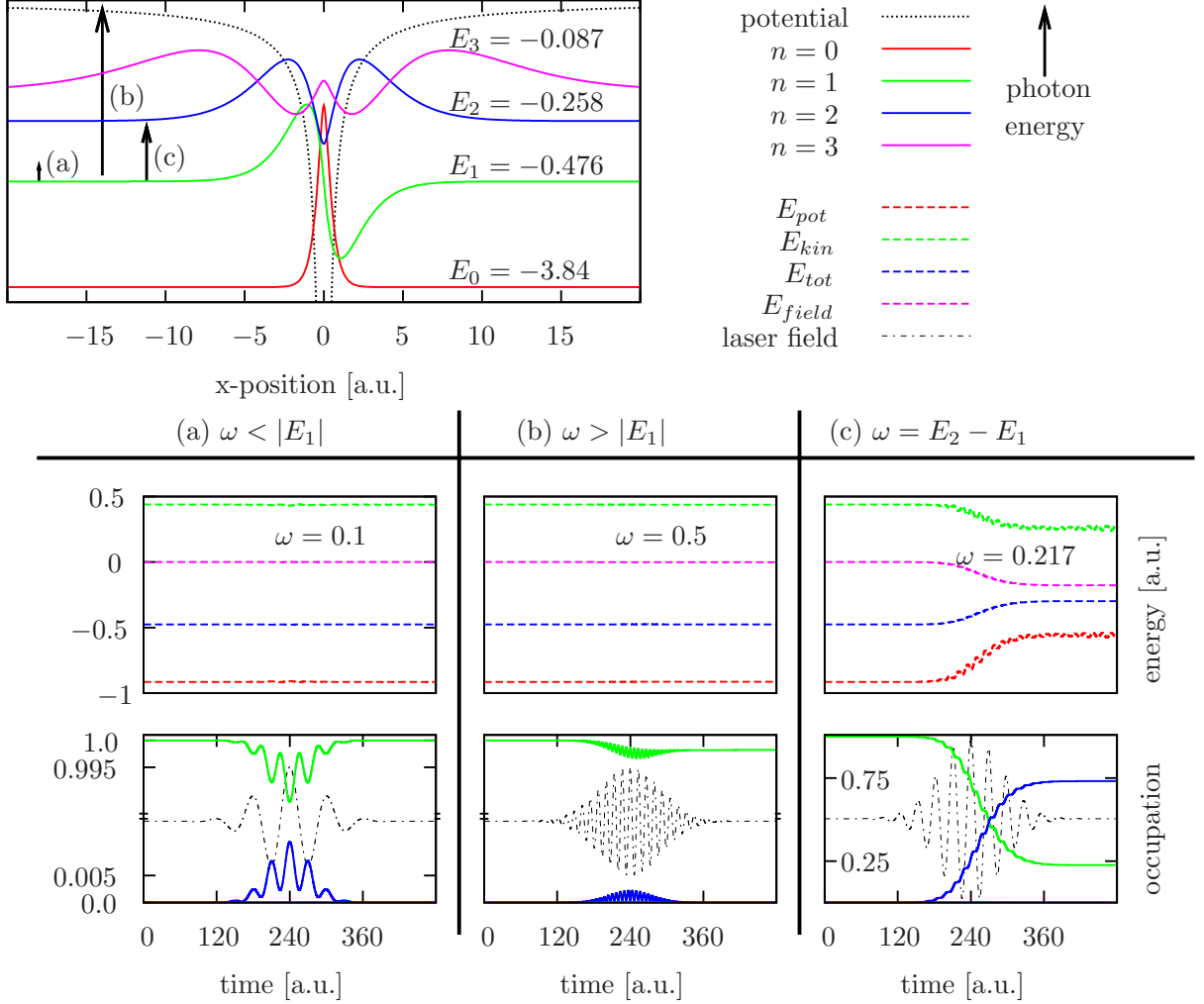


**Figure 5.2:** Laser excitation of bound states in a one-dimensional soft-core Coulomb potential,  $\kappa = 0.1$ . The uppermost figure displays the system and the selected excitations. For all pulses the system is initially prepared in the physical ground state (first odd wave function,  $n = 1$ ). Three different pulses are used: (a) the photon energy is smaller than the ionization potential but does not fulfill any Bohr condition. (b) the photon energy is larger than the binding energy, hence the electron can be lifted into the continuum and (c) the photon energy fulfills the Bohr condition  $E_2 - E_1 = \omega$ , thus the system can be resonantly excited to the next higher level. The lower figures show the time-dependent energies and occupation numbers. Note that the scale of the occupation numbers is changed from (b) to (c).

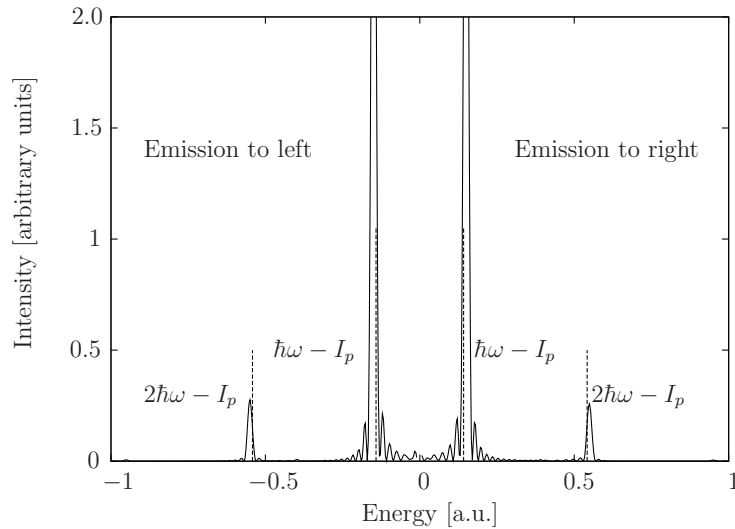


**Figure 5.3:** Comparison between Fermi's golden rule and the TDSE solution. The second state of a 1D Coulomb potential with the ionization potential  $I_p = 0.258$  a.u. is excited with a monochromatic laser pulse,  $\omega = 0.4$  a.u. The electron energy spectrum is calculated after 16 laser periods. Negative energies denote emission to the left, positive energies to the right of the Coulomb potential. The second peak appears due to higher-order effects. The dashed lines indicate the theoretical position of the photon peaks according to Fermi's golden rule. The width of the peaks obtained numerically stems from the finite excitation time and the resulting spectral broadening of the laser pulse.

with a binding energy of  $E_1 = -0.476$  a.u. The first pulse with  $\omega = 0.1$  a.u. can neither ionize the state nor excite the system to a higher state since no Bohr condition is fulfilled. The next energy level with  $E_2 = -0.258$  a.u. is separated by more than twice the photon energy. Similar to the harmonic oscillator only a small change in the occupation numbers during the excitation occurs and after the pulse the system is again in the initial state. For larger photon energies (middle figures,  $\omega = 0.5$  a.u.) the electron can access the continuum by absorption of one single photon. The initially filled energy level becomes depopulated and no other bound state is filled, thus this missing probability describes free electrons which have escaped the potential. As can be seen in the small change in the occupation number (and the only minor energy difference) the ionization yield is very small for the chosen intensities and pulse durations.

The strongest effect is obtained by irradiation with a frequency which fulfills the Bohr condition  $\Delta E = \omega$ . The right figures show such an arrangement ( $\omega = E_2 - E_1 = 0.217$  a.u. ). The initial state is drastically depopulated while the next level is filled. Since no ionization is possible and no other resonant state is accessible from this level the occupation is increased monotonously and no further excitation occurs. After the pulse the laser has increased the total energy of the system.

### Comparison with Fermi's golden rule

For further investigations of the populated continuum states we analyse the energies of directly ionized electrons ( $\omega > I_p$ ). A reasonable approximation to describe effects in these weakly excited systems is given by time-dependent perturbation theory. For monochromatic excitation with infinite duration, this formalism leads in first order to Fermi's golden rule, cf. Chapter 2.3.1, Eq. (2.28) and Eq. (2.29). Only final states with energies  $E = \hbar\omega - I_p$  can be accessed. Thus the electron spectrum shows discrete peaks. For higher-order processes, multiple final states with  $E_n = n \cdot \omega - I_p$  can be expected.

Fig. 5.3 shows the electron spectrum for a direct excitation of a state with the ionisation

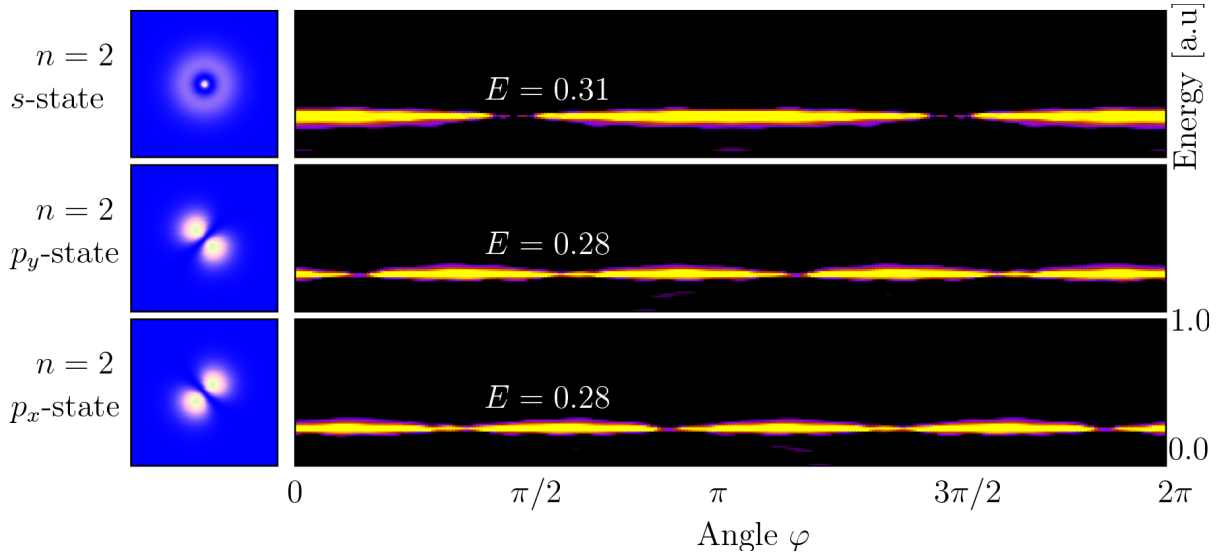


**Figure 5.4:** Angle-resolved ionization spectra of a single 2D model H-atom (2D-Coulomb system). The left figures show the initially prepared state ( $s$ - and  $p_x$ -,  $p_y$ -like states with  $E_p = -0.221$  a.u. and  $E_s = -0.194$  a.u., cf. Fig. 4.10). The right figures show the corresponding electron energy distributions obtained from a TDSE solution. The emitted electron is detected at a distance of  $r = 50$  a.u. The used excitation with  $\omega = 0.5$  a.u. and  $E_0 = 0.002$  a.u. can ionize the system with one single photon. The angle is measured with respect to the polarization axis of the laser field,  $\varphi = 0, \pi$  (cf. Chapter 3, Fig. 3.5).

potential of  $I_p = 0.258$  a.u. The photon energy is chosen as  $\omega = 0.4$  a.u. which allows for a direct ionization by the absorption of one single photon. In fact, the calculated electron spectrum shows discrete peaks at the correct position, but due to the finite pulse duration (16 laser cycles) they show a broadening. Because of second-order effects (absorption of two photons) a second peak appears in the spectrum. Both peaks are accurately separated by the photon energy  $\omega$ . The spectrum is symmetric with respect to the center of the Coulomb potential, which shows that no explicit direction of emission is preferred since the exciting pulse is symmetric regarding the net acceleration of the electron to the left or right (long pulse duration and no additional phase shift).

### 5.1.3 Angle-resolved electron spectra

The simple model of a one-dimensional system can be improved enormously if it is extended to a two-dimensional model atom. In such systems additional quantities like the angular distribution occur. In the following we concentrate on the ionization of a 2D hydrogen-like atom (2D regularized Coulomb potential with  $\kappa = 0.1$ ). The eigenstates are discussed in Chapter 4.3.3, Fig. 4.10. The first three states besides the unphysical ground state are investigated. The results are shown in Fig. 5.4. The laser frequency was chosen to be  $\omega = 0.5$  a.u. thus the initially bound electron can be directly ionized like in the 1D case. A detector is placed at a distance of  $r = 50.0$  a.u. where the electrons are considered to be free and not driven back to the core. It was secured that the spectrum is independent of the distance  $r$  of the detector. After the detection the wave function is damped with an imaginary absorber potential in order to allow for a smaller size of the simulation box.

The first order photon peak appears for all three states at the expected energy  $E = \omega - I_p$ . A remarkable feature is the angle dependence for different types of states. The spherically symmetric  $s$ -state ( $n = 2$ ) is ionized predominantly along the polarization axis of the laser field ( $\varphi = 0$

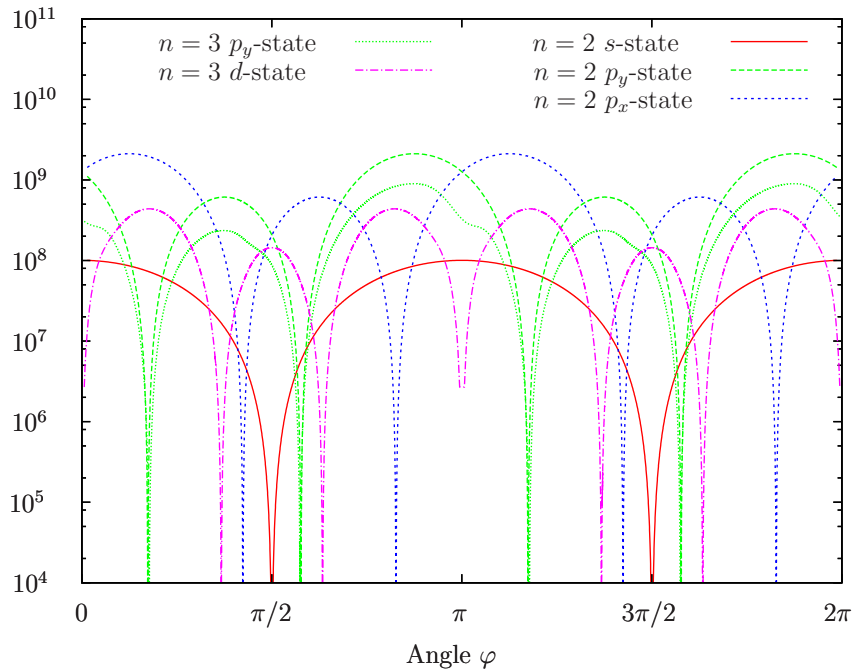


**Figure 5.5:** Absolute square of the dipole matrix elements  $\alpha_i(k, \varphi)$  for different states of the 2D model hydrogen atom, cf. Eq. (5.4). The possibility of dipole transitions from a bound state ( $s$ -,  $p$ - or  $d$ -state) to a free plane wave with fixed wave vector length  $k = 1.0$  a.u. and different angles  $\varphi$  is shown.

and  $\varphi = \pi$ ) whereas no perpendicular emission ( $\varphi = \pi/2$  and  $\varphi = 3\pi/2$ ) is observed. A totally different picture is obtained for the  $p_x$ - and  $p_y$ -states. Both spectra show four distinct minima but are rotated by  $\pi/4$  with respect to each other, as is the density of the initial states. As can easily be seen in Fig 5.4, neither the preferred direction of emission nor the drop in the intensity of the resolved photoelectrons correspond to the polarization axis of the laser field. The position of the minima strongly depends on the orientation of the initial state with respect to the field polarization axis but the *number* of drops (2 in the case of a  $s$ -state and 4 in the case of both  $p$ -states) seems to be a universal quantity depending on the angular momentum of the initial state.

The calculation of the dipole matrix

$$\alpha_{i,\mathbf{k}} = \langle \phi_i | \hat{x} | \phi_{\mathbf{k}} \rangle \quad (5.3)$$

helps get insight into the physical mechanism behind those forbidden regions.  $\phi_i$  denotes the initial bound state and  $\phi_{\mathbf{k}}$  a plane wave,  $\exp(i\mathbf{k} \cdot \mathbf{r})$ . The angle  $\varphi = \tan^{-1}(k_x/k_y)$  (analogously the other branches of the arcus tangens function), which corresponds to the direction of the plane wave, and the length  $k$  of the wave vector are the free parameters. We will use cartesian coordinates to evaluate Eq. (5.3) because the initial states  $\phi_i$  are constructed via the ITP-algorithm on a cartesian grid. An integration in polar coordinates would be easier but requires a transformation of the  $\phi_i$  computed numerically.

In the chosen coordinate representation, the dipole matrix can be written as

$$\alpha_i(k, \varphi) = \int_{-\infty}^{\infty} \int_{-\infty}^{\infty} dx dy \phi_i^*(x, y) x \exp[ik(x \cos \varphi + y \sin \varphi)] . \quad (5.4)$$

The integration is performed numerically for every angle  $\varphi$ . The length of the wave vector,  $k = \sqrt{k_x^2 + k_y^2}$ , is fixed and chosen according to Fermi's golden rule to  $k = \sqrt{2\omega} = 1.0$  a.u. The

results are displayed in Fig. 5.5.

At first sight, one recognizes the strong variation of the angle dependence when different atomic states  $\phi_i$  are chosen. The dipole matrix elements of the  $s$ -state, indicated by the red solid line, show two minima at the angles  $\varphi = \pi/2$  and  $\varphi = 3\pi/2$  which is exactly perpendicular to the field-polarization axis. States with larger angular momentum, i.e., the  $p$ -states and the displayed  $d$ -state, behave differently: As in the numerically obtained solutions of the TDSE, the  $p_x$ - (blue dashed line) and the  $p_y$ - (green dashed line) states possess four minima which can be identified up to more than six orders of magnitude. The angles of those drops do neither coincide with the field polarization axis nor are they perpendicular to it. They are observed at exactly the same angles as in the angle-resolved photoelectron spectra of the direct ionization which were obtained by means of numerical solutions of the TDSE, cf. Fig. 5.4.

The specific positions of the minima depend on the alignment of the states with respect to the field polarization axis, which can be seen from the equidistant shift of the drops for the differently oriented  $p_x$ - and  $p_y$ -states. Additionally, these positions are independent of the quantum number  $n$ . This can be seen in Fig. 5.5, where the  $3p_y$ -state and the  $2p_y$ -state exhibit the same angle dependence of the dipole matrix elements (see Chapter 4.3.3, Fig. 4.10 for the corresponding densities of  $\phi_i$ ). Therefore, the observed features in the dipole matrix elements can be interpreted as a consequence of the angular momentum  $l$  of the state  $\phi_i$ . The calculation of the dipole matrix for a  $d$ -state (larger angular momentum) supports this interpretation. Here, six distinct minima can be identified (magenta line in Fig. 5.5).

As a closing remark, the perfect agreement between both methods considered, the full TDSE approach and the calculation of the angle-dependent dipole matrix elements, is pointed out. One may conclude that the observed angle-dependent features in the two-dimensional photoelectron spectra shown in Fig. 5.4 can be explained in terms of dipole-forbidden transitions.

### Angle dependence of allowed dipole transitions for the hydrogen atom

Now, it seems worthwhile to investigate the ionization of the hydrogen atom based on the approach developed for the two-dimensional case. It appears that the technique for the calculation of the angle-dependent dipole matrix elements can be easily extended to the 3D case. The generalization of Eq. (5.3) is straightforward and the resulting dipole matrix elements are now dependent on the two spherical angles  $\varphi$  and  $\theta$ :

$$\alpha_i(k, \varphi, \theta) = \int_0^\infty dr' \int_0^\pi d\theta' \int_0^{2\pi} d\varphi' r'^2 \sin \theta' \phi_i^*(r', \theta', \varphi') r' \sin \theta' \cos \varphi' \Pi(k, \theta, \varphi, r', \theta', \varphi') . \quad (5.5)$$

$\Pi(k, \theta, \varphi, r', \theta', \varphi')$  represents the plane wave in spherical coordinate representation and the  $\phi_i(r, \theta, \varphi)$  are the wave functions of the hydrogen atom which are well-known from quantum mechanics.

They can be split into an angular part  $Y_{l,m}(\theta, \varphi)$  and a radial part  $R_{n,l}(r)$ :

$$\psi_{n,l,m} = R_{n,l}(r) \cdot Y_{l,m}(\theta, \varphi) . \quad (5.6)$$

As we learned in the two-dimensional case from the similar behavior of the  $2p_y$ - and  $3p_y$ -state, only the angle-dependent part, the  $Y_{l,m}$ , should play a role in the calculation of angle-dependent

## 5 Excitation and ionization in laser fields

dipole transitions. The first three corresponding functions read

$$Y_{0,0}(\theta, \varphi) = \frac{1}{\sqrt{4\pi}}, \quad (5.7)$$

$$Y_{1,0}(\theta, \varphi) = \frac{3}{\sqrt{4\pi}} \cos \theta, \quad (5.8)$$

$$Y_{1,\pm 1}(\theta, \varphi) = \mp \frac{3}{8\pi} \sin \theta \exp \pm i\varphi. \quad (5.9)$$

As can be seen in the case of  $Y_{1,\pm 1}$ , the resulting density is the same for  $m = 1$  and  $m = -1$ . Thus the different orientation of the wave function with respect to a laser polarization, as studied in the two-dimensional case of the  $p_x$ - and  $p_y$ -states, cannot be present for all three functions. However, this may be of special interest in the observation of the angle-dependent drops in the dipole matrix elements.

Now the orbitals of the hydrogen atom and hydrogen-like atoms known from chemistry come into play. Orbitals with different angular orientation for a fixed quantum numbers  $l$ , are given by superpositions of the spherical harmonics with different  $m$  [Eqs. (5.8) and (5.9)], such that the resulting orbital wave function is real. For a nomenclature see for instance [47]. There are three real and orthogonal  $p$ -orbitals, which are differently oriented in space and exhibit similar features as the  $p_x$ - and  $p_y$ -states obtained for the two-dimensional case. They are constructed from  $Y_{1,m}$  and are given by

$$\psi_{n,p_z}(r, \theta, \varphi) = R_{n,1}(r)Y_{1,0}(\theta, \varphi) = \sqrt{\frac{3}{4\pi}}R_{n,1}(r) \cdot \cos \theta, \quad (5.10)$$

$$\psi_{n,p_x}(r, \theta, \varphi) = \frac{1}{\sqrt{2}}R_{n,1}(r)(-Y_{1,1}(\theta, \varphi) + Y_{1,-1}(\theta, \varphi)) = \sqrt{\frac{3}{4\pi}}R_{n,1}(r) \cdot \sin \theta \cos \varphi, \quad (5.11)$$

$$\psi_{n,p_y}(r, \theta, \varphi) = \frac{1}{i\sqrt{2}}R_{n,1}(r)(-Y_{1,1}(\theta, \varphi) - Y_{1,-1}(\theta, \varphi)) = \sqrt{\frac{3}{4\pi}}R_{n,1} \cdot \sin \theta \sin \varphi. \quad (5.12)$$

Analogously, five independent  $d$ -orbitals can be constructed from  $Y_{2,m}$ :

$$\psi_{n,d_{z^2}} = R_{n,2}(r)Y_{2,0}(\theta, \varphi) = \sqrt{\frac{5}{16\pi}}R_{n,2}(r)(3 \cos^2 \theta - 1), \quad (5.13)$$

$$\psi_{n,d_{xz}} = \frac{1}{\sqrt{2}}R_{n,2}(r)(-Y_{2,1}(\theta, \varphi) + Y_{2,-1}(\theta, \varphi)) = \sqrt{\frac{15}{4\pi}}R_{n,2}(r) \sin \theta \cos \theta \cos \varphi, \quad (5.14)$$

$$\psi_{n,d_{yz}} = \frac{1}{i\sqrt{2}}R_{n,2}(r)(-Y_{2,1}(\theta, \varphi) - Y_{2,-1}(\theta, \varphi)) = \sqrt{\frac{15}{4\pi}}R_{n,2}(r) \sin \theta \cos \theta \sin \varphi, \quad (5.15)$$

$$\psi_{n,d_{x^2-y^2}} = \frac{1}{\sqrt{2}}R_{n,2}(r)(Y_{2,2}(\theta, \varphi) + Y_{2,-2}(\theta, \varphi)) = \sqrt{\frac{15}{16\pi}}R_{n,2}(r) \sin^2 \theta \cos 2\varphi, \quad (5.16)$$

$$\psi_{n,d_{xy}} = \frac{1}{i\sqrt{2}}R_{n,2}(r)(Y_{2,2}(\theta, \varphi) - Y_{2,-2}(\theta, \varphi)) = \sqrt{\frac{15}{16\pi}}R_{n,2}(r) \sin^2 \theta \sin 2\varphi. \quad (5.17)$$

The radial part  $R_{n,l}$  of the wave function remains the same as for the usual representation of the eigenstates of the hydrogen atom. The angle dependence of the orbitals [Eqs. (5.10) - (5.17)] is displayed in Fig. 5.6. Each orbital shows a different spatial orientation, as observed in the two-dimensional calculations via the ITP (cf. Chapter 4.3.3, Fig. 4.10). We will consider these orbitals to evaluate the angle-dependent dipole matrix elements, Eq. (5.5), since their densities are more alike in their shape as the 2D densities obtained numerically and treated previously in

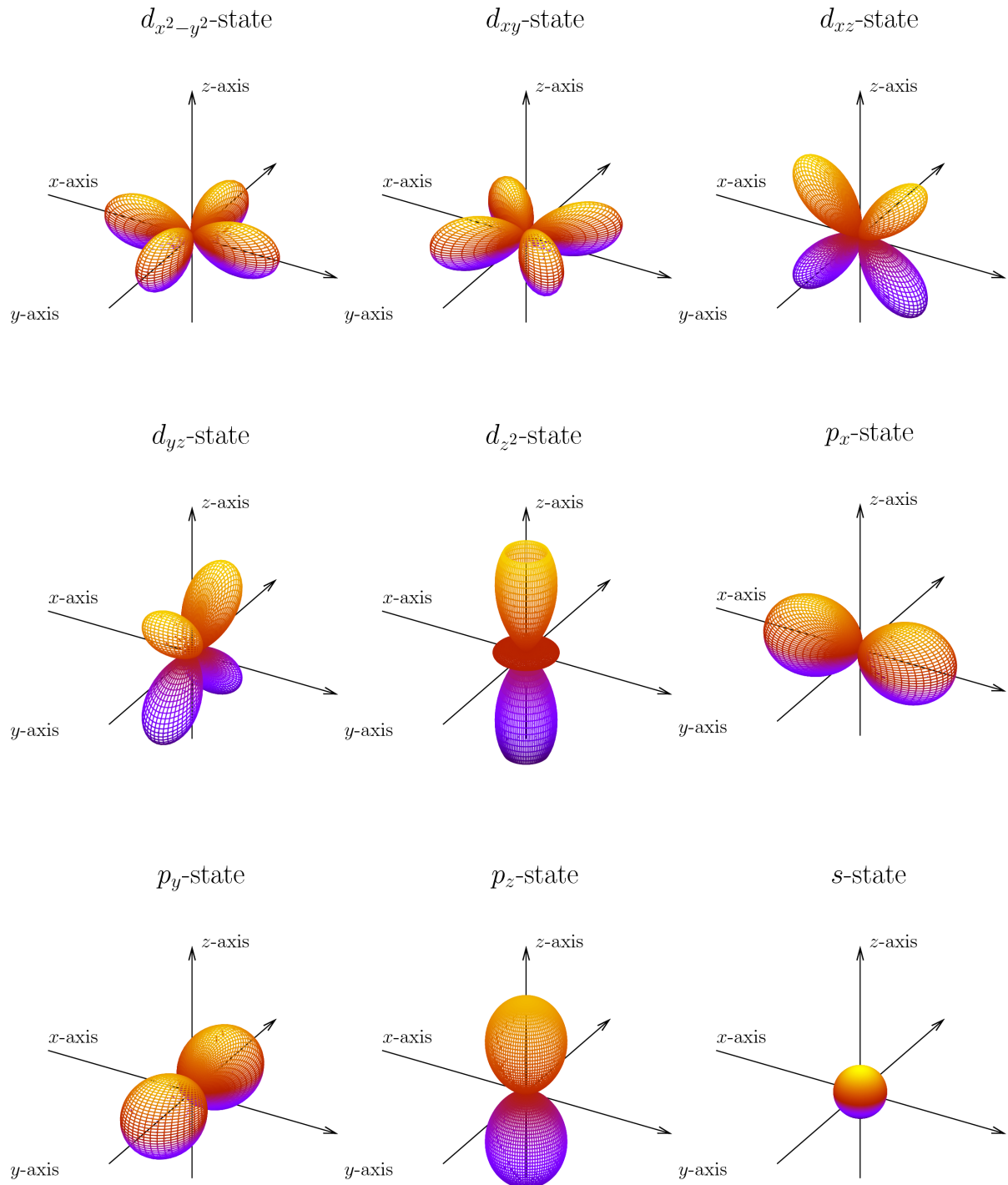


**Figure 5.6:** Angle dependence of the orbitals of the hydrogen atom for  $n < 3$  according to Eqs. (5.10) - (5.17). The orbitals are constructed from  $Y_{l,m}$  such that the resulting wave function is real. To obtain the final wave function, these orbitals have to be multiplied by the radial part  $R_{n,l}(r)$ .

## 5 Excitation and ionization in laser fields

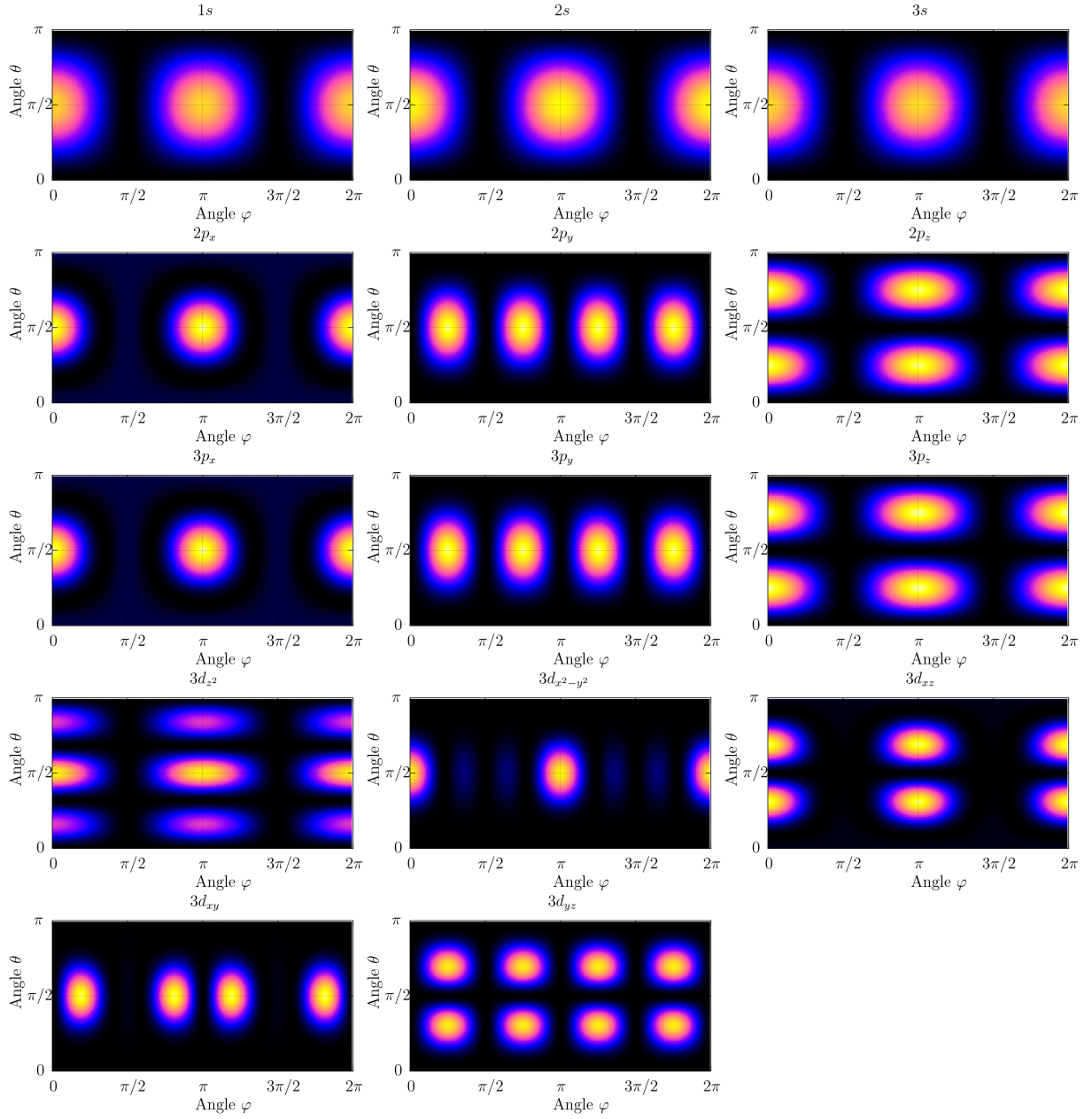


**Figure 5.7:** Angle dependence of the absolute square of the dipole matrix elements  $\alpha_i(k = 1, \theta, \varphi)$ , Eq. (5.5), for different states  $\phi_i$  of the hydrogen atom, cf. Fig. 5.6. The color, in a linear presentation, indicates the probability for a dipole transition from high (bright color) to low (dark regions).

this chapter. Additionally, the explicit choice of the basis should not affect the physical solution of the problem investigated.

The integration of Eq. (5.5) is performed numerically in spherical coordinates for different angles  $\varphi$  and  $\theta$  of the final plane wave  $\Pi(k, \theta, \varphi, r', \theta', \varphi')$ . The length of the wave vector was again fixed to  $k = 1.0$  a.u. The results for the discussed initial bound states  $\phi_i$  are presented in Fig. 5.7. Shown are the dipole-allowed transitions from the state  $\phi_i$  to a plane wave in dependence on the angles  $\varphi$  and  $\theta$  with respect to the dipole polarization axis (which corresponds to the angles  $\varphi = 0, \pi$  and  $\theta = \pi/2$ ). At first glance one observes, in analogy to the two-dimensional case, no dependence on the quantum number  $n$ . The angle-dependent dipole matrix elements show a similar behavior for the  $1s$ -,  $2s$ - and  $3s$ -states. The same statement holds as well for the  $2p_x$ - and  $3p_x$ -state and accordingly the  $p_y$ - and  $p_z$ -states.

As in the two-dimensional case, the quantum number  $l$  of a state is an important quantity to describe the resolved angle dependence. Additionally, the different adjustments of the orbitals with respect to the polarization axis, corresponding to different quantum numbers  $m$  as given by Eqs. (5.10) - (5.17), come into play. As observed previously, the higher  $l$  the more complex features appear, i.e., more drops in the transition probability to a plane wave at certain angles. Furthermore, the orientation of the orbitals results in a different structure. The  $2p$ -orbitals (second row in Fig. 5.7) may be mentioned as an example. Here, the different alignment results in a totally different angle dependence of the dipole matrix elements and the orientation of the initial state  $\phi_i$  is also found in the angle dependence of the allowed dipole transitions. In addition the angle-dependent shape of the bound state  $\phi_i$  plays an important role in the formation of the observed structures for the  $d$ -states. As an example, we mention the  $3d_{z^2}$ -orbital where the coincidence of the shape of the atomic wave function and the angle dependence of the dipole matrix elements is apparent<sup>2</sup>.

### Comparison with literature results

The qualitative theoretical explanation found in [48] agrees with the results obtained numerically and presented above. The phenomenon can be interpreted in terms of the selection rules for dipole-allowed transitions holding for the hydrogen atom. The important condition for our case is given by  $\Delta l = \pm 1$ . The final state in Eq. (5.5) described by an angle-dependent plane wave, can equivalently be described by an outgoing spherical wave. These waves carry, in analogy to the atomic wave functions, an angular momentum and have as well  $s$ -,  $p$ - and  $d$ -character.

By applying the selection rules one easily obtains that for an initially prepared  $s$ -wave function ( $l = 0$ ) the final electron wave must carry the angular momentum  $l = 1$  since this alone is a dipole-allowed transition. The final wave possesses a shape like the  $p_x$ -state because the characteristic axis is the polarization axis of the field in our case the  $x$ -axis. By comparing the results of the angle-dependent dipole matrix for a  $s$ -state, cf. Fig. 5.7 upper row, with the atomic wave function of a  $p_x$ -state, Fig. 5.6, one immediately recognizes the relation. The results obtained are sectional drawings of the final, spherical electron wave with  $p_x$ -character.

An analogous interpretation can be given for the states with higher angular momentum  $l$ . As an example, let us mention the angle-dependent dipole transitions for the  $2p_y$ -state. The accessible final electron wave has to be of  $s$ -character for the case  $\Delta l = -1$  or of  $d$ -character for the case  $\Delta l = +1$ . By again comparing the observed transition angles with an atomic  $d$ -state, Fig. 5.6, one finds that the angle distribution is a sectional drawing of such a spherical wave, but now with  $d_{xy}$ -character.

For the states with even higher angular momentum, in our case the  $d$ -states, the interpretation becomes more involved. Now, spherical waves with  $f$ -character and  $p$ -character (and of

<sup>2</sup>the famous ‘‘Doppelschnuller’’ structure, cf. Fig. 5.6  $3d_{z^2}$

## 5 Excitation and ionization in laser fields

course superpositions) can be occupied. This explains the rather complicated structure of the angle-dependent dipole matrix elements shown in Fig. 5.7, last two rows.

The rigorous analytical treatment, briefly mentioned in [48] and the references therein, is rather complex. According to [48] the angle dependence of the ionization spectrum created by a linearly polarized dipole field is given for any state by the simple formula

$$I(\theta) = \frac{\sigma}{4\pi} \left[ 1 + \frac{\beta}{2} (3 \cos^2 \theta - 1) \right]. \quad (5.18)$$

The angle  $\theta$  is measured against the polarization plane of the light field,  $\sigma$  is the total ionization cross section and  $\beta$  the *anisotropy* parameter.  $\beta$  is the single parameter used to describe the whole angle dependence of the spectrum. Its estimation involves the phase differences between the different partial waves and the cross sections for the production of the  $l-1$  and  $l+1$  partial waves. It has no additional angle dependence. By analyzing the results presented in Fig. 5.7 for the  $s$ -state, one immediately finds the  $\cos^2 \theta$  behavior predicted by Eq. (5.18). However, states which show a different angular behavior in their allowed transitions, again we exemplarily mention the  $3d_{z^2}$ -state, cannot be described accurately by this formula.

Now, the question arises how the results obtained above can be interpreted, especially concerning the orientation of the orbitals with respect to the laser polarization and a possible experimental realization. The investigation of angle-dependent features in the dipole matrix arose from the observation of intensity minima in the photoelectron spectra depending on the initial atomic state within a two-dimensional model. This could accurately be explained by dipole-allowed transitions. Therefore, in the case where both considered methods agree, the preparation of an atom in a corresponding orbital or an atom with an equivalent highest occupied orbital should also verify the results within an experimental setup — assuming that these experiments are feasible. Although, the case for the hydrogen atom may be more involved. Additional numerical simulations for angle-resolved photoelectron spectra seem worthwhile in order to verify the results obtained from the angle-resolved dipole matrix elements.

## 5.2 Above threshold ionization (ATI)

If the intensity of the laser field is increased to about  $10^{14}$  W/cm<sup>2</sup> and more, not only linear effects describable by Fermi's golden rule with one photon can appear. Non-linear effects like multi-photon (MP) processes described in Chapter 2.1.3 become relevant. In the following we will concentrate on above threshold ionization (ATI) which is an important MP process. During all calculations the photon energy  $\omega$  is smaller than the binding energy and only non-linear ionization is observed in the electron spectra.

### 5.2.1 TDSE solution for a 1D model atom

The first simple model again uses the regularized one-dimensional Coulomb potential with  $\kappa = 0.1$ . The system is prepared in one of the first three eigenstates which were obtained by the imaginary time propagation algorithm. The exciting laser pulse has a photon energy of  $\omega = 0.2$  a.u. which is not sufficient to ionize one of those states directly. But with an electric field amplitude of  $E_0 = 0.2$  a.u. the intensity of  $7.4 \cdot 10^{15}$  W/cm<sup>2</sup> enables multi-photon ionization. Fig. 5.8 shows the calculated electron spectra after propagating the TDSE for 16 laser cycles. The spectra consist of a distribution of equidistant peaks forming the above threshold ionization plateau (cf. Chapter 2.1.4). Each single event corresponds to the absorption of a single photon.

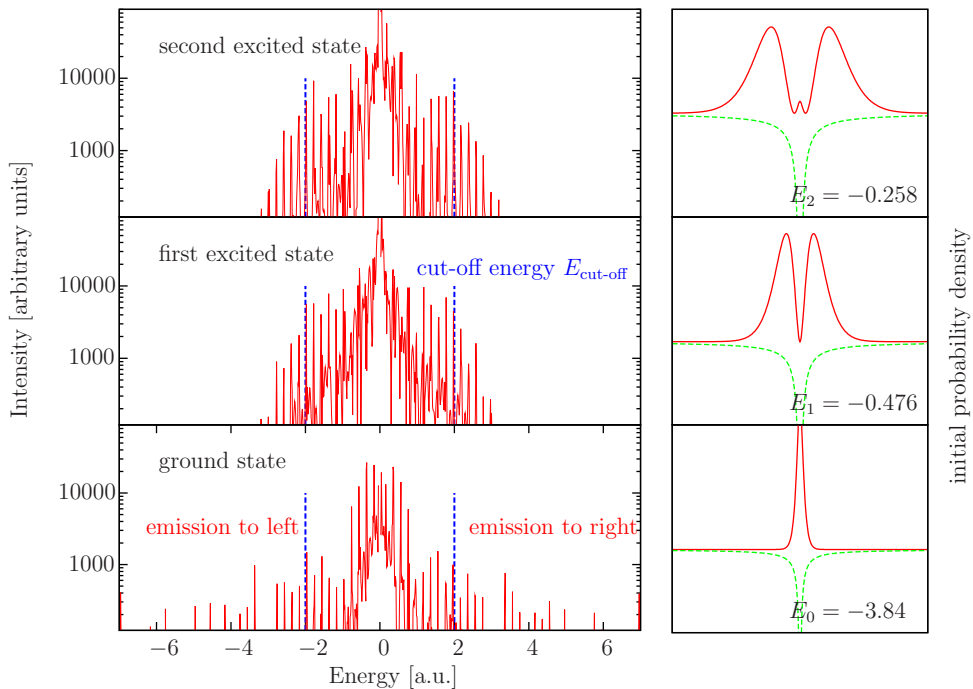


**Figure 5.8:** ATI spectra of a one-dimensional model H-atom (soft-core Coulomb,  $\kappa = 0.1$ ). The initially prepared states (constructed via ITP-method) before the laser excitation are given in the right picture, the dashed green line indicates the binding potential. The photon energy  $\omega = 0.2$  a.u. is smaller than the ionization potential for each state, the electric field  $E_0 = 0.2$  a.u. corresponds to an intensity of  $7 \cdot 10^{15}$  W/cm<sup>2</sup>. Therefore non-linear multi-photon ionization is possible. The left figures show the TDSE photoelectron spectrum after 16 laser cycles. Negative (positive) energies indicate emission to the left (right). The blue dashed lines indicate the cut-off energies according to  $E_{\text{cut-off}} = 8 \cdot U_p$ .

The peaks are well resolved and accurately separated by the photon energy  $\omega$ . Depending on the binding energy the spectrum shows different orders. The lower the state the more photons have to be absorbed to free the electron from the potential. Additional photons which will form the ATI spectrum are only absorbed with a small probability (very high order effect). For example the (unphysical) ground state with  $I_p = 3.84$  a.u. needs 20 photons to lift the electron into a continuum state. As can be seen in the spectrum (lowest pictures in Fig. 5.8), the ATI breaks down and only a few peaks in the intensity appear. For higher states with lower binding energy only a few quanta are needed for the ionization and the additional photons will form the ATI spectrum up to 18 photon orders (both upper figures).

An estimation of the cut-off is given in terms of the empirical formula  $E_{\text{cut-off}} = 8 \cdot U_p$  where  $U_p$  is the ponderomotive energy determined by Eq. (2.4). For the parameters used herein this cut-off evaluates to  $E_{\text{cut-off}} = 2.0$  a.u. (blue dashed lines in Fig. 5.8) which can be verified in the calculations. Also the main structures of the experimentally observed spectrum shown in Fig. 2.3 (b) can be reproduced.

### 5.2.2 Comparison with the strong field approximation (SFA)

A powerful theoretical tool for investigations of non-linear processes is the SFA (cf. Chapter 2.3.2). The transition probability from the first odd wave function  $\phi_1$  to the final Volkov states  $\phi_f$

$$P_{1 \rightarrow f} = \left| -i \int_{-\infty}^{\infty} dt \langle \phi_f | V(t) | \phi_1 \rangle \right|^2 \quad (5.19)$$

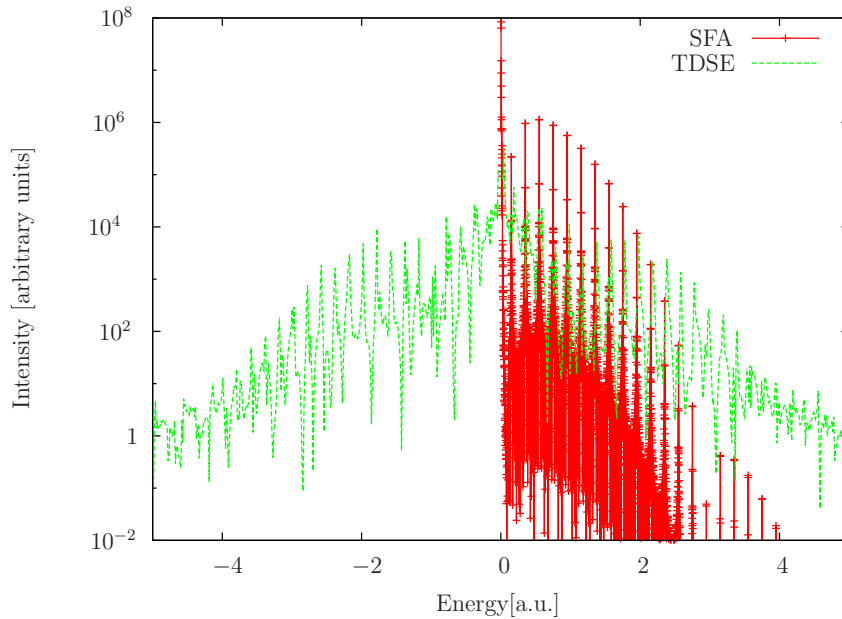


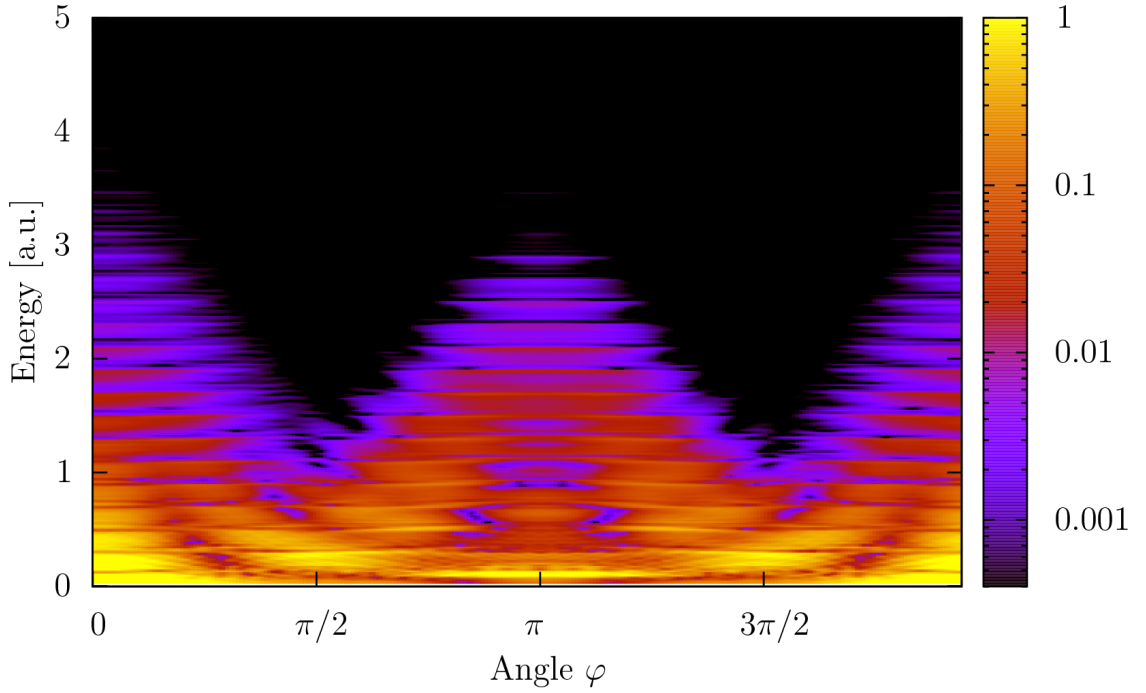
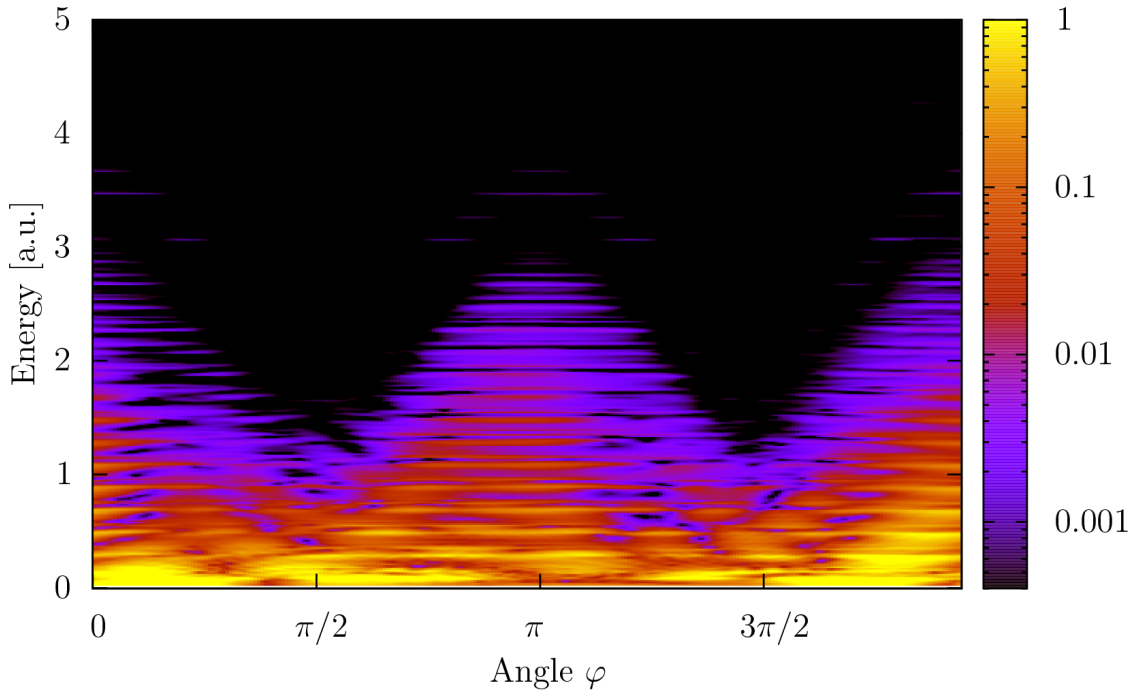
**Figure 5.9:** ATI spectrum of the first odd state in the 1D Coulomb potential ( $I_p = 0.5$  a.u.). The photon energy is adjusted to  $\omega = 0.2$  a.u. (only non-linear effects can appear). Shown is a comparison between the SFA and the full TDSE solution. The laser pulse with  $E = 0.2$  a.u. is instantaneously switched on at  $t = 0$ . The calculations were performed over 16 laser cycles.

is calculated numerically. Within the SFA the pure Coulomb potential ( $\kappa = 0$ ) is used because its eigenfunctions can be given analytically. Then the spatial integration of the scalar product in Eq. (5.19) can be evaluated (see Appendix D for a detailed description) which decreases the computational effort drastically.

Fig. 5.9 shows the ionization of the first odd wave function in the 1D Coulomb potential. For the benchmarking TDSE solution the regularized Coulomb potential is used. But according to the results in Chapter 4.3 this regularization has only little effect on the odd states. All other parameters are the same for both calculations. The methods show perfect agreement concerning the position of the photon peaks, but due to Coulomb effects the spectra differ in the height of the peaks and the range of the ATI plateau. The SFA is not able to reproduce the correct cut-off energy and shows a decrease in the intensity at lower energies. A distorted final state as used in the Coulomb Volkov approximation (CVA), where the influence of the long-range effect of the Coulomb potential on the final state is included, would give better agreement [24]. Additionally the chosen pulse intensity of  $7 \cdot 10^{15}$  W/cm<sup>2</sup> is at the lower boundary of the validity of the SFA. Still, this example clearly shows the importance of this approximation of Keldysh.

### 5.2.3 Angle-resolved 2D ATI spectra

As in the case of weak excitation, the two-dimensional model gives access to the angular distribution of emitted electrons. Fig. 5.10 shows an angle- and energy-resolved ATI spectrum for two different states ( $s$  and  $p_x$ ) in the 2D regularized Coulomb potential ( $\kappa = 0.1$ ) [49]. The direction of the highest energy yield is along the field polarization axis for both states ( $\varphi = 0, \pi$ ). Hence for the multi-photon absorption, the dipole single-photon selection rules of the weak excitation (cf. Fig. 5.4) are broken up. Each photon line in the spectrum now possesses its own substructure forming a rather complex angle dependence. The photoelectron spectrum of the isotropic  $s$ -state, Fig. 5.10 (a), shows a perfect symmetry along the polarization axis  $\varphi = \pi$  of the laser field whereas the spectrum of the  $p_x$ -state, Fig. 5.10 (b), exhibits an asymmetry, especially in

(a) ATI of the  $s$ -state, density: cf. Fig. 5.4(b) ATI of the  $p_x$ -state, density: cf. Fig. 5.4

**Figure 5.10:** Angle- and energy-resolved ATI spectra for two states of the 2D soft-core Coulomb potential,  $\kappa = 0.1$ . The color key indicates the intensity (logarithmic plot). The angle  $\varphi$  is measured with respect to the field polarization axis  $x$  ( $\varphi = 0, \pi$ ). The upper figure shows the ionization of the isotropic  $s$ -state and the lower figure the spectrum of the  $p_x$ -state. Both calculations performed within the KH-frame are for a laser pulse ( $t = 16$  cycles) with  $\omega = 0.2$  a.u. and  $E_0 = 0.2$  a.u. corresponding to an intensity of  $7 \cdot 10^{15}$  W/cm<sup>2</sup>.

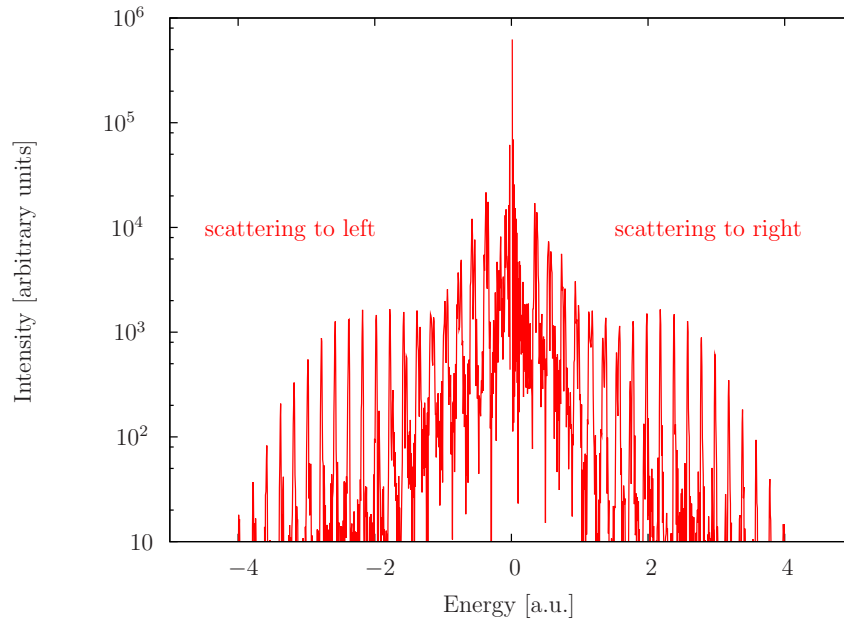


**Figure 5.11:** Electron spectrum of a scattering process with  $k_0 = 0$  electrons in the vicinity of an ion (regularized Coulomb potential with  $\kappa = 0.1$ ) in a strong laser field ( $\omega = 0.2$  a.u.,  $E_0 = 0.2$  a.u.,  $t = 16$  laser cycles).

the lower photon orders. But its dominant direction of multi-photon ionization is also along the polarization axis. The maximum cut-off energy along the field ( $\varphi = \pi$ ) is the same as in the 1D case.

### 5.3 Scattering with slow electrons

This part leads over to another central issue of this work, time-dependent Coulomb scattering in strong laser fields. The physical mechanisms behind the absorption of photons during scattering processes and ionization are basically the same. Hence in the following the connection point between both, at first sight different topics, will be worked out.

We consider the scattering of very slow electrons in the vicinity of an ion in a strong laser field. This can be achieved within the wave packet formalism introduced in Chapter 4.2 [10]. The Gaussian shaped wave packet of the form given by Eq. (4.4) with a wave vector  $k_0 = 0$  and a very large spatial spread  $\sigma = 1000.0$  a.u. represents those electrons. Applying a laser field allows them to gain energy via absorption of photons, similar to the ATI mechanism. Therefore the resulting energy distribution of scattered electrons is expected to show the features of an ATI spectrum, symmetric in both scattering directions.

Fig. 5.11 presents the energy distribution of such a scattering process in one dimension, obtained by solving the TDSE. The laser parameters are the same as in the ATI case ( $\omega = 0.2$  a.u.,  $E_0 = 0.2$  a.u.,  $t = 16$  laser cycles). The ATI features in the spectrum are clearly visible and the relation between scattering and ionization becomes apparent. Therefore scattering processes in strong laser fields obey the same absorption rules and mechanisms as multi-photon ionization processes. Since the electron is already free, the cut-off energy is higher than in the pure ATI case. Of course for situations with  $k_0 > 0$  the setup becomes highly asymmetric and the ATI spectrum distorts. These asymmetric situations are presented in detail in the next chapter.

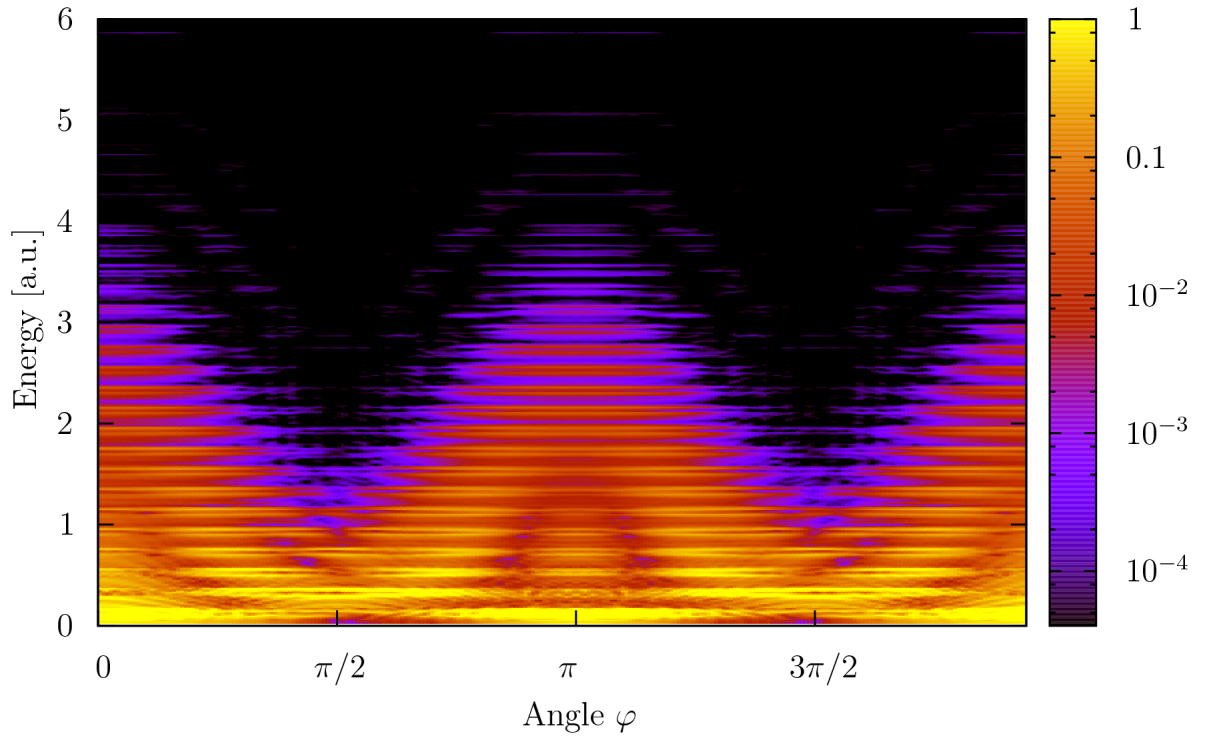


**Figure 5.12:** Angle-resolved spectrum of a scattering process with  $k_0 = 0$  electrons within a strong laser field ( $\omega = 0.2$  a.u.,  $E_0 = 0.2$  a.u.). The color indicates the intensity of the detected electrons (logarithmic plot) on a detector at the distance  $r = 75.0$  a.u.

Nearly the same arguments hold for the 2D case (Fig. 5.12). The simulation box sizes are somewhat smaller since the grid sizes are more limited in two dimensions. Hence the initial state has a width of  $\sigma = 50$  a.u. All other parameters are the same as in the 1D case. Here, it becomes clear that the scattering of slow electrons involves all lower states of the binding potential since the Gaussian shaped initial wave function can be expanded in terms of the eigenfunctions of the Coulomb potential. The spectrum is symmetric with respect to the polarization axis of the field. All subfeatures due to different alignment of the wave functions (like  $p_x$ - or  $p_y$ -orientation) are smeared out and superposed to a total spectrum which exhibits angular symmetry around  $\varphi = 0, \pi$ . The maximum energy gain is again slightly higher compared to the ATI since the electrons are already free. The cut-off energy in the polarization direction of the external field is the same as in the one-dimensional case ( $\approx 3.8$  a.u.). Thus, for the estimation of cut-off energies the 1D model seems to be a reasonable simplification.

## 5 *Excitation and ionization in laser fields*

## 6 Coulomb scattering

In the beginning of this chapter a simple one-dimensional model for electron scattering on single ions in laser fields is introduced. This model illustrates the arising effects based on numerical solutions of the time-dependent Schrödinger equation for wave packet scattering on a regularized Coulomb potential. It follows a classical approach to scattering processes within the static field limit (*instantaneous Coulomb collisions* [10]) which gives the opportunity to estimate maximum energies and helps construct improved and more efficient scattering setups. This will be the central issue of the following section: the investigation of resonance phenomena and the generation of high-energy electrons on a microscopic scale utilizing scattering processes on two and more ions in adequate distances.

In the second part we concentrate on Coulomb scattering in two-dimensional systems and the corresponding angle dependences of scattered electrons. After discussing classical Coulomb scattering without any laser field and its comparison to quantum mechanical wave-packet scattering, the case of different laser intensities is investigated. Special attention is paid to the collision of electrons with single ions in the presence of a strong field and the corresponding angle-resolved energy spectra within the framework of the TDSE. Various scattering geometries and detector resolutions are presented. Finally, we adapt the previously constructed 1D scattering setups to two dimensions. First, electron scattering on an ion pair is considered and finally this setup is enhanced by an additional confinement potential. Again, the angle- and energy-resolved electron spectra are discussed.

### 6.1 Coulomb scattering in a one-dimensional model

In the following, Coulomb scattering on a one-dimensional model ion in a strong laser field is discussed. Again, for numerical reasons, the regularized Coulomb potential, Eq. (4.8) with  $\kappa = 0.1$ , is used to represent the ion with atomic number  $Z = 1$ . The electron is modelled by a Gaussian-shaped wave packet [cf. Eq. (4.4)]. Fig. 6.1 shows the scattering setup for a single ion. Besides single-ion scattering also electron scattering on ion pairs as well as arrangements of three ions will be discussed. Fig. 6.1 holds schematically for all one-dimensional scattering geometries considered in this thesis. The initial wave packet is placed at the position  $-x_0$  left of the ion.  $x_0$  is chosen according to the initial momentum  $k_0$  of the wave packet such that the center of the wave packet is in a symmetric position  $x_0$  after time propagation:

$$x_0 = k_0 \cdot \frac{\tau}{2} \quad \text{with} \quad \tau = N_{\text{laser}} \cdot \frac{2\pi}{\omega} . \quad (6.1)$$

$N_{\text{Laser}}$  denotes the total number of laser cycles during the collision process (usually  $N_{\text{Laser}} \approx 16$  is chosen). For simplicity no laser pulse shaping is applied. All calculations presented in this chapter are performed within the Kramers-Henneberger frame of reference. Therefore the quiver motion of the electron is eliminated and the Coulomb potential moves back and forth. Thus the electron wave function behaves like a free particle until it reaches the ion and the obtained results are not sensitive to the chosen  $N_{\text{Laser}}$ .

An additional free parameter is the width  $\sigma$  of the wave packet. As is shown for the case of scattering on a potential well in Chapter 4.2, this is a critical parameter for sufficient resolution

## 6 Coulomb scattering

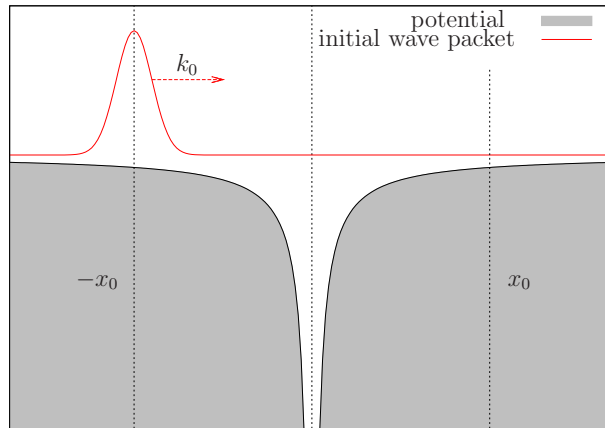


**Figure 6.1:** Wave packet scattering on a single ion (soft-core Coulomb potential).  $-x_0$  indicates the initial position of the center, determined by Eq. (6.1).  $+x_0$  represents the final position of the wave packet if its motion would not be perturbed (symmetric situation).  $k_0$  indicates the initial momentum of the electron.

in the energy domain. Furthermore, the width of the Gaussian wave packet increases while traveling over the potential-free region before the collision. Therefore it is chosen in relation to  $x_0$  and  $k_0$  such that the influence of any additional spreading is small and the energy resolution is high enough to accurately resolve the distinct photon orders:

$$\sigma = 0.4 \cdot x_0 . \quad (6.2)$$

This condition also assures that the initial wave function has only a small probability amplitude in the region of the scattering center.

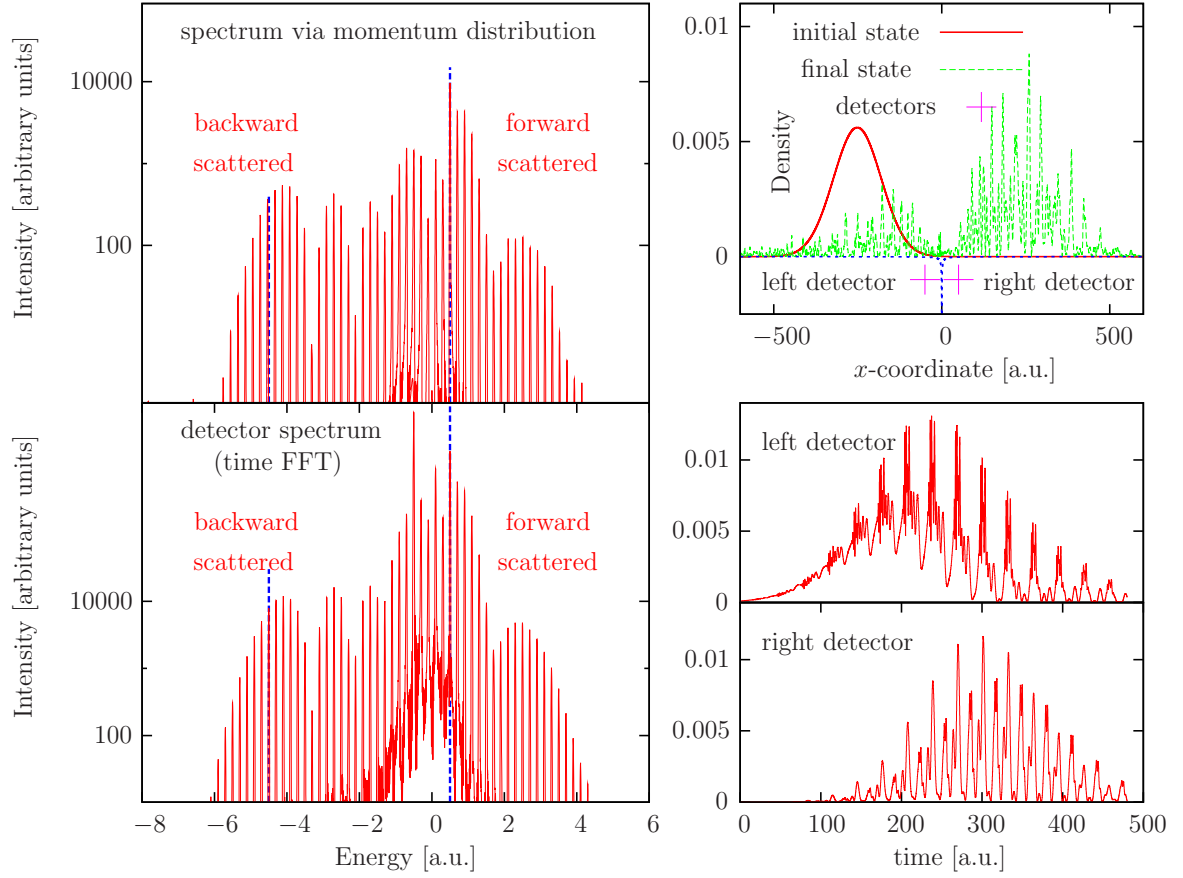
### 6.1.1 Single ion collisions

We are interested in the energy distribution of an electron after the collision with an ion in a laser field. The numerically obtained solution of the TDSE for wave packet scattering processes on a regularized Coulomb potential is shown in Fig. 6.2. The initially prepared wave packet at the position  $x = -x_0$  travels with a wave vector of  $k_0 = 1.0$  a.u. (a) [ $k_0 = 4.0$  a.u. (b)] towards the Coulomb potential at  $x = 0$ . The whole system is excited by a strong laser field with  $\omega = 0.2$  a.u. and  $E_0 = 0.2$  a.u. This corresponds to an intensity of  $7 \cdot 10^{15}$  W/cm<sup>2</sup>. The resulting energy spectrum of the scattered electron is obtained with both methods outlined in Chapter 3.4: firstly by using the momentum distribution in combination with the free particle dispersion relation and secondly by placing a detector at a distance  $r = 50.0$  a.u. The positions of the detectors are indicated in the right figures. For situation (a) also the time-dependent density on these selected grid points is displayed which provides the raw data for the energy spectrum shown in the left figures. First of all, both methods perfectly agree, cf. Fig. 6.2 (a), left graphs, in the energy cut-offs as well as in the relative height of the corresponding photon orders. Therefore all simulations presented later in this chapter use the approach with less computational effort according to the individual investigated problem. If no special remark is made this will be the detector technique.

The right graphs in Fig. 6.2 (a) and (b) display the initial Gaussian wave packet and the final state after colliding with the potential ( $t = 480$  a.u.). The main part of the density is located at the expected position  $x_0$  but is strongly deformed due to the collision process. The packet has separated into a reflected and a transmitted part. From the behavior of the reflection coefficient for the regularized Coulomb potential (Chapter 4.3.1, Fig. 4.7) one easily recognizes that the

### 6.1 Coulomb scattering in a one-dimensional model

(a) Electron scattering on a single ion with  $k_0 = 1$  a.u.



(b) Electron scattering on a single ion with  $k_0 = 4$  a.u.

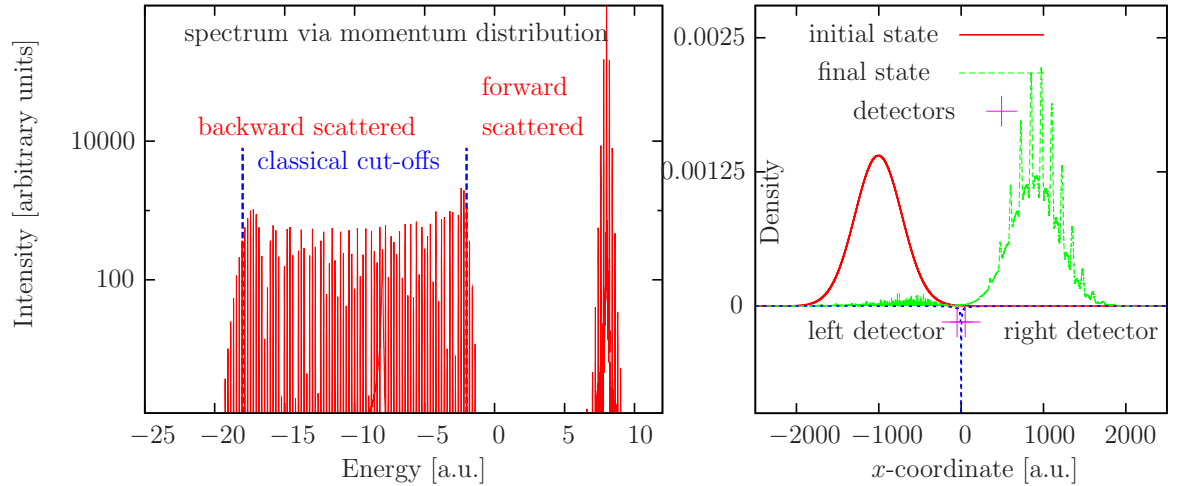


**Figure 6.2:** Wave packet scattering on a single ion located at a strong laser field with  $\omega = 0.2$  a.u. and  $E_0 = 0.2$  a.u. which corresponds to an intensity of  $7 \cdot 10^{15}$  W/cm<sup>2</sup>. (a) and (b) show the same process but with different initial momenta  $k_0$  of the wave packet. The upper right picture displays the initial (red) and the final density (green) after the collision. The detector positions at a distance of  $r = 50.0$  a.u. are marked by magenta crosses. The lower right graphs in (a) show the time series on the detector grid point and the left figures present the total energy spectrum after the collision process, calculated with both methods introduced in Chapter 3.4. The direction of the scattered electron is indicated by positive (right) and negative (left) energies. In (b) the application of only one technique is shown. The classical cut-off energies are estimated within the static field limit, see Chapter 6.1.2.

## 6 Coulomb scattering

$k_0/\text{a.u.}$	1.0	2.0	3.0	4.0	5.0
$k_{\text{max}}/\text{a.u.}$	-3.0	-4.0	-5.0	-6.0	-7.0
$k_{\text{min}}/\text{a.u.}$	1.0	0.0	-1.0	-2.0	-3.0
$E_{\text{max}}/\text{a.u.}$	-4.5	-8.0	-12.5	-18.0	-24.5
$E_{\text{min}}/\text{a.u.}$	0.5	0.0	-0.5	-2.0	-4.5

**Table 6.1:** Cut-off energies and maximum/minimum momenta for electrons in the case of electron scattering on a single ion in a laser field with  $\omega = 0.2$  a.u. and  $E_0 = 0.2$  a.u. calculated according to the classical theory within the static field limit, Eq. (6.4) and Eq. (6.5). The negative energies and momenta indicate backward scattering.

probability of reflection is reduced with increasing wave vector. Hence the wave packet with  $k_0 = 4$  a.u. shows a much smaller reflected fraction.

As discussed in Chapter 5.3 for scattering processes of  $k_0 = 0$  electrons a finite initial momentum  $k_0$  of the electron introduces an asymmetric situation. The main mechanism of energy absorption from the laser field is the same as in the ATI case (multi-photon absorption). Both spectra in Fig. 6.2 (a) and (b) show this asymmetry in forward (positive energies) and backward scattering (negative energies). The highest intensity peak in each spectrum comes from the unscattered initial wave packet and is located at an energy  $E = k_0^2/2$ . In the case of the electron spectrum resolved on the detector also the initial wave packet travelling over the left detector produces a very large peak at  $E = -k_0^2/2$ , cf. Fig. 6.2 (a) lower left. The interesting part of the spectrum is now formed by the backward scattered fraction of the wave packet, i.e., the electrons reflected by the potential. They form a large plateau in intensity up to a significant cut-off energy at  $E_{\text{max}} = -5.0$  a.u. for  $k_0 = 1.0$  a.u. and  $E_{\text{max}} = -18.0$  a.u. for  $k_0 = 4.0$  a.u. The energy absorption mechanism of single photons is obvious since the whole spectrum consists of isolated peaks separated by the photon energy  $\omega$ .

### 6.1.2 Instantaneous Coulomb collisions

A classical approach [10] is quite effective in approximately describing the shape and the cut-off energies of the resolved electron spectra. The collisions in the time-dependent laser field are treated within the static field limit where the electric field of the excitation is assumed to be constant during the scattering time. This approximation is valid if the collision time is much smaller than one period,  $T = 2\pi/\omega$ , of the laser field.

The momentum conservation law of an elastic scattering process reads:

$$k + p_E = -(k_0 + p_E) . \quad (6.3)$$

The momentum of the electron before the collision is given by  $k_0$  and  $k$  indicates its momentum after the collision.  $p_E = v_0 \cos \phi$  with  $\phi = \omega t_c$  is the quiver momentum at the collision time  $t_c$ .  $v_0 = E_0/\omega_0$  determines the amplitude of the quiver velocity, cf. Eq. (2.2). The quantity  $p_E$  can then be regarded as the additional momentum the electron obtains from the electric field of the laser. Its value exhibits a maximum if the field reaches the turning points where  $\cos \phi = \pm 1$  holds which corresponds to collision times  $t_c = n \cdot \pi/\omega$ ,  $n = 1, 2, \dots$ . Hence, the resulting maximum and minimum momenta after the collision are simply determined by

$$k_{\text{max}} = -k_0 - 2v_0 \quad \text{and} \quad k_{\text{min}} = -k_0 + 2v_0 . \quad (6.4)$$

The sign indicates the direction of the particle after the collision. The corresponding character-

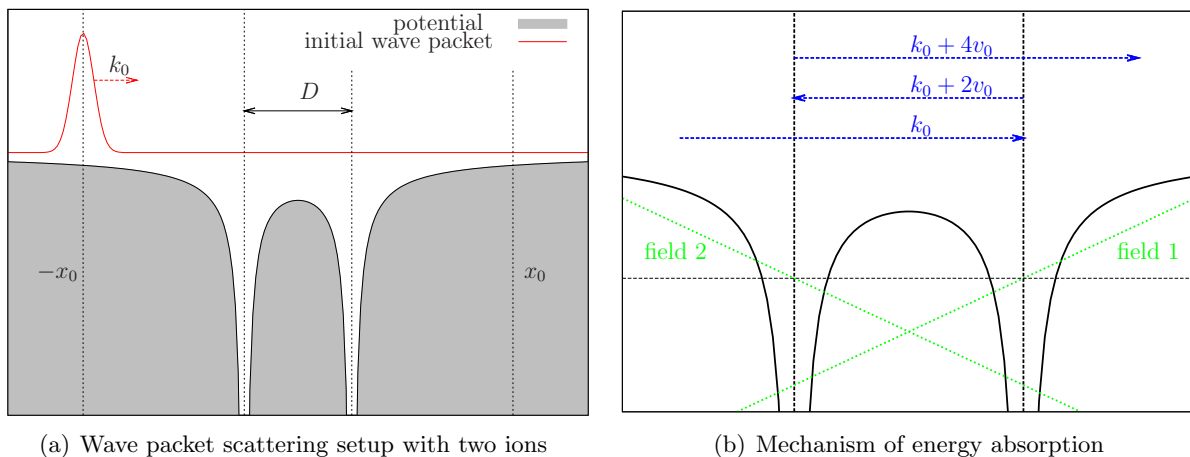


**Figure 6.3:** Scattering on an ion pair.  $k_0$  is again the initial momentum of the wave packet,  $v_0$  the ponderomotive velocity of the electron in the laser field. Fig. (b) shows the mechanism of resonant acceleration by two subsequent scattering processes. The lines field 1 and 2 indicate the instantaneous dipole potential at time of scattering. This corresponds to  $\phi = n \cdot \pi/\omega$ ,  $n = 1, 2, \dots$  in Eq. (6.3).

$k_0/\text{a.u.}$	1.0	2.0	3.0	4.0	5.0
$D/\text{a.u.}$	47.12	62.83	78.54	94.24	109.95
$E_{\text{max}}/\text{a.u.}$	12.5	18.0	24.5	32.0	40.5

**Table 6.2:** Resonance distances and cut-off energies for electron scattering on an arrangement of two ions in a laser field with  $\omega = 0.2$  a.u. and  $E_0 = 0.2$  a.u. within the classical approach according to Eq. (6.6) and Eq. (6.7).

istic cut-off energies can be written as

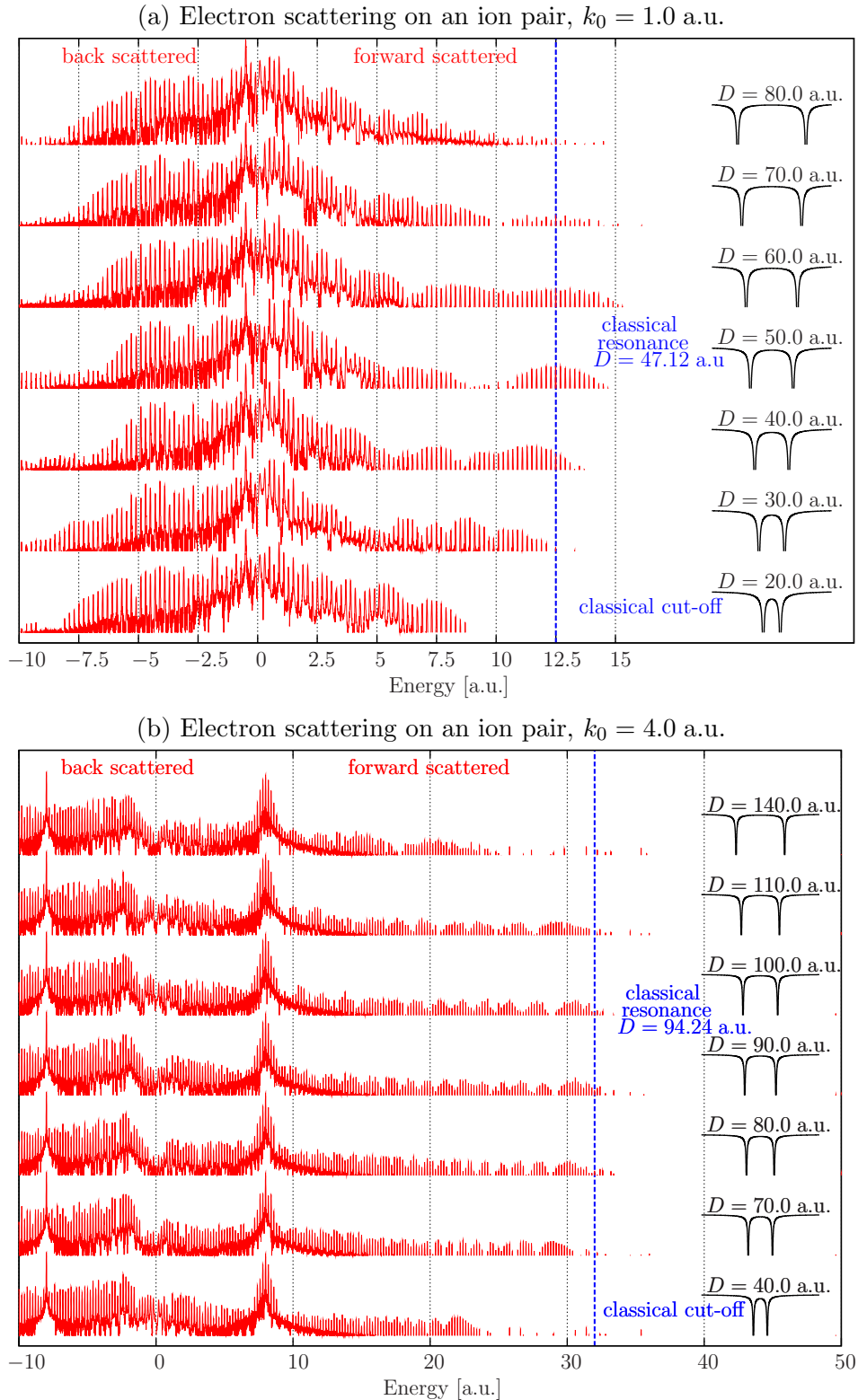
$$E = \frac{k^2}{2} = (k_0 \pm 2v_0)^2. \quad (6.5)$$

Table 6.1 gives the cut-off energies in the case of single ion scattering shown previously. The comparison with the TDSE calculations presented in Fig. 6.2 for  $k_0 = 1.0$  a.u. and  $k_0 = 4.0$  a.u. show accurate agreement concerning the high-energy cut-offs in the spectrum of the scattered electron (blue dashed lines in the electron spectra).

### 6.1.3 Scattering on ion pairs: resonance phenomena

Using the classical approach of instantaneous Coulomb collisions allows for a simple derivation of a resonance condition for an optimal distance  $D$  of two ions where a maximum energy yield of the scattered electrons should be achieved [11]. Fig. 6.3 (a) shows the considered scattering geometry and (b) illustrates the occurring scattering processes with the classically expected momentum transfers. The first process is in analogy to the single ion scattering. The wave packet separates into the reflected part considered previously and a transmitted fraction which is now of special interest. This transmitted part can scatter with the second ion where it increases its momentum according to Eq. (6.4). A maximum momentum transfer is obtained if the electric field of the laser has its maximum and acts in the correct direction. Then the electron is able to accumulate up to  $2v_0$  additional momentum and travels back to the first ion. If the distance  $D$  of the two ions is accurately chosen such that the electric field has changed its direction completely when the electron hits the left core, it again increases its momentum in a second scattering process. The

6 Coulomb scattering



**Figure 6.4:** Wave packet scattering on an ion pair. Both figures show the electron energy distribution after the collision process for different distances  $D$  of the two ions (schematically drawn in the right). The whole setup is placed in a strong laser field,  $\omega = 0.2$  a.u. and  $E_0 = 0.2$  a.u. The classically expected cut-offs in the energy are indicated by the blue dashed lines and are estimated within the static field limit.

## 6.1 Coulomb scattering in a one-dimensional model

optimal distance is therefore simply given by half of the laser period and the initial momentum  $k_0$  of the electron:

$$D = \frac{1}{2}(k_0 + 2v_0) \cdot T = (k_0 + 2v_0) \cdot \frac{\pi}{\omega}. \quad (6.6)$$

$v_0$  is again the amplitude of the quiver velocity of the electron in the laser field. Since the electron is faster after the second collision this resonance condition is not fulfilled for a following scattering event and it leaves the arrangement to the right with increased momentum.

The maximum energy gain of the twice scattered electrons is then

$$E_{\max} = \frac{1}{2}(4 \cdot v_0 + k_0)^2. \quad (6.7)$$

Table 6.2 contains the estimation of cut-off energies and the corresponding resonance distances  $D$  for different initial momenta  $k_0$  of the wave packet. A strong laser field with  $\omega = 0.2$  a.u. and  $E_0 = 0.2$  a.u. is assumed.

The resulting electron energy spectra obtained from TDSE simulations [50] are displayed in Fig. 6.4 for  $k_0 = 1.0$  a.u. and  $k_0 = 4.0$  a.u. The distance between both scattering centers is varied around the classical resonance condition, Eq. (6.6). Fig. 6.4 (a) shows the complete spectrum for forward and backward scattered electron distributions. The backward scattered part shows nearly the same behavior as in the case of single ion scattering. This is not surprising because an important fraction of the wave packet is already scattered without reaching the second Coulomb potential. The spectrum of the forward scattered electron, Fig. 6.4 (a) and (b), now shows an enhanced plateau up to the classical cut-off energy in the case of a resonant distance between both ions. Hence the classical static field limit is, also in this case, a reasonable approximation. The distinct photon peaks indicate again the energy absorption process in the laser field. For the scattering of electrons with  $k_0 = 4.0$  a.u. an energy of up to 64.0 Rydberg can be observed. This corresponds to an energy of 870 eV. Therefore already this setup can be used to accelerate electrons on microscopic dimensions ( $\approx 5$  nm).

### 6.1.4 Scattering on chains of Coulomb potentials

The next step is to increase the maximal energy transferred to the electron by choosing further improved scattering setups. A naïve idea is to simply add more Coulomb potentials to the system — at the correct distances. Unfortunately the reflection and transmission properties of the Coulomb potential change with the energy of the scattered particle by orders of magnitude, cf. Fig 4.7 (b). Therefore higher-order scattering processes are less likely and the already small fraction of high-energy electrons will be decreased significantly for each additional collision. Nevertheless an optimal setup for Coulomb potentials can be derived with the help of the classical static field limit.

#### Scattering on an arrangement of three ions

A first approach is to add one more ion, i.e., one additional Coulomb potential. The occurring setup is given in Fig. 6.5 (a). The expected scattering processes, which increase the energy of the electron, are schematically drawn in Fig. 6.5 (b). The already demonstrated process leading to a fast-electron distribution by scattering on two ions is accompanied by a collision process on the third ion. To maximize the momentum transfer it has to be placed at a resonant distance  $D_2$  from the first ion in that sense that the electric field has changed its direction when the already accelerated electron reaches the rightmost potential. This field behavior is visualized by

## 6 Coulomb scattering

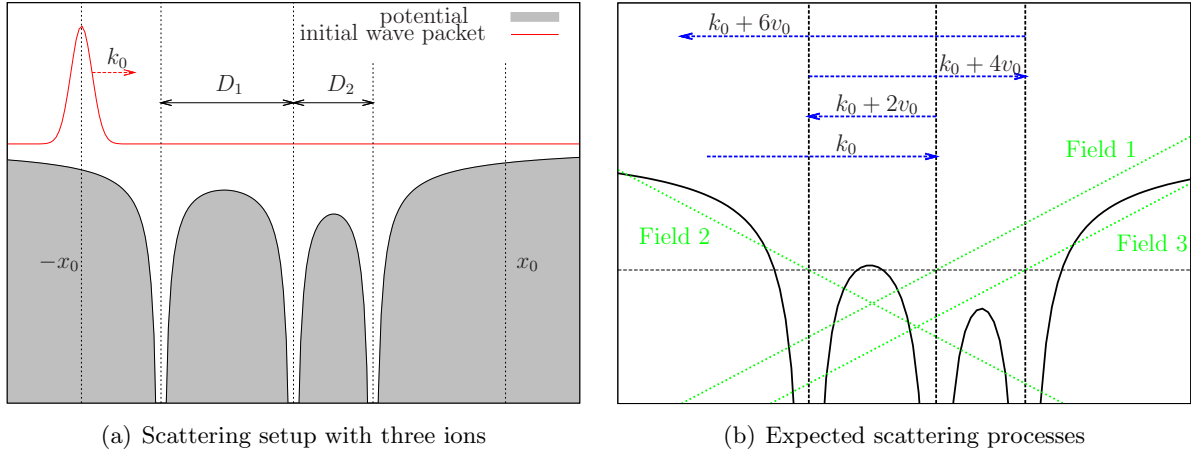


**Figure 6.5:** Scattering on an arrangement of three ions within the distances  $D_1$  and  $D_2$ . All other quantities are the same as in Fig. 6.3.

$k_0$	$D_1$	$D_2$	$E_{\text{cut-off 1}}$	$E_{\text{cut-off 2}}$	$E_{\text{cut-off 3}}$
1.0	47.12	31.4	4.5	12.5	24.5
4.0	94.24	31.4	8.0	32.0	50.0

**Table 6.3:** Recapitulatory table of all cut-off energies which can be identified in a scattering process on three ions in the resonant distances  $D_1$  and  $D_2$  (Fig. 6.6) in the strong laser field ( $\omega = 0.2$  a.u.,  $E_0 = 0.2$  a.u.).

the green lines in Fig. 6.5 (b) marked by “Field 1 . . . 3”.

The first two ions are placed at the same distance like in the previous case, cf. Eq. (6.6),

$$D_1 = (k_0 + 2v_0) \cdot \frac{\pi}{\omega}. \quad (6.8)$$

The electrons scattered by this process gain the momenta given by Eq. (6.4). Hence, the optimal distance for the additional potential from the first ion is given by

$$D_1 + D_2 = (k_0 + 4v_0) \cdot \frac{\pi}{\omega}$$

which leads to

$$D_2 = 2v_0 \cdot \frac{\pi}{\omega}. \quad (6.9)$$

According to this formula, the third ion has to be placed at a distance independently of the initial momentum  $k_0$  since only the additional momentum absorbed from the electric field by the last scattering process plays a role. An estimation of the maximum energy yield and the distances  $D_1$  and  $D_2$  is shown in Table 6.3. For  $k_0 = 4.0$  a.u. this corresponds to electrons with an energy of 1.3 keV, accelerated over a setup which measures only 6.5 nm.

Since the electron collides with the third ion lastly, the distribution with the highest kinetic energy is expected to be scattered to the left of the whole arrangement. But due to the transmission and reflection properties the total intensity should be small. Figure 6.6 shows the resulting energy spectrum of a wave packet scattering simulation,  $k_0 = 1.0$  a.u. The laser properties are as before. The ions are placed at the distances  $D_1$  and  $D_2$  according to Table 6.3 where an optimal energy yield is expected. Since the spectra of those multiple scattering processes contain very weak signals, these kinds of simulations have to be done very carefully. Otherwise the signal of

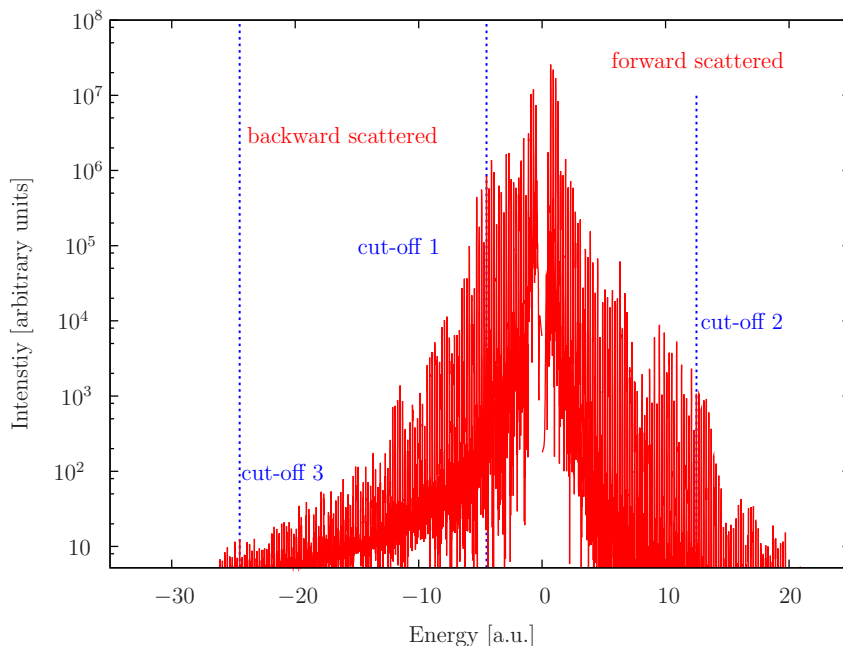


**Figure 6.6:** Wave packet scattering  $k_0 = 1.0$  a.u. on an arrangement of three ions in resonant distances in a strong laser field,  $\omega = 0.2$  a.u.,  $E_0 = 0.2$  a.u. The energy spectrum is obtained from a numerical solution of the TDSE. The classical cut-off energies, cf. Table 6.3, are indicated by blue dashed lines.

the three-fold scattered electron cannot be distinguished from the underlying numerical noise. Therefore very fine grids with parameters  $\Delta t = 0.001$  and  $\Delta x = 0.0125$  are used. This increases the computational effort enormously because very large computational grids ( $N \geq 200000$  and  $N_t = 480000$ ) are required. For these parameters the signal of the third scattering process can clearly be identified in the electron spectrum (cut-off 3 in Fig. 6.6). The noise is more than one order of magnitude lower. Furthermore the traces of all other scattering processes described previously in this chapter can be found in the spectrum: the scattering on one single ion in the backward scattered fraction (cut-off 1) and the two-fold scattered fraction of electrons in the forward direction (cut-off 2). Therefore, the instantaneous Coulomb collisions model developed in [10] is also able to describe all significant cut-offs in Fig. 6.6.

Since the reflection coefficient of the one-dimensional Coulomb potential is increased dramatically if  $\kappa$  is decreased, the total yield could be increased if the cut-off parameter is chosen to be smaller for the last Coulomb potential. But since an adjustable cut-off parameter, as it is essential for 1D simulations, does not have any physical meaning, these further investigations were not (yet) performed. A more physical approach is the change of the atomic number  $Z$  for the related potential since it also affects the transmission and reflection rates of the whole setup. However, introducing a third ion with an atomic number of  $Z = -0.1$  a.u., i.e., a higher reflection coefficient, does not noticeably change the situation. A significant increase in the intensity of high-energy electrons, compared to the case shown in Fig. 6.6, could not be verified in the simulations.

### Scattering on longer chains

As displayed in Fig. 6.5 (b) the exiting electron beam from a setup consisting of three ions lies in the direction of the incident electron wave packet. Hence a further increase in the energy yield can only be achieved if this exiting electron collides with an additional ion. This ion has to be placed in front of the first one. Therefore it seems to be impossible to enhance the shown

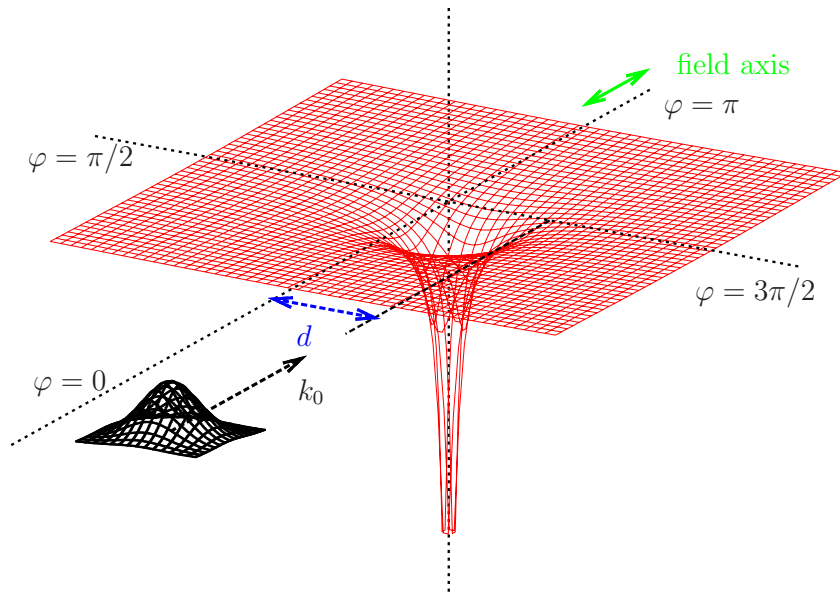


**Figure 6.7:** Schematic drawing of the two-dimensional scattering setup. A wave packet with initial momentum  $\mathbf{k}_0 \parallel x$  is launched on the  $x$ -axis ( $\varphi = 0, \pi$ ). An additional scattering parameter  $d$  adjusts the distance from a central collision of the wave packet center. The laser field — if included — is linearly polarized along the same axis (green arrow).

setup to longer chains of potentials by using the same energy absorption mechanism introduced above. However, lots of situations with equidistant and non-equidistant potentials have been simulated but no significant resonances could be found. A more sophisticated setup which uses the non-monotonous behavior of the quantum reflection and transmission properties of potentials is proposed in the last chapter “Outlook”.

## 6.2 Two-dimensional Coulomb scattering

The one-dimensional model allows for an easy and fast access to scattering processes in (strong) laser fields and the corresponding distribution of fast electrons. Nevertheless it is not able to make robust predictions for experiments since the intensity of high-energy electrons is clearly overestimated due to an additional angular degree of freedom. A two-dimensional model is somewhat closer to reality. As already shown in Chapter 5.2.3, the angular distribution of electrons emitted by multi-photon processes can accurately be calculated within a two-dimensional model. Thus the generalization of the 1D case gives us the opportunity to investigate the angle dependence of the scattering processes observed previously and additionally a possibility to estimate the total yield of the high-energy electrons in each direction.

First of all, we present a recap of the well-known scattering of particles on a single Coulomb potential in three dimensions. This leads to the famous Rutherford formula and the corresponding cross sections. These are then compared with the results of two-dimensional wave packet scattering (solutions of the TDSE). Additionally, this formalism is set into relation with the classical trajectories of a scattered particle. Then the collision of electrons with single ions in laser fields, beginning with low-intensity fields, and the change in the cross sections caused by a linearly polarized pulse are discussed. Finally, the scattering geometries constructed in the previous part are extended to the two-dimensional case and adjusted to increase the total yield of fast electrons [51, 52].

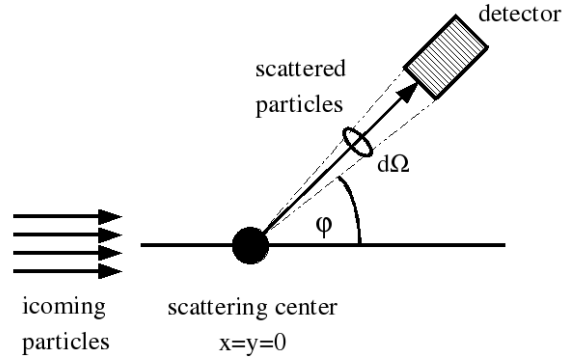


**Figure 6.8:** Scattering geometry for particle scattering on a potential at  $x, y = 0$ . The incident particle beam is scattered into the solid angle element  $d\Omega$  at the scattering angle  $\varphi$ .

### 6.2.1 Coulomb scattering without a laser field

First we will discuss the elastic scattering of particles, in our case electrons, on positively charged ions without any laser field. In this case an analytical solution is possible and leads to the well-known Rutherford formula [53]

$$\frac{d\sigma}{d\Omega} = \left( \frac{Z_1 Z_2}{4E} \right)^2 \frac{1}{\sin^4(\varphi/2)}. \quad (6.10)$$

For naming conventions see Fig. 6.8. Eq. (6.10) gives the differential scattering cross section for a particle scattered on a Coulomb potential. It determines the fraction between the number of scattered particles per time and solid angle element  $d\Omega$  and the total number of incoming particles per time and area.  $Z_1$  and  $Z_2$  are the atomic numbers of the collision partners, which can be positive or negative. Within this thesis  $Z_1 = -Z_2 = 1.0$  a.u. is chosen.  $\varphi = 0 \dots \pi$  is the scattering angle at which the fraction  $d\sigma/d\Omega$  of particles is detected. The initial energy of the particle far away from the partner is denoted by  $E$ . The angle-dependent cross section replaces the transmission and reflection coefficients of the one-dimensional potential. The intensity predicted by the Rutherford formula diverges at scattering angles where the sine function vanishes. This is a direct effect of the long-range potential, i.e., a Coulomb effect. In reality this singularity plays no important role since nearby scattering centers will prevent its appearance. As will be seen in the discussion of the classical trajectories below, this singularity stems from particles collected from regions with extremely large scattering parameters  $d$ .

It is remarkable that Eq. (6.10) is exact in the case of pure Coulomb interaction. The classical derivation first done by Rutherford and nowadays printed in many introductory textbooks on physics, gives exactly the same result as a full quantum mechanical treatment of the scattering process. Here an additional interesting property of the Coulomb potential can be found: the quantum mechanical derivation of Eq. (6.10) in the first Born approximation and the complete exact calculation, e.g. given in [54], agree.

We now turn our attention to wave packet scattering in two dimensions. Fig. 6.9 shows a comparison of wave packet scattering (numerically obtained TDSE solution) on a repulsive Coulomb potential (a) and an attractive Coulomb potential (b) to its classical analogon. The density  $|\Psi(x, t)|^2$  is indicated by contour lines for the initial wave packet at the left and for a snapshot at a time after the scattering process ( $t = 25$  a.u.). Additionally, the classical trajectories are drawn (red solid lines). These were obtained by solving Newton's equations of

## 6 Coulomb scattering

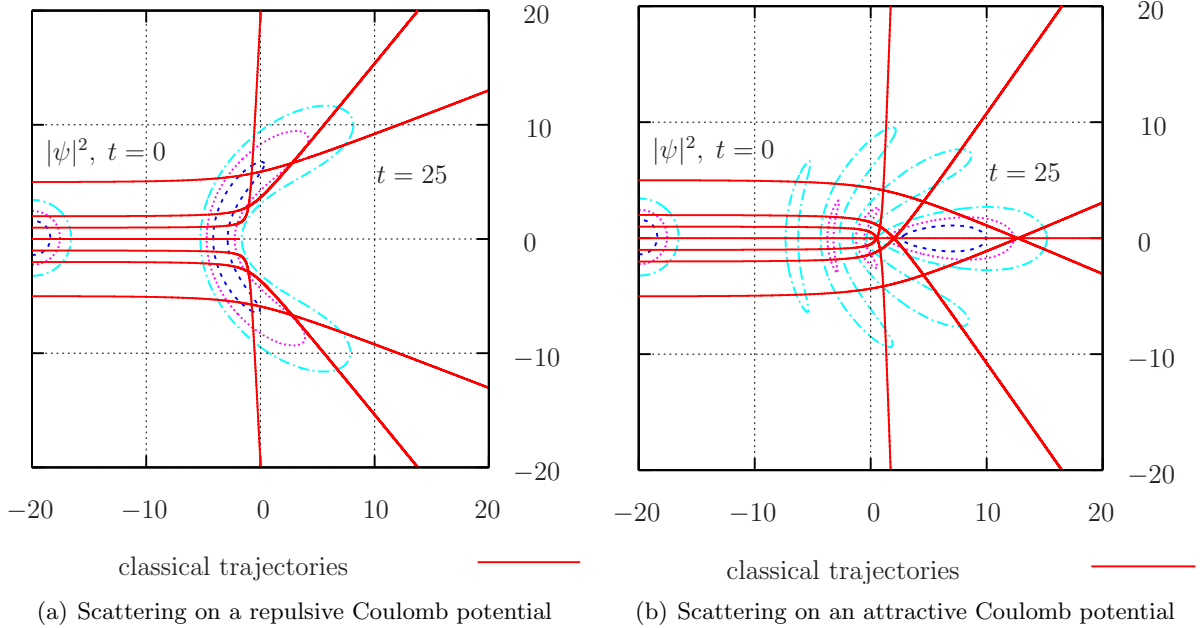


**Figure 6.9:** Two-dimensional scattering on one single repulsive (a) and attractive (b) Coulomb potential in the center of the figures. Shown are the classical trajectories (red solid lines) of a particle obtained by solving Newton’s equations of motion for different scattering parameters  $d$ . The contour plots are density snapshots from quantum calculations (TDSE solution of wave packet scattering,  $k_0 = 1.0$  a.u.) for the initial state (left) and a state after the collision (right,  $t = 25$  a.u.) [43].

motion using a standard 4th-order Runge-Kutta integration method. All physical parameters are the same for the quantum and for the classical calculations. As one easily sees, the wave packet formalism gives access — due to the spatial width  $\sigma$  of the initial distribution — to a plethora of possible classical trajectories. Each corresponds to a different scattering parameter  $d$ , cf. Fig. 6.7.

The density of the electron is mainly located in the vicinity of the classical paths. But this is — of course — not the whole story: the scattering process in the quantum case is much more involved. An interference pattern discussed later arises in the case of an attractive Coulomb potential, Fig. 6.9 (b). Additionally, for quantum calculations the transmission and reflection properties of the potential come into play and the equality of Eq. (6.10) to its full quantum mechanical counterpart is, in fact, just a coincidence. Nevertheless, what one should keep in mind is that the wave packet formalism involves a distribution of scattering parameters  $d$ . Together with the quantum properties of the potential (reflection/transmission), the scattering of the electron into an arbitrary angle  $\varphi$  is possible, even in the case of wave packets with small width  $\sigma$ . This spatial effect is supplemented by the additional uncertainty in the momentum space which makes even more trajectories accessible.

To construct the corresponding cross sections, we now analyse the angular distribution of such scattering processes. Fig. 6.10 shows the angle- and energy-resolved spectrum of the wave packet after colliding with a soft-core Coulomb potential (TDSE solution for (a)  $k_0 = 1.0$  a.u. and (b)  $k_0 = 2.0$  a.u.). First one immediately recognizes that the spectrum corresponds to elastic scattering. Since no relevant absorption processes or exciting forces are present, the peak intensity appears at the free particle energy  $E = k_0^2/2$  for each scattering angle  $\varphi$ . The width in the energy domain is a direct consequence of the small spatial size of the wave packet ( $\sigma = 10.0$  a.u.). The main intensity appears at an angle of  $\varphi = \pi$ . This is the direction of the initial momentum  $k_0$ . The intensity experiences an angle-dependent modulation similar to the

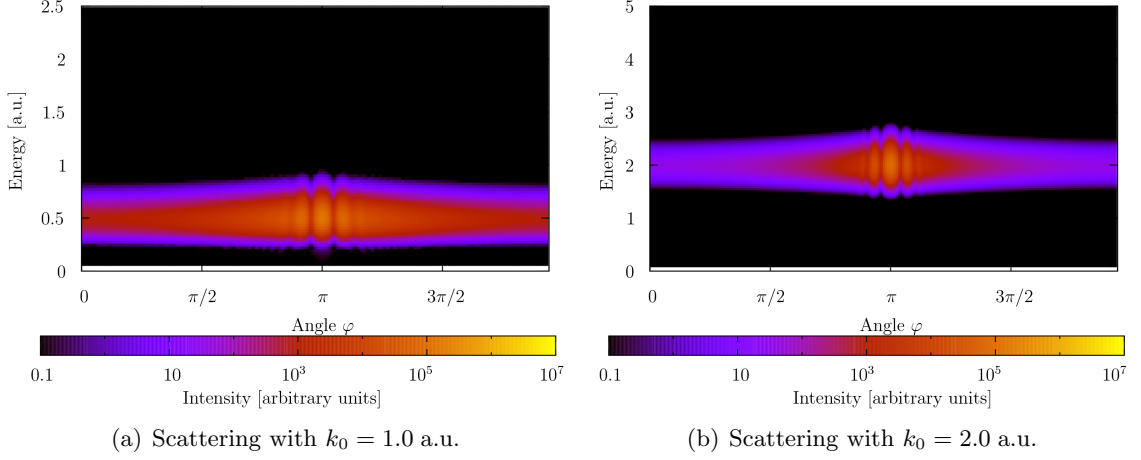


**Figure 6.10:** Energy- and angle-resolved spectrum of Coulomb scattering without a laser field. The width of the initial wave packet is chosen to be  $\sigma = 10.0$  a.u. A detector is placed at a distance  $r = 50$  a.u.,  $\varphi = \pi$  indicates the direction of the initial wave packet. The resolved distribution corresponds to elastic scattering with  $E = k_0^2/2 = 0.5$  a.u. and  $E = 2.0$  a.u. resp.

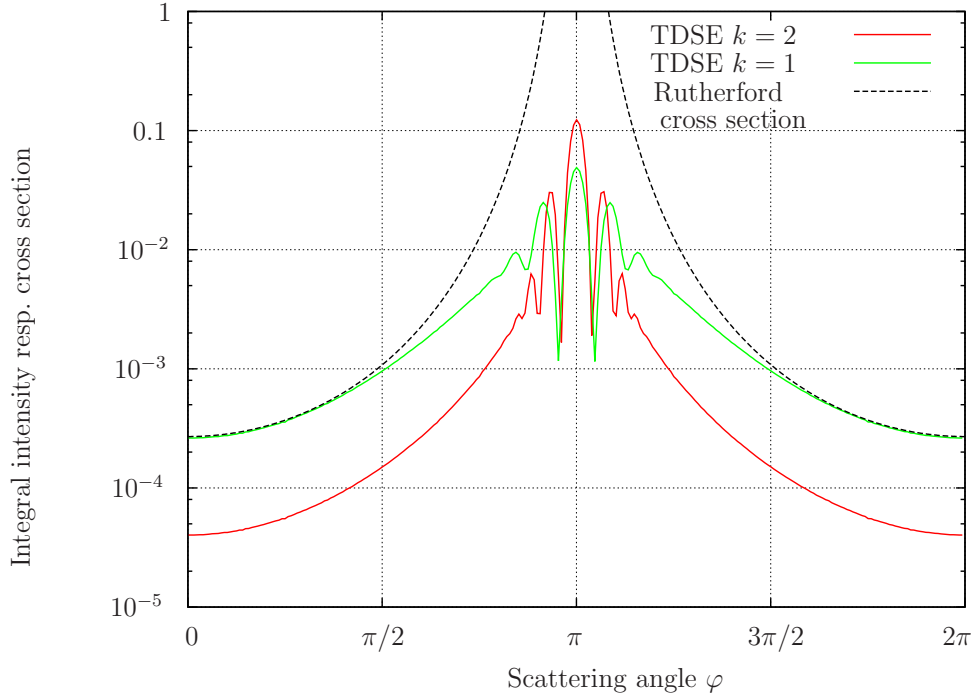


**Figure 6.11:** Angle-dependent scattering probability: Rutherford cross section, cf. Eq. (6.10) shifted by  $\pi$ , compared with a time-dependent two-dimensional soft-core Coulomb collision using wave packets ( $k_0 = 1.0$  a.u. and  $k_0 = 2.0$  a.u.). The angle-resolved energy distribution of the TDSE solution, cf. Fig. 6.10, is integrated over all energies. Additionally, the angular integrated spectrum is normalized to unity. The Rutherford cross section is fitted to the asymptotic behavior of the  $k_0 = 1.0$  a.u. case (green line).

## 6 Coulomb scattering

interference phenomenon observed in a single slit experiment. For higher initial momentum  $k_0$ , and therefore higher energies  $E$ , the parts scattered into large angles are significantly smaller. This agrees with the Rutherford formula, Eq. (6.10), where  $E$  appears in the denominator.

The total cross section for a particle being scattered at an angle  $\varphi$  is obtained by integrating the angle-resolved spectrum over the energy. This result can then be related to Eq. (6.10). Fig. 6.11 shows the normalized intensity for both situations discussed in Fig. 6.10. Additionally, the Rutherford cross section, fitted to the graph for the case  $k_0 = 1.0$  a.u., is drawn. It describes the scattering at large angles very well but the distribution for small angles differs a lot. The singularity in the Rutherford cross section is diminished. This is a direct effect of the finite size of the wave packet. Since the Coulomb potential “collects” all particles (probability distributions) for large scattering parameters  $d$  and focuses them to the angle  $\varphi = \pi$ , the wave packet formalism shows a significantly smaller intensity. Furthermore, the modulation already mentioned appears in the integrated spectrum. In this illustration the relation to the interference pattern is more obvious. The behavior of the intensity can be qualitatively explained with the formula [55]

$$I(\varphi) = \frac{\sin^2 x}{x^2} \quad \text{with} \quad x = \pi \cdot b \cdot k \sin(\varphi) . \quad (6.11)$$

$b$  describes the width of the slit and  $\varphi$  denotes the diffraction angle measured from the optical axis. The oscillations are faster for larger values of  $k$ . This dependence can be identified in the numerically obtained graphs, Fig. 6.11. One also recognizes that the fraction of total backward scattered electrons ( $\phi = 0, 2\pi$ ) is very small compared to the incident wave packet. Additionally, it is further decreased for larger momenta ( $k_0 = 2.0$  a.u., red line). This already illustrates the difficulties that will arise when the one-dimensional scattering situations presented in the previous part are generalized to the 2D case.

### 6.2.2 Including laser fields

We have now developed the tools for investigating two-dimensional Coulomb scattering processes in laser fields. We restrict ourselves to linearly polarized fields in this work. Fig. 6.7 indicates the polarization direction of the field along the  $x$ -axis which is also the direction of the incoming particle beam. The influence of the field strength  $E_0$  of a laser for a fixed photon energy  $\omega = 0.2$  a.u. is presented in Fig. 6.12. First of all, relatively weak fields ( $E_0 \leq 0.01$  a.u.) seem to have nearly no effect on the scattering process itself. The energy integrated angular spectrum shows no significant field dependence. But for laser intensities approaching the strong field regime ( $E_0 \geq 0.05$  a.u.), a change especially in the distribution of backward scattered electrons can be observed. For  $E_0 = 0.05$  a.u. the curve in Fig. 6.12 is shifted upwards whereas in the case of a strong field ( $E_0 = 0.2$  a.u.) additional new angle-dependent features arise. The direction of the laser field polarization ( $\varphi = 0, 2\pi$ ) becomes visible by two maxima. Two significant drops, marked with  $p_1$  and  $p_2$  in Fig. 6.12, are identified and a strong increase of approximately one order of magnitude in the intensity of backward scattered electrons is obtained. Thus this direction of scattering becomes more likely in the case of a linearly polarized laser field - depending strongly on the intensity. This effect is important because the probability of backward scattering is an important quantity for efficient generation of fast electrons by scattering processes.

### 6.2.3 Scattering on one ion in a strong laser field

We now have a detailed look at the scattering of electrons on one single ion in a strong laser field in two dimensions. The increased fraction of backward scattered electrons was already mentioned. Fig. 6.13 shows the energy- and angle-resolved spectrum of 2D wave packet scattering on a single

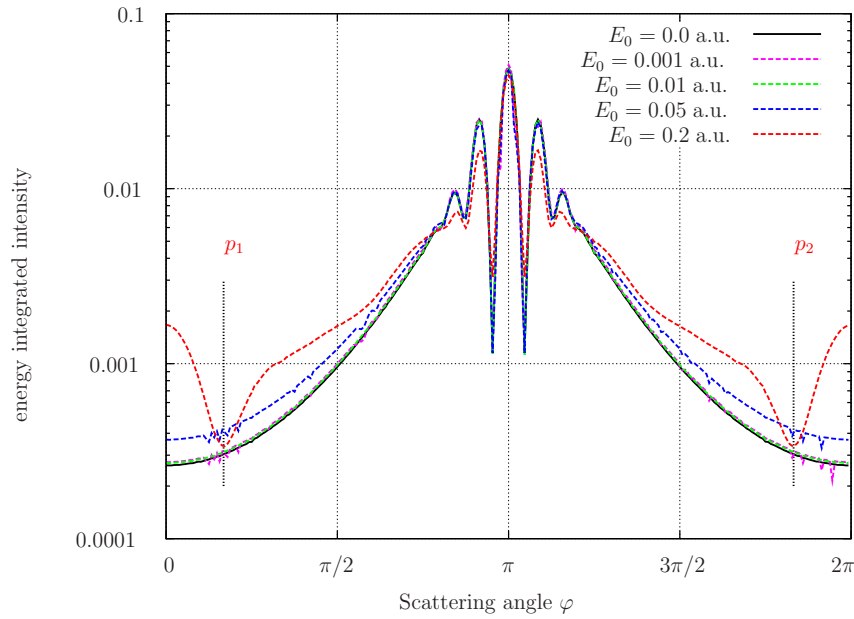


**Figure 6.12:** Energy integrated angular distribution for the intensity of scattered electrons after the collision with one single ion depending on the electric field strength of the laser ( $\omega = 0.2$  a.u.). The initial momentum of the wave packet was chosen to be  $k_0 = 1.0$  a.u. for all calculations.

ion for two different initial momenta  $k_0$ . The detector is placed at a distance of  $r = 75.0$  a.u., which is large compared to the active scattering region. Furthermore, it was assured that the variation of  $r$  does not change the electron spectra. Hence, near-field effects are negligible in the formation of the presented spectra. The strong angle dependence, not only in the cross section but also in the energies, becomes apparent. As in the one-dimensional case a plateau in intensity in the distribution of backward scattered electrons ( $\varphi = 0, 2\pi$ ) is observed. The cut-off energy can be identified to approximately  $E_{\text{cut-off}} = 5$  a.u. for  $k_0 = 1.0$  a.u. ( $E_{\text{cut-off}} = 8$  a.u. for  $k_0 = 2.0$  a.u.) which agrees with the instantaneous Coulomb collision model introduced for the 1D case. The forward scattered fraction, with most intensity coming from the elastically scattered part of the wave packet at  $\varphi = \pi$  and an energy  $E = k_0^2/2$ , exhibits also an increase in energy. In analogy to the one-dimensional setup a cut-off energy can be identified. The relation between multi-photon processes in scattering processes and the above threshold ionization becomes again visible (cf. Fig. 5.10).

In both spectra the photon orders are clearly separated by exactly the photon energy  $\omega = 0.2$  a.u., although for numerical reasons a small width of  $\sigma = 10$  a.u. in the case for  $k_0 = 1.0$  a.u. ( $\sigma = 40$  a.u. for  $k_0 = 2.0$  a.u.) is chosen. Furthermore, both distributions show qualitatively a similar structure but in the case of  $k_0 = 2.0$  a.u. an additional angular quantization with forbidden regions at certain scattering angles  $\varphi$  becomes visible. This has to be an effect of angular momentum conservation. As shown previously for the case of the ionization of different states (cf. Chapter 5) the emission at specific angles is impossible due to the dipole selection rules which are a consequence of angular momentum conservation ( $\Delta l = \pm 1$ ). Fig. 6.13 (b) visualizes that each absorption of a photon shifts the forbidden regions by a certain angle. This can then be connected with the increase of the angular momentum of the electron by a constant factor for each subsequent photon line. Thus, the arising fringe structure seems to be a trace of the multi-photon ladder.

If one now remembers the result of the scattering process with slow electrons ( $k_0 = 0$ ), shown in Chapter 5, Fig. 5.12, one recognizes that no angle-dependent substructure is present whereas

## 6 Coulomb scattering

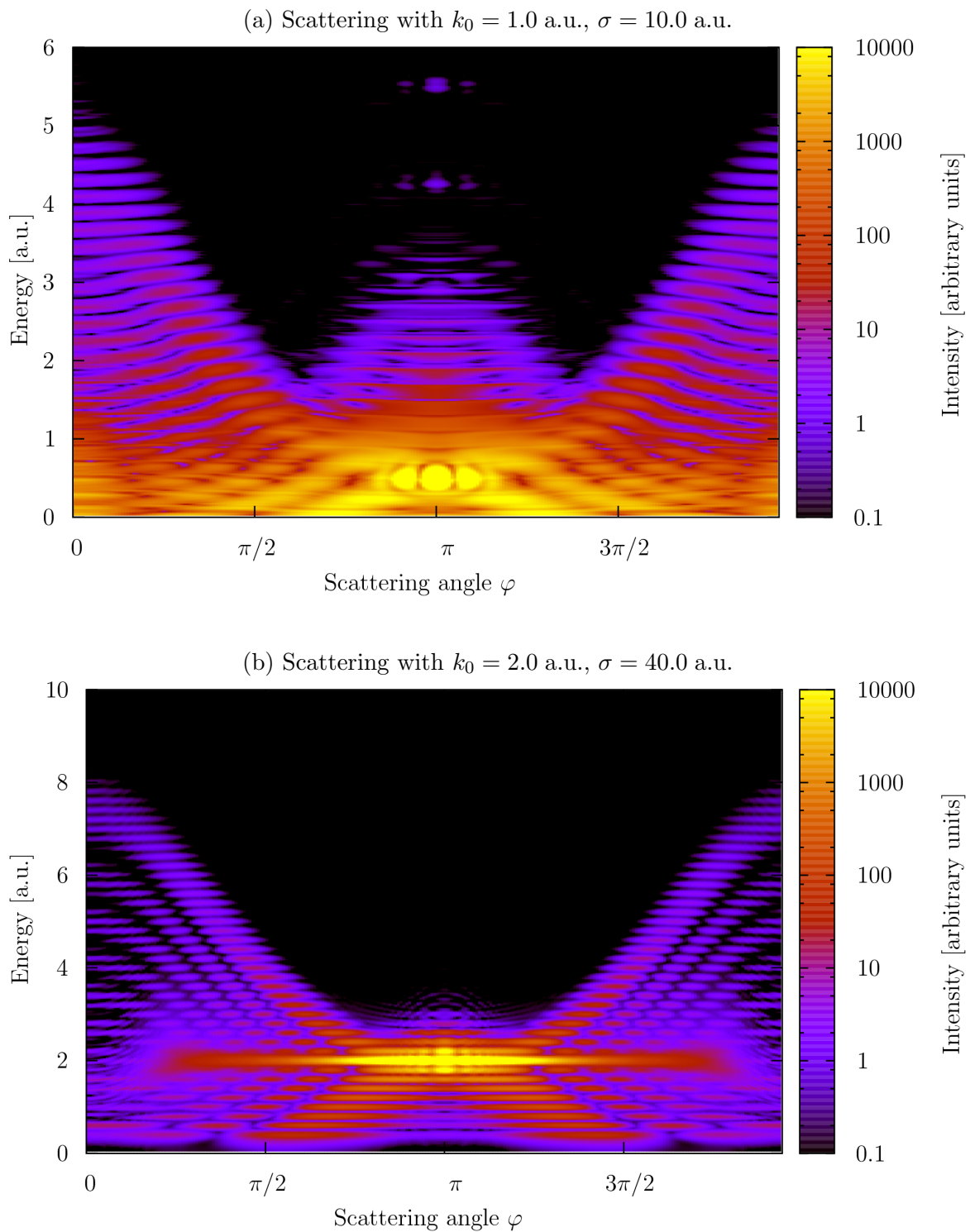


**Figure 6.13:** Energy- and angle-resolved electron spectra of central ( $d = 0$ ) wave packet scattering on one single ion in a strong laser field  $\omega = 0.2$  a.u. and  $E_0 = 0.2$  a.u. The electrons are detected at a distance of  $r = 75.0$  a.u. The spectra are not dependent on this special choice.

## 6.2 Two-dimensional Coulomb scattering

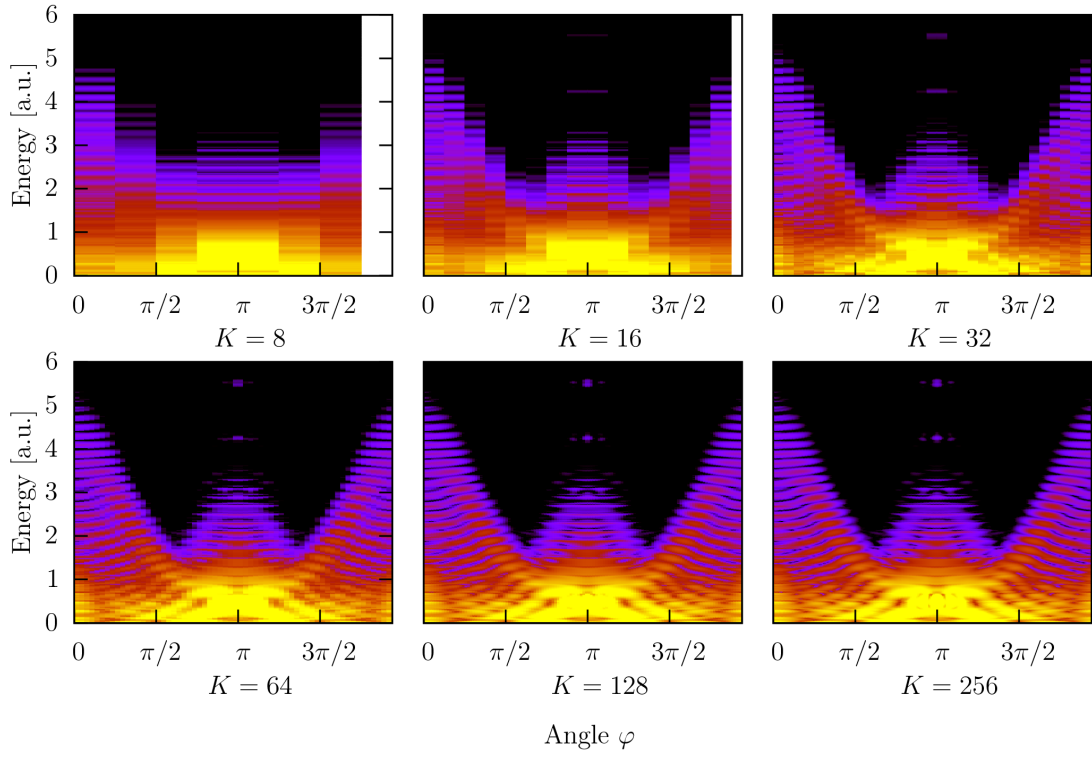


**Figure 6.14:** Central wave packet scattering ( $d = 0$ ) on one single Coulomb potential in a strong laser field ( $\omega = 0.2$  a.u.,  $E_0 = 0.2$  a.u.) for different detector resolutions  $\Delta\varphi = 2\pi/K$ . The initial momentum is chosen to be  $k_0 = 1.0$  a.u., the width  $\sigma = 10.0$  a.u.

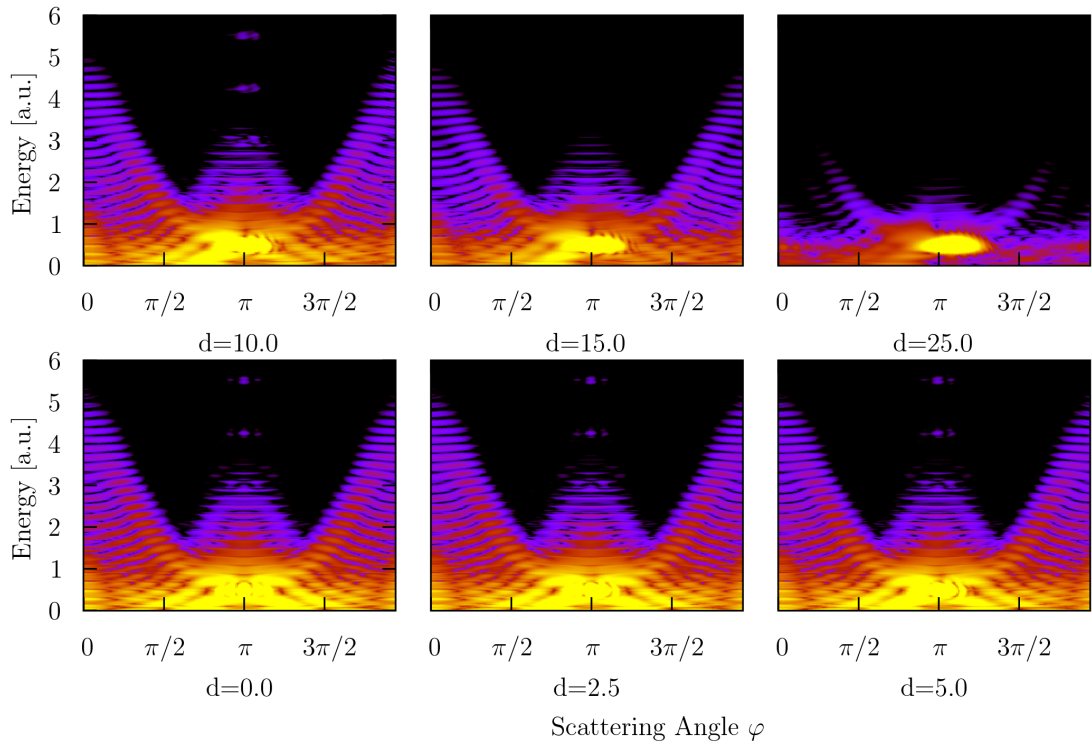


**Figure 6.15:** Same setup as Fig. 6.14 but for different scattering parameters  $d$ . The parameter of the resolution was fixed at  $K = 256$ .

## 6 Coulomb scattering

in the case of scattering with  $k_0 = 1.0$  a.u., Fig. 6.13 (a), already a weak modulation can be spotted (indicated by a shift in each photon line). One can now conclude that the additional initial momentum  $k_0$  and the corresponding angular momentum of non-central parts of the wave packet (with respect to the central potential) play an important role in the formation of this substructure. Further investigations, on numerical as well as on an analytical basis, are planned.

The resolution of the detector is a limiting factor for the experimentalist. Of special interest is therefore, how the angle-resolved spectra depend on the angular resolution of a possible detector. Fig. 6.14 shows the spectrum for the case  $k_0 = 1.0$  a.u. with different parameters  $K$  (cf. Chapter 3.4.2, Fig. 3.5) The resolution is simply given by  $\Delta\varphi = 2\pi/K$ . As one can easily see, the substructures in the spectrum vanish but the main cut-off energies are still resolvable for nearly all investigated parameters  $K$ . Of course the finer the resolution, large  $K$ , the more underlying structures like angular quantization are observable. But the distribution of fast electrons generated by collisions in laser fields are detectable over a wide range of resolutions.

The next question is how the spectra are affected when the wave packet is not sent centrally ( $d = 0$ ) to the scattering region which is difficult to realize experimentally. A simple idea for an experiment occurred during the discussion of this work [56]:

The positively charged ions are made available by an ion beam and the electrons are irradiated perpendicular to the direction of ions. The crossing point of both beams is located in a strong, linearly polarized laser field, e.g., the X-FEL at DESY Hamburg. This setup will lead to collisions with scattering parameters  $d$  distributed over a wide range. But as already mentioned previously in the discussion of the classical trajectories, the wave packet scattering formalism already shows this distribution intrinsically. Only the intensity at specific angles should vary if the center of the wave packet travels on a trajectory displaced from the central axis. Fig. 6.15 shows the wave packet calculations with  $k_0 = 1.0$  a.u. for different scattering parameters  $d$ . The graph with  $d = 0$  is the same as in the previous picture, Fig. 6.13 (a). The results support the arguments above. The structure of the spectra is not affected by variation of  $d$ . Only the intensity decreases and up to  $d = 15.0$  a.u. nearly no change is observed. The main peak at  $\varphi = \pi$  is shifted to the angle of the new scattering axis which can be identified as an effect of the relatively small distance  $r$  between the scattering center and the detector. But the main contributions to the fast electrons in the backward direction are not affected. For  $d = 25.0$  a.u. this fraction finally vanishes in the background because nearly no part of the wave packet hits the ion anymore (finite width  $\sigma = 10.0$  a.u. of the wave packet). Thus the process of generating fast electrons should be detectable also in the case of scattering with an ensemble of scattering parameters  $d$ .

### 6.2.4 Scattering on an ion pair

In the following, the generation of high-energy electrons by correlated collisions in strong laser fields (see Chapter 6.1.3) is extended to 2D scattering geometries. As mentioned in the first part for the one-dimensional case, the optimal setup to increase the total energy yield formed by two ions can be estimated with the help of the classical resonance condition, Eq. (6.6). This equation holds also for the multi-dimensional case, since we have restricted ourselves to linearly polarized laser fields. For the case of  $k_0 = 1.0$  a.u. this corresponds to a distance  $D = 47.12$  a.u., cf. Table 6.2, of the two scattering centers. The considered setup is sketched in Fig. 6.16. The wave packet is launched centrally ( $d = 0$ ) towards the scattering centers. The field is polarized along the direction of the alignment of the ion pair, which corresponds to an angle of  $\varphi = 0, \pi$ . As we already learned from electron scattering on single ions in the 2D case, the expected effect is weaker as for the one-dimensional setup. The cross sections for backward scattering, where the maximum energy yield is obtained, is very small. Additionally, we are interested in the special

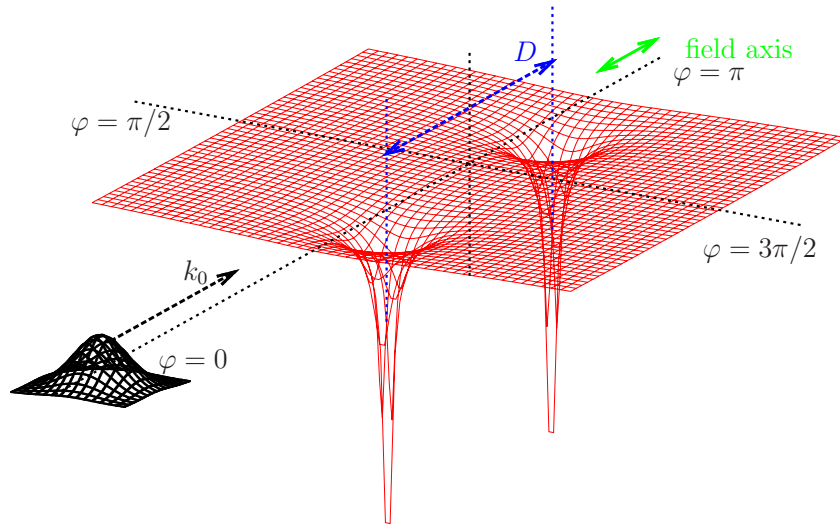


**Figure 6.16:** Two-dimensional wave packet scattering on an ion pair in a laser field.

case of doubly scattered electrons, and therefore an even smaller fraction of scattered particles.

The simulations, i.e., the solutions of the TDSE, have to be performed on very large spatial grids since the initial wave packet needs a sufficient width  $\sigma$  and the scattering process itself needs to be followed for a reasonable scattering time over several laser periods, comparable to those in 1D. Additionally, due to the expected weakness of the effect, the simulation parameters  $\Delta x$  and  $\Delta t$  have to be adjusted carefully. Choosing parameters too large will increase the noise in the spectra and hide the expected physical effect in the background. Choosing  $\Delta x$  too small makes the simulations nearly impossible since the grid becomes incredibly large. A dimension of 300 a.u.  $\times$  300 a.u. seems to be a reasonable simulation box size but already with a resolution of  $\Delta x = 0.05$  a.u. this corresponds to an enormous amount of  $3.6 \times 10^7$  grid points. Here, the advantage of an effective imaginary absorbing potential becomes apparent. Additionally, the detected wave function becomes a computational challenge. It needs to be stored on approximately 16000 grid points to give a sufficient resolution for *all* time steps, which can easily increase up to  $N_t = 96000$  since  $\Delta t$  has to be chosen sufficiently small. A total amount of several ten GB of data is created for each simulation run which need to be post processed by effective algorithms to obtain the angle-resolved energy spectra.

After a detailed analysis with different parameters  $\Delta x$  and  $\Delta t$ , grid sizes and zero-padding for the FFT algorithms, the best spectrum of the detected electrons after the scattering process is given in Fig. 6.17. The final numerical parameters are given in the caption. The significant cut-off energy for the single ion scattering process in the backward direction ( $\varphi = 0, 2\pi$ ) is again identified ( $E_{\text{cut-off}} \approx 5$  a.u.). The photon orders are well resolved and separated by the photon energy  $\omega$ . But in comparison to the single ion scattering spectrum, cf. Fig. 6.13 (a), the distribution is strongly distorted due to the second collision event.

However, the expected second classical cut-off in the forward direction, which corresponds to the electrons with the highest kinetic energy, cannot be reliably identified. It vanishes in the numerical noise of the spectrum (black regions in the graph correspond to the noise level). Still, a very weak distribution in the forward direction can be observed. An interpretation of the missing signal is straightforward: The fraction of the wave packet being scattered at the second ion, namely the backward scattered fast electrons from the first collision, is too small in the two-dimensional system to give a reasonable intensity for the second collision. Nevertheless the

## 6 Coulomb scattering

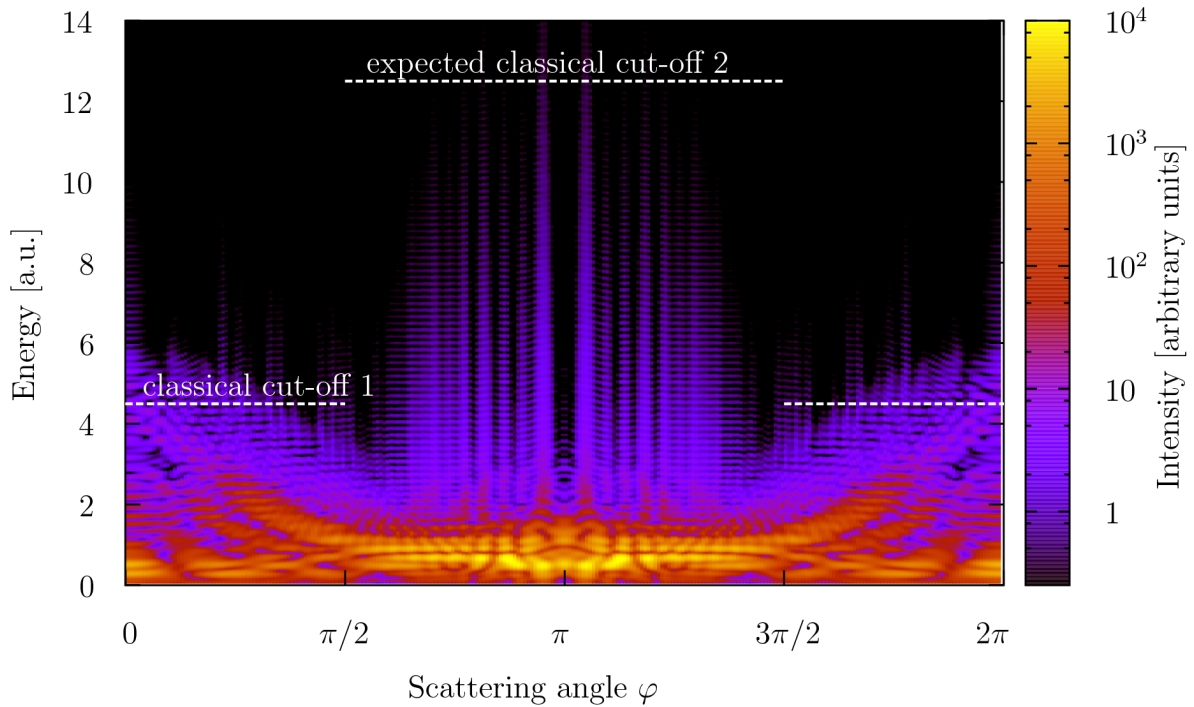


**Figure 6.17:** Electron energy spectrum of wave packet scattering on two ions,  $k_0 = 1.0$  a.u.,  $D = 47.12$  a.u. The simulation parameters are:  $N = 7500$ ,  $M = 5000$ ,  $\Delta x = \Delta y = 0.05$ ,  $\Delta t = 0.005$ ,  $N_t = 96000$ . Laser parameters as before:  $\omega = 0.2$  a.u.,  $E_0 = 0.2$  a.u. The classical estimations for the cut-off energies according to the instantaneous Coulomb collision model are indicated by white dashed lines. They hold for complete backward ( $\varphi = 0, 2\pi$ ) and forward ( $\varphi = \pi$ ) scattering.

distorted substructure in the spectrum due to multiple collisions is of interest since it should be present in all scattering experiments in the gas phase where such resonant distances between two particles should appear occasionally. Further investigations of this fundamental process in gases and plasmas seem to be worthwhile since there are also open questions, for instance, in the generation of higher harmonics which can possibly be explained by such correlated collisions [57].

### 6.2.5 Scattering in a confined setup

A possible way to overcome the problem of the vanishing signal discovered in the case of pure two-dimensional scattering is to use an additional confinement potential. This leads to two valuable effects: firstly, the electrons are focused into the desired directions of true forward respectively backward scattering. Secondly, it allows for the usage of smaller, i.e., rectangular, grids. This helps keep the simulation time smaller and enormously decreases the required memory size. Therefore the entrapment of the scattering setup has beneficial effects on the physical nature of the problem as well as on the numerical treatment within the TDSE framework.

Throughout the remaining part of the present chapter, a harmonic confinement with the trap frequency  $\Omega$  along the  $y$ -direction, i.e. perpendicular to the scattering direction, is used (cf. Fig. 6.18):

$$V_{\text{conf}} = \frac{1}{2} m \Omega^2 y^2 . \quad (6.12)$$

The initial conditions for the simulation are adjusted according to the trap: along the  $x$ -

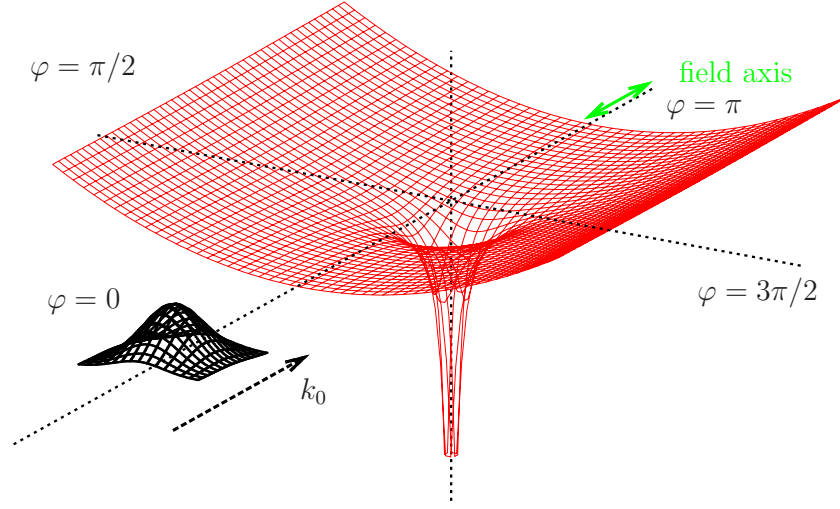


**Figure 6.18:** Scattering on one single ion in an additional harmonic confinement along the  $y$ -direction.

direction a free traveling Gaussian wave packet with the initial momentum  $k_0$  is still used. In the  $y$ -direction however, the first eigenstate of the harmonic confinement, i.e., a Gaussian distribution with the width  $\sigma_y = 1/\sqrt{\Omega}$  is chosen.

The confinement now allows for grid sizes in  $x$ -direction which are comparable to those in the 1D problem since the size of the numerical grid in  $y$ -direction is strongly limited. The grid resolution is determined according to the maximum energy occurring in the expected scattering processes. This cut-off energy is estimated by means of the classical approximation presented above. The grid size is identified by the condition that the confinement energy at the grid boundary should be significantly larger than the highest expected kinetic energy of the electron in order to avoid perturbing boundary effects. It appears that for trap frequencies used herein, a relatively small grid in  $y$ -direction is adequate. Therefore large widths in the  $\mathbf{k}_0$  direction of the initial wave packet are possible and lead to a high energy resolution for the scattering process itself.

### Scattering on one single ion

First we are interested in a comparison with solutions already obtained and a survey of the influence of different confinement strengths. Therefore, wave packet scattering on a single ion in a harmonic confinement is considered. Within this setup the transition from the one-dimensional geometry to the 2D system can be investigated. Fig. 6.19 shows the energy spectrum of the backward scattered electrons in a pure 1D, a pure 2D and entrapped systems of different confinement strengths. The laser parameters are as usual ( $\omega = 0.2$  a.u.,  $E_0 = 0.2$  a.u.). The initial momentum of the wave packet in  $x$ -direction is  $k_0 = 1.0$  a.u. and its width is chosen to be  $\sigma = 50$  a.u.

In order to obtain comparable results, the calculations of the spectra were done by integration over an angle of  $\Delta\varphi = 0.2/2\pi$  centered at the direction of total backward scattering ( $\varphi = 0$ ). After the integration, the spectra are normalized.

Furthermore, one has to keep in mind that the choice of the first eigenstate of the harmonic potential in  $y$ -direction adds energy to the system. Hence, it is increased by

$$E_0 = \Omega \left( n_y + \frac{1}{2} \right) = \Omega/2. \quad (6.13)$$

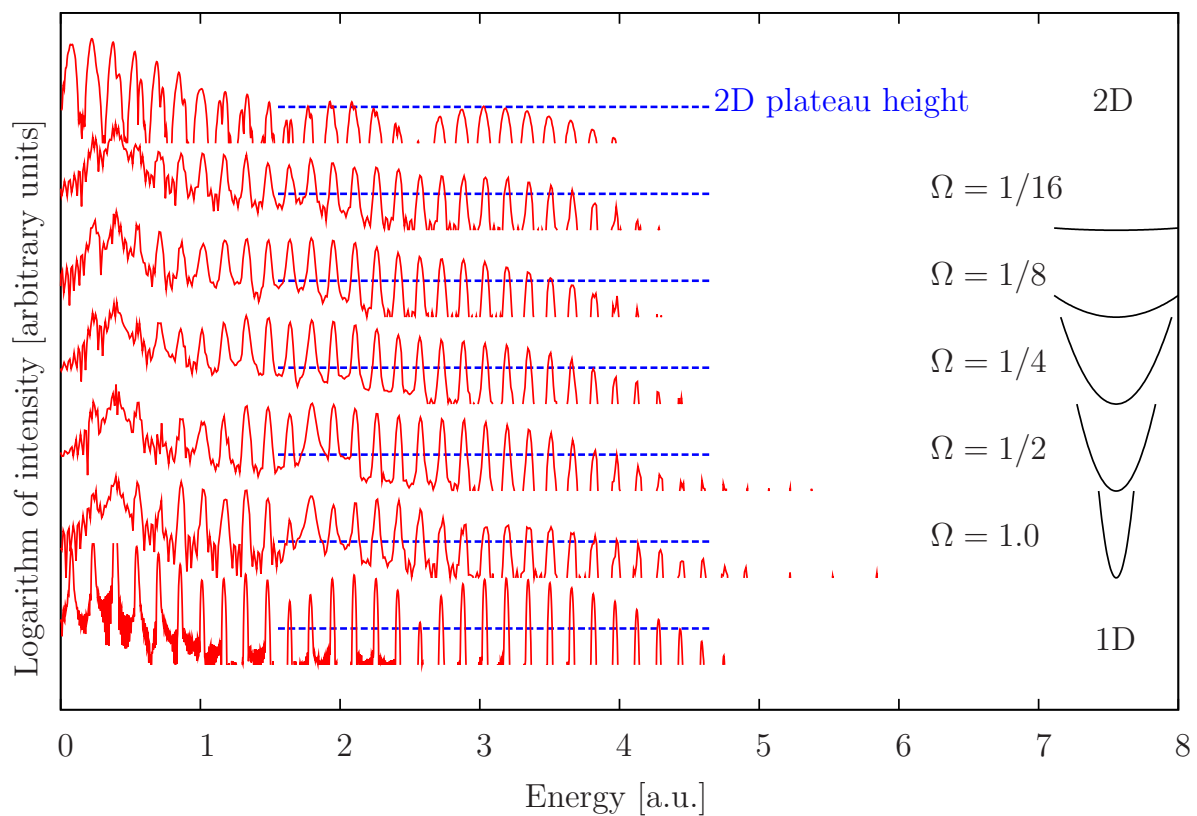


**Figure 6.19:** Energy spectra of the backward scattered fraction of an electron-ion collision in a strong laser field ( $\omega = 0.2$  a.u.,  $E_0 = 0.2$  a.u.). The graphs show the result for the pure two-dimensional case (uppermost spectrum), the pure one-dimensional case (lowest graph) and the result for different confinement strengths  $\Omega$ . Weaker confinement is closer to the 2D case, stronger confinement closer to 1D. The trap is schematically drawn in the right. The intensity of each spectrum ( $y$ -axis) runs from  $10^{-5}$  to 1 on a logarithmic scale. The background noise level is below the plotted graphs. The blue dashed line indicates the height of the intensity plateau found in the 2D calculation as a reference.

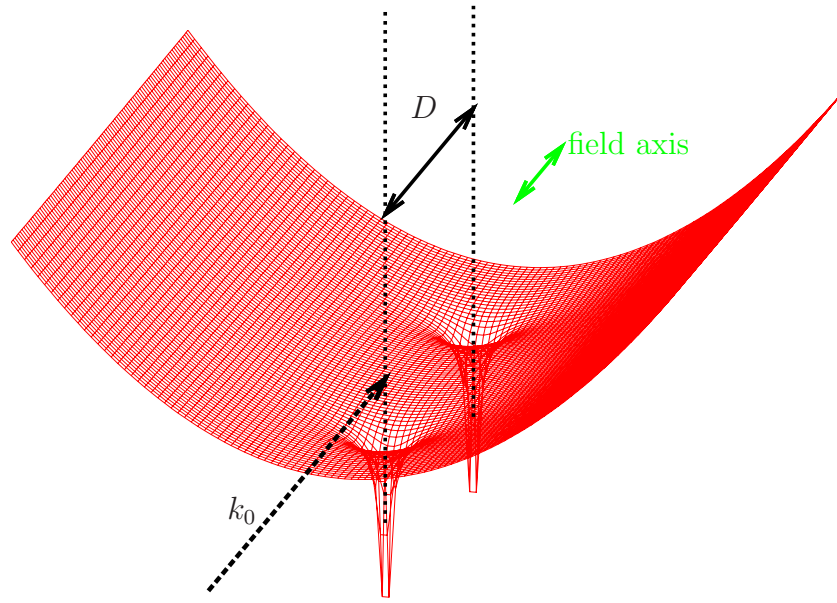


**Figure 6.20:** Scattering on an arrangement of two confined ions in a laser field.

To account for this effect, the energy scale for each spectrum in Fig. 6.19 is shifted by the corresponding value. At first glance, one recognizes the accurately obtained photon orders which are located at the same energies for all systems considered. Thus the shift of the energy scale according to Eq. (6.13) is correct. Furthermore, all spectra show a similar structure with a cut-off energy within the same energy region. For a comparison of the intensities (logarithmic scale) the height of the backward scattering plateau for the 2D case is indicated by a blue dashed line. The trend which arises by introducing the confinement is easily observed: The intensity of backward scattered electrons is increased with stronger entrapment. This is of course the effect of the expected focusing. The comparison with the 1D calculations (lowest graph) is difficult. The normalization of the spectrum underestimates the total yield since no corresponding angle element is available. Therefore the blue line should be located somewhat lower as indicated in Fig. 6.19. Further calculations — also on larger grids with a better signal to noise ratio — are planned for the future.

### Scattering on an ion pair

In this last part we discuss the correlated scattering on an ion pair in a harmonic confinement. The whole setup is schematically given in Fig. 6.20. The laser field is polarized along the alignment axis of both ions which also corresponds to the external trap. The laser parameters are as usual ( $\omega = 0.2$  a.u. and  $E_0 = 0.2$  a.u.). The initial momentum of the incoming electron was chosen to be  $k_0 = 1.0$  a.u. and again in  $y$ -direction the first eigenstate of the harmonic potential with  $\Omega = 1.0$  a.u. has been used. This trap frequency results in a very strong confinement. Both ions are placed at a distance  $D = 47.12$  a.u. which allows for the generation of resonantly scattered electrons with high energies. The corresponding energy spectrum of the forward and backward scattered electrons is shown in Fig. 6.21. The spectra are obtained as in the single ion case by integrating over an angle element  $\Delta\varphi = 0.1$ , but now for both directions,  $\varphi = 0$  and  $\varphi = \pi$ .

The strong asymmetry (as observed in the one-dimensional case, cf. Fig. 6.4) in the spectrum becomes apparent, i.e., the relatively low-energy part of backward scattered electrons and the broad plateau of forward scattered electrons with higher energies. The intensity structure

## 6 Coulomb scattering

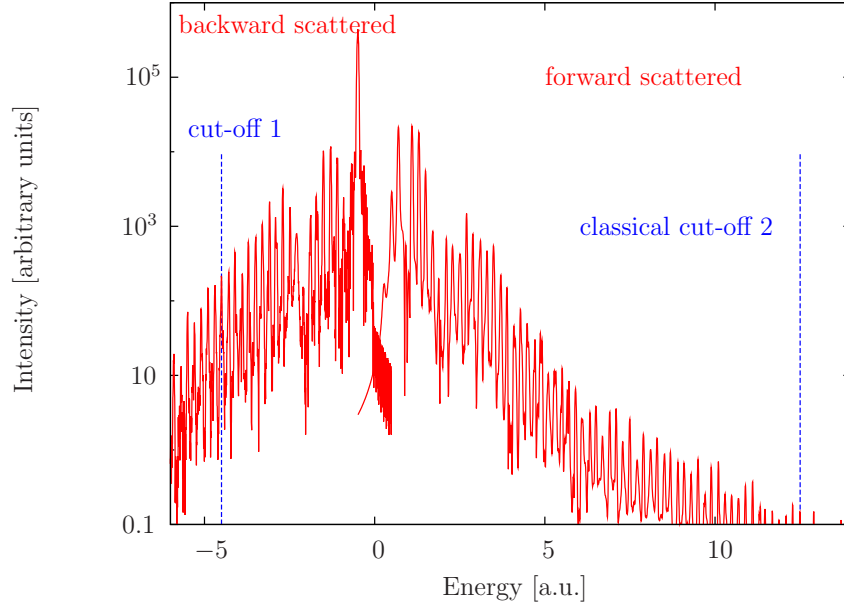


**Figure 6.21:** Energy spectrum of a correlated electron-ion pair collision,  $k_0 = 1.0$  a.u., in a harmonic confinement with  $\Omega = 1.0$ . The laser field parameters are  $\omega = 0.2$  a.u.,  $E_0 = 0.2$  a.u. Negative energies indicate backward scattering and forward scattering is marked by positive energies. The classical cut-off energies (instantaneous Coulomb collision model) are denoted by dashed blue lines. The highest peak results from the incident electron energy with  $E = k_0^2/2$ .

of the one-dimensional case, especially the substructure of the height of subsequent photon peaks, cannot be reproduced accurately within this model. Nevertheless the classical cut-offs can be identified more readily than in the pure two-dimensional case and therefore the additional harmonic confinement allows for the construction of a more efficient scattering setup in two dimensions.

As in the case of single ion collisions presented above, cf. Fig. 6.19, an analogous effect of focusing due to the external confinement can be observed in the simulations of correlated scattering processes. By comparison of the resolved intensity of doubly scattered electrons without confinement, Fig. 6.17, and the results shown in Fig. 6.21 ( $\Omega = 1.0$  a.u.), one finds an increase in the yield of high-energy electrons by several orders of magnitude. Due to the vanishing signal in the case of ion pair scattering for  $\Omega = 0$ , a more precise quantification is not possible. However, since the signal of the twice scattered electrons can be verified for  $\Omega = 1.0$  a.u., the introduction of an additional harmonic confinement promises an increase of efficiency in the generation of high-energy electrons by correlated scattering processes.

A (last) remark on a possible experimental realization is in order. The scattering centers, i.e., the ions, can be represented by interfaces in a semi-conductor hetero-structure [58]. The specific shape of a Coulomb potential is not the critical necessity. The distance between both scattering centers, or alternatively the laser frequency, has to be adjustable to allow for resonant scattering. The external confinement is the limiting factor. It should be very strong, especially for the generation of very high-energy electrons. This may be achievable, e.g., with tip electrodes near a surface.

## 7 Conclusions and outlook

In the present work ionization processes and electron-ion collisions in the presence of (strong) laser fields were addressed. The central method was the numerical solution of the time-dependent Schrödinger equation (TDSE). To this end a code package based on the Crank-Nicolson method and the alternating direction implicit procedure was developed. It allows for the solution of the multi-dimensional TDSE on large spatial grids in the usual laboratory frame as well as in the adapted Kramers-Henneberger [40, 41] representation which eliminates the quiver motion of an electron in a time-dependent field. The program contains routines for the construction of initial conditions such as the shooting method and the imaginary time propagation [36] which give access to the eigenstates of the considered potential. Furthermore the calculation of various quantum mechanical observables is included, with special interest in the calculation of the energy distribution of scattered or ionized electrons. This was achieved by modelling a detector-like situation in combination with (imaginary) absorbing potentials.

The convergence behavior and several tests of the implemented code were presented within this thesis showing the desired agreement with well-known analytical results. The central systems investigated in the work were based on the one- and two-dimensional Coulomb potential. As it is necessary for their numerical treatment, regularized soft-core potentials were used to prevent the singularity at  $x = 0$ . The arising complications such as broken degeneracies were discussed in detail. In addition the formalism of wave packet scattering was accurately described and applied to potentials in order to obtain quantum properties as, e.g., their transmission and reflection coefficients. These implemented and well-tested techniques allowed for the investigation of ionization, emission and scattering processes in strong laser fields on a microscopic level. The results are restricted to linearly polarized laser fields with intensities up to  $7 \cdot 10^{15} \text{ W/cm}^2$ . The coupling of the electro-magnetic field to the Hamilton operator is treated within the classical electro-dynamics and, for simplicity, the dipole approximation is used which appeared to be sufficient for the systems investigated.

One central topic of the thesis at hand was the investigation of excitation and ionization of electrons initially bound in model potentials such as the regularized Coulomb potential. Within manageable one-dimensional systems, well-known linear phenomena occurring for excitations in the perturbative regime were confirmed numerically. In particular, the dipole-selection rules and Fermi's golden rule were addressed. For two-dimensional situations, the numerical solution of the TDSE gave access to the angle-resolved distribution of photoionized electrons. Distinct minima depending on the angular momentum  $l$  of the initial state were observed, corresponding to forbidden ionization angles. These numerical results could be verified in the calculations of the allowed angle-dependent dipole transitions. To this end the dipole matrix elements for transitions between bound atomic states and free plane waves with certain angles of the wave vector  $\mathbf{k}$  measured with respect to the laser polarization axis were calculated. In addition, these two-dimensional results were generalized to the 3D hydrogen atom. Depending on the initial state preferred directions for the emission of electrons could also be observed.

Moreover, non-linear multi-photon processes with the focus on above threshold ionization (ATI) in strong laser fields were simulated within the framework of the TDSE and compared with results obtained within the strong field approximation (SFA) firstly introduced by Keldysh [18]. Good agreement, besides the well-known deviations of the SFA due to long-range Coulomb

## 7 Conclusions and outlook

effects [24], could be demonstrated. Furthermore, angle-resolved ATI spectra for different initial states of a two-dimensional model hydrogen atom were calculated. As a related effect to ATI [10], the scattering of slow electrons (with initial momentum  $k_0 = 0$ ) on a single Coulomb potential was investigated and the connection to the issue of “Coulomb scattering in strong laser fields” could be pointed out. In both cases MP processes are the dominant effects leading to accelerated electrons.

Another concern of the present thesis was the investigation of electron-ion collisions ( $k_0 > 0$ ) in strong laser fields with the goal to generate high-energy electrons by correlated scattering processes. Within a one-dimensional model, based on ideas by H.-J. Kull [10, 12], the energy-transfer mechanisms between laser field and electrons by collision processes were illustrated. With the help of the classical approach of *instantaneous Coulomb collisions*, cut-off energies in the electron spectra could be estimated and resonance conditions for setups consisting of two and three spatially fixed ions could be derived. Simulations of wave packet scattering with the help of numerical solutions of the TDSE confirmed the results predicted by the classical treatment. A distribution of scattered, high-energy electrons could be observed exhibiting kinetic energies up to 50 times higher than their initial energy. These electrons were accelerated over a scattering setup in a laser field ( $I = 7 \cdot 10^{15}$  W/cm<sup>2</sup>) which measured only a few nanometers.

To account for additional angular degrees of freedom in real experiments, this one-dimensional approach was extended to the 2D case. It was demonstrated that high-energy electrons can be generated by collisions on single ions in this model as well. The investigation of angle-resolved electron spectra revealed that the maximum energy yield is obtained by direct backward scattering where the cut-off energies agree with the one-dimensional case. Indeed, the intensity of high-energy electrons is significantly decreased due to the additional possible scattering directions. An observed angle-dependent substructure in the spectra pointed at angular momentum conservation during the MP process. We addressed several, especially for the experimentalist, interesting aspects, such as detector resolutions and variation of the scattering parameter. The results indicate that the fraction of fast electrons generated by single-ion collisions should be detectable in measurements.

The last part of the thesis generalized the investigated correlated scattering processes in one dimension to the two-dimensional case. As expected, the generation of high-energy electrons by collision on two spatially correlated ions is not as efficient as in the 1D case. To overcome this problem an additional external harmonic confinement was introduced which focuses the electrons in the direction of the highest energy yield. Within TDSE simulations a significant increase in the yield of high-energy electrons could be verified, promising that this method is a possible way for the generation of fast electrons by correlated scattering processes on the nanometer scale.

### Outlook

The work on the thesis at hand revealed several questions unanswered up to this point. As mentioned in Chapter 6.2.3, the occurring angle-dependent fringe structure in the spectra of scattered electrons needs a well-founded theoretical explanation. Furthermore, the influence of the additional external confinement on the generation of high-energy electrons and the corresponding increase in intensity is not exhaustively investigated, cf. Chapter 6.2.5. Further calculations with improved methods, e.g. parallelized algorithms in order to be able to use larger grids, may be worthwhile to consider.

Additionally, the code already available allows for the investigation of two-color experiments which gives the possibility for time-resolved analysis of electronic dynamics in laser fields. This offers a wide range of further applications [7]. Finally, it is planned to explore correlated many-body effects in strong laser fields based on other theoretical approaches, as e.g. outlined in [15]. Here, the results obtained within the thesis at hand offer profound benchmarks.

As a final remark on the generation of fast electrons by scattering processes, can be mentioned that the mechanism of acceleration due to correlated electron-ion collisions in laser fields is not necessarily restricted to Coulomb or Coulomb-like potentials. Also the consideration of probably more efficient quantum well and quantum dot structures may be worthwhile. Here, advantage can be taken of the non-monotonous behavior of the transmission and reflection properties of the potentials to increase the total fraction of optimally scattered electrons by filtering effects.

## *7 Conclusions and outlook*

# A Conversion of atomic units

Quantity	Formula Symbol	basic unit	SI-Value	cgs-Value
Mass	$m_e$	mass of electron	$9.1094 \times 10^{-31}$ kg	$9.1094 \times 10^{-28}$ g
Charge	$e$	charge of electron	$1.602 \times 10^{-19}$ As	$4.803 \times 10^{-10}$ esu
Action	$\hbar = h/2\pi$	Planck's constant	$1.0544 \times 10^{-34}$ Js	$1.0544 \times 10^{-27}$ erg-sec
Length	$a_0$	$a_0 = \hbar^2/m_e e^2$ Bohr radius	$5.2917 \times 10^{-11}$ m	$5.2917 \times 10^{-9}$ cm
Energy	$E_0$	$e^2/a_0$ : twice the ionization energy of hydrogen atom (1 hartree = 2 rydbergs)	$2 \cdot 2.1799 \times 10^{-18}$ J = 27.210 eV	
Time	$t_0$	$\hbar/E_0$ : orbit time for ground state electron in hydrogen atoms	$2.4189 \times 10^{-17}$ s	$2.4189 \times 10^{-17}$ sec
Velocity	$v_0$	$a_0/t_0$ : velocity of electron in the first Bohr orbit of hydrogen atoms	$2.1877 \times 10^6$ m/s	$2.1877 \times 10^8$ cm/sec
Cross section	$\sigma$	Area of the first Bohr orbit $\pi a_0^2$ of hydrogen atoms	$0.88 \times 10^{-20}$ m <sup>2</sup>	$0.88 \times 10^{-16}$ cm <sup>2</sup>
Vacuum velocity of light	$c$	$c/v_0 = 137.037$ a.u. = $1/\alpha$ where $\alpha$ is Sommerfeld's fine structure constant	299792458 m/s	29979245800 cm/sec
Field strength	$\mathbf{E}$	Coulomb field on electron in hydrogen atoms in the distance of $a_0$	$5.1418 \cdot 10^{11}$ V/m	$5.1418 \cdot 10^9$ V/cm
Frequency	$\omega$	$E_0/\hbar = 1/t_0$	$4.134 \cdot 10^{16}$ Hz	$4.134 \cdot 10^{16}$ 1/sec
Intensity	$I$	intensity boundary between atom-electron and field-electron interaction	$3.4 \cdot 10^{16}$ W/cm <sup>2</sup>	

**Table A.1:** Conversion between atomic units (a.u.), SI-units and cgs-units for several quantities. The choice  $m = e = \hbar = 1$  generates the atomic system of units.

*A Conversion of atomic units*

## B Frequently used abbreviations

---

ADI	alternating direction implicit (method)
APT	attosecond pulse train
ATI	above threshold ionization
CE phase	carrier envelope phase
c.m.	center of mass
FFT	fast Fourier transform
HHG	higher harmonics generation
IR	infrared (radiation)
ITP	imaginary time propagation
KFR theory	Keldysh-Faisal-Reiss theory (SFA)
KH-frame	Kramers-Henneberger coordinate frame of reference
MP	multi-photon
MPI	multi-photon ionization
NEGF	non-equilibrium Green's function
OBI	over barrier ionization
QED	quantum electro dynamics
SFA	strong field approximation
TDDFT	time-dependent density functional theory
TDSE	time-dependent Schrödinger equation
VUV	vacuum ultraviolet
X-FEL	X-ray free-electron laser
XUV	extreme ultraviolet

---

**Table B.1:** List of frequently used abbreviations and notations (alphabetical order).

*B Frequently used abbreviations*

$\Psi^{\text{KH}}$	wave function in Kramers-Henneberger frame
$\Psi^{\text{lab}}$	wave function in laboratory frame
$\mathbf{A}$	vector potential of electro-magnetic field
$\mathbf{A}^*$	vector potential $\mathbf{A}$ multiplied by $c$
$k_0$	initial momentum of wave packet
$\sigma$	spatial width of wave packet
$E_0$	electrical field strength of laser
$\omega$	photon energy of laser
$v_0$	amplitude of quiver velocity
$\kappa$	regularization parameter for Coulomb potential
$\varphi$	scattering angle
$K$	detector resolution ( $2\pi/K = \Delta\varphi$ )
$\Delta t$	time step size
$\Delta x, \Delta y$	spatial step size
$N_t$	number of time steps
$N$ and $M$	number of spatial grid points $(x, y)$

**Table B.2:** notations and formula symbols

## C The Schrödinger equation in the Kramers-Henneberger coordinate frame

In the following it is shown that  $\Psi^{KH}(\mathbf{r}, t)$  satisfies

$$-\frac{1}{2}\Delta\Psi^{KH}(\mathbf{r}, t) + V[\mathbf{r} + \boldsymbol{\alpha}(t)]\Psi^{KH}(\mathbf{r}, t) = i\frac{\partial}{\partial t}\Psi^{KH}(\mathbf{r}, t) \quad (\text{C.1})$$

By using the Kramers-Henneberger ansatz for the wave function  $\Psi^{KH}(\mathbf{r}, t) = \hat{U}\Psi^{\text{lab}}(\mathbf{r}, t)$  one obtains:

$$\begin{aligned} i\frac{\partial}{\partial t}\Psi^{KH}(\mathbf{r}, t) &= i\frac{\partial}{\partial t}\hat{U}_1 \cdot \hat{U}_2\Psi^{\text{lab}}(\mathbf{r}, t) \\ &= i\left(\frac{\partial}{\partial t}\hat{U}_1\right)\hat{U}_2\Psi^{\text{lab}}(\mathbf{r}, t) + i\hat{U}_1\left(\frac{\partial}{\partial t}\hat{U}_2\right)\Psi^{\text{lab}}(\mathbf{r}, t) + i\hat{U}_1\hat{U}_2\frac{\partial}{\partial t}\Psi^{\text{lab}}(\mathbf{r}, t) \end{aligned}$$

Inserting the relations  $\frac{\partial}{\partial t}\hat{U}_1 = -\hat{U}_1 \cdot \frac{1}{c}\mathbf{A}\nabla$  and  $\frac{\partial}{\partial t}\hat{U}_2 = \hat{U}_2 \cdot \frac{i}{2c^2}\mathbf{A}^2$ , this evaluates to

$$i\frac{\partial}{\partial t}\Psi^{KH}(\mathbf{r}, t) = \hat{U}_1 \cdot \hat{U}_2 \left(-\frac{i}{c}\mathbf{A}\nabla\right)\Psi^{\text{lab}}(\mathbf{r}, t) + \hat{U}_1 \cdot \hat{U}_2 \left(\frac{1}{2c^2}\mathbf{A}^2\right)\Psi^{\text{lab}}(\mathbf{r}, t) + \hat{U}_1 \cdot \hat{U}_2 \cdot i\frac{\partial}{\partial t}\Psi^{\text{lab}}(\mathbf{r}, t) \quad (\text{C.2})$$

The Schrödinger equation in the laboratory frame can be written as (within the dipole approximation  $[\mathbf{A}, \nabla] = 0$ ):

$$i\frac{\partial}{\partial t}\Psi^{\text{lab}}(\mathbf{r}, t) = -\left(\frac{1}{2}\Delta - \frac{1}{ic}\mathbf{A} \cdot \nabla - \frac{1}{2c^2}\mathbf{A}^2\right)\Psi^{\text{lab}}(\mathbf{r}, t) + V(\mathbf{r})\Psi(\mathbf{r}, t)^{\text{lab}} \quad (\text{C.3})$$

Combining now Eq. (C.3) and Eq. (C.2) yields:

$$\begin{aligned} i\frac{\partial}{\partial t}\Psi^{KH}(\mathbf{r}, t) &= \hat{U} \left(-\frac{i}{c}\mathbf{A}\nabla + \frac{1}{2c^2}\mathbf{A}^2\right)\Psi^{\text{lab}}(\mathbf{r}, t) + \hat{U} \left[-\frac{1}{2}\Delta - \frac{1}{ic}\mathbf{A}\nabla - \frac{1}{2c^2}\mathbf{A}^2 + V(\mathbf{r})\right]\Psi^{\text{lab}}(\mathbf{r}, t) \\ &= \hat{U} \left[-\frac{1}{2}\Delta + V(\mathbf{r})\right]\Psi^{\text{lab}}(\mathbf{r}, t) \\ &= -\frac{1}{2}\Delta\hat{U}\Psi^{\text{lab}}(\mathbf{r}, t) + \hat{U}V(\mathbf{r})\Psi^{\text{lab}}(\mathbf{r}, t) \\ &= -\frac{1}{2}\Delta\Psi^{KH}(\mathbf{r}, t) + \hat{U}_1V(\mathbf{r})\hat{U}_2\Psi^{\text{lab}}(\mathbf{r}, t) \\ &= -\frac{1}{2}\Delta\Psi^{KH}(\mathbf{r}, t) + V(\mathbf{r} + \boldsymbol{\alpha})\hat{U}\Psi^{\text{lab}}(\mathbf{r}, t) \\ &= -\frac{1}{2}\Delta\Psi^{KH}(\mathbf{r}, t) + V(\mathbf{r} + \boldsymbol{\alpha})\Psi^{KH}(\mathbf{r}, t) \end{aligned} \quad (\text{C.4})$$

where the commutator relations  $[\hat{U}, \Delta] = 0$  and  $[\hat{U}_2, V(\mathbf{r})] = 0$  have been used, since  $\hat{U}_1$  is a translation operator and  $\hat{U}_2$  is independent of  $\mathbf{r}$ . Finally, we have shown that the transformed wave function  $\Psi^{KH}(\mathbf{r}, t)$  satisfies Eq. (3.45) in Chapter 3 which is the TDSE in the Kramers-Henneberger frame.

*C The Schrödinger equation in the Kramers-Henneberger coordinate frame*

## D Strong field approximation for 1D Coulomb ionization

In the following we present the calculation of the ionization spectrum for a bound state in the one-dimensional Coulomb potential using the SFA. Starting point is Eq. (2.30). The initial state (first bound odd wave function in the Coulomb potential with binding energy  $E = -0.5$  a.u.) is given by

$$\phi_i = \sqrt{2}x \exp(-|x|). \quad (\text{D.1})$$

The final state is a Volkov state

$$\phi_f = \frac{1}{2\pi} \exp(ikx) \exp\left(-i\frac{k^2}{2}t\right) \exp[i\delta(k, x, t)] \quad (\text{D.2})$$

with the Volkov phase

$$\delta(k, x, t) = -\frac{E_0}{\omega} \sin \omega t - \frac{E_0}{\omega^2} \cos \omega t x - \frac{1}{2} \frac{E_0^2}{\omega^2} \left( \frac{1}{2}t - \frac{1}{4\omega} \sin 2\omega t \right). \quad (\text{D.3})$$

For the derivation of Eq. (D.3) a linearly polarized laser pulse with a vanishing amplitude for  $t \rightarrow \pm\infty$  of the form

$$E(t) = E_0 \cos \omega t \quad (\text{D.4})$$

is assumed. Hence the interaction part of the full Hamiltonian is given by

$$V(t) = xE_0 \cos(\omega t). \quad (\text{D.5})$$

The transition probability amplitude depending on the final state with momentum  $k$  [cf. Eq. (2.30)]

$$p_{i \rightarrow f} = -i \int_{-\infty}^{\infty} dt \langle \phi_f | V(t) | \phi_i \rangle \quad (\text{D.6})$$

evaluates in spatial coordinate representation to

$$p_{i \rightarrow f} = -\frac{i}{\sqrt{2\pi}} \int_{-\infty}^{\infty} dt \Phi(t, k) \int_{-\infty}^{\infty} dx \exp\left(ikx + \frac{E_0}{\omega^2} x \cos \omega t\right) x^2 E_0 \exp(-|x|) \quad (\text{D.7})$$

with a function

$$\Phi(t, k) = \exp\left[i\frac{k^2}{2}t + i\frac{E_0}{\omega} \sin \omega t + i\frac{E_0^2}{2\omega^2} \left(\frac{1}{2}t - \frac{1}{4\omega} \sin 2\omega t\right)\right] \cos \omega t \quad (\text{D.8})$$

being independent of  $x$ .

The spatial integration in Eq. (D.7) can be performed analytically:

$$\begin{aligned} & \frac{E_0}{2\pi} \int_{-\infty}^{\infty} dx \exp\left(-ikx + \frac{E_0}{\omega^2} x \cos \omega t - |x|\right) \cdot x^2 \\ &= \frac{E_0}{2\pi} \int_0^{\infty} dx \exp(\gamma_1 x) \cdot x^2 + \int_{-\infty}^0 \exp(\gamma_2 x) \cdot x^2 \\ &= \frac{E_0}{\pi} \left( \frac{1}{\gamma_2^3} - \frac{2}{\gamma_1^3} \right) = \Xi(t, k) \end{aligned} \quad (\text{D.9})$$

### D Strong field approximation for 1D Coulomb ionization

with the functions

$$\gamma_1 = -ik + \frac{E_0}{\omega^2} \cos \omega t - 1 \quad \gamma_2 = -ik + \frac{E_0}{\omega^2} \cos \omega t + 1 . \quad (\text{D.10})$$

The whole expression simplifies to

$$p_{i \rightarrow f} = -i \int_{-\infty}^{\infty} dt \cos \omega t \exp \left\{ i \left[ \frac{k^2}{2} t + \frac{E_0}{\omega} \sin \omega t + \frac{E_0^2}{2\omega^2} \left( \frac{1}{2} t - \frac{1}{4\omega} \sin 2\omega t \right) \right] \right\} \cdot \Xi(t, k) . \quad (\text{D.11})$$

Eq. (D.11) is computed numerically within the region  $t \in [0, t_{max}]$  where the laser pulse is active. The absolute square of  $p_{i \rightarrow f}$  gives the total transition probability  $P_{i \rightarrow f} = |p_{i \rightarrow f}|^2$ .

## E Proof of the 1D-non-degeneracy theorem

Let  $E$  be a two-fold degenerate energy level in a potential  $V(x)$ . Thus, there exist two wave functions  $\psi_1$  and  $\psi_2$  which fulfill

$$-\frac{1}{2} \frac{d^2}{dx^2} \psi_1 + V(x)\psi_1 = E\psi_1 \quad \text{and} \quad (\text{E.1})$$

$$-\frac{1}{2} \frac{d^2}{dx^2} \psi_2 + V(x)\psi_2 = E\psi_2 . \quad (\text{E.2})$$

By multiplying Eq. (E.1) with  $\psi_2$  and Eq. (E.2) with  $\psi_1$  one obtains

$$-\psi_2 \frac{1}{2} \frac{d^2}{dx^2} \psi_1 + \psi_2 V(x)\psi_1 = \psi_2 E\psi_1 \quad \text{and} \quad (\text{E.3})$$

$$-\psi_1 \frac{1}{2} \frac{d^2}{dx^2} \psi_2 + \psi_1 V(x)\psi_2 = \psi_1 E\psi_2 . \quad (\text{E.4})$$

Subtracting Eq. (E.4) from Eq. (E.3) leads to

$$\psi_1 \frac{d^2}{dx^2} \psi_2 - \psi_2 \frac{d^2}{dx^2} \psi_1 = 0 . \quad (\text{E.5})$$

This can be written as

$$\frac{d}{dx} \left( \psi_2 \frac{d}{dx} \psi_1 - \psi_1 \frac{d}{dx} \psi_2 \right) = 0 . \quad (\text{E.6})$$

By integrating this equation one trivially finds that  $\psi_2 \frac{d}{dx} \psi_1 - \psi_1 \frac{d}{dx} \psi_2 = \text{constant}$ .

Since  $\lim_{x \rightarrow \infty} \psi_1 = 0$  and  $\lim_{x \rightarrow \infty} \psi_2 = 0$  hold, this constant has to be zero. Therefore, dividing by  $\psi_1 \psi_2$  in the non-zero region yields:

$$\frac{d\psi_1}{\psi_1} = \frac{d\psi_2}{\psi_2} \quad (\text{E.7})$$

Finally, the integration of this equation leads to  $\psi_1 = C\psi_2$ , where  $C$  is a constant. Therefore  $\psi_1$  and  $\psi_2$  are not independent and the 1D - system cannot be degenerate.

But for the 1D - Coulomb potential  $\psi_1 \psi_2$  is zero in the region of the singularity. Therefore Eq. (E.7) can only be integrated in the regions between the roots of the wave function and the proof is not valid for potentials with any singularity. Those systems can have degeneracies even in the one-dimensional case.

*E Proof of the 1D-non-degeneracy theorem*

# Bibliography

- [1] Albert Einstein. Über einen die Erzeugung und Verwandlung des Lichtes betreffenden heuristischen Gesichtspunkt. *Annalen der Physik* **17**, 132, 1905.
- [2] Max Planck. Über das Gesetz der Energieverteilung im Normalspectrum, 1900. *Verhandlungen der DGP 2*, p. 202 und p. 237, published for instance in M. Planck: “*Physikalische Abhandlungen und Vorträge, Bd I., S. 717-727, Vieweg und Sohn Braunschweig*, 1958.
- [3] T. Brabec and F. Krausz. Intense few-cycle laser fields: Frontiers of nonlinear optics. *Rev. of Mod. Phys.* **72**, No. 2, p. 545, 2000.
- [4] D.B. Milošević, G. G. Paulus, D. Bauer, and W. Becker. Above-threshold ionization by few-cycle pulses. *J. Phys. B* **39**, R203-R262, 2006.
- [5] A. Baltuška, Th. Udem, M. Uiberacker, M. Hentschel, E. Goulielmakis, Ch. Gohle, R. Holzwarth, V.S. Yakovlev, A. Scrinzi, T.W. Hänsch, and F. Krausz. Attosecond control of electronic processes by intense light fields. *Nature* **521**, p. 611, 2003.
- [6] M. Hentschel et al. Attosecond metrology. *Nature* **414**, p. 509, 2001.
- [7] E. E. Krasovskii and M. Bonitz. Spectral Line Shape Variations in Time-Resolved Photoemission from a Solid. *Phys. Rev. Lett.* **99**, 247601, 2007.
- [8] J. Mauritsson, P. Johnsson, E. Mansten, M. Swoboda, T. Ruchon, A. L’Huillier, and K. J. Schafer. Coherent Electron Scattering Captured by an Attosecond Quantum Stroboscope. *Phys. Rev. Lett.* **100**, 073003, 2008.
- [9] Michael Bauer. Femtosecond ultraviolet photoelectron spectroscopy of ultra-fast surface processes. *J. Phys. D: Appl. Phys.* **38** R253-R267, 2005.
- [10] H.-J. Kull and V. T. Tikhonchuk. Fast electrons from electron-ion collisions in strong laser fields. *Phys. Plas.* **12**, 063301, 2005.
- [11] J. Görlinger, H.-J. Kull, and V. T. Tikhonchuk. *Laser Physics* **15**, 245, 2005.
- [12] G. Rascol, H. Bachau, V. T. Tikhonchuk, H.-J. Kull, and T. Ristow. Quantum calculations of correlated electron-ion collisions in a strong laser field. *Phys. Plas.* **13**, 103108, 2006.
- [13] H. Haberland, M. Bonitz, and D. Kremp. Harmonics generation in electron-ion collisions in a short laser pulse. *Phys. Rev. E* **64**, 026405, 2001.
- [14] Thomas Katsouleas. Electrons hang ten on laser wake. *Nature* **431**, p.515-516, 2004.
- [15] Karsten Balzer. Nonequilibrium Green’s function approach to artificial atoms. *Diploma thesis, Kiel University*, 2007.
- [16] D. N. Fittinghoff, P. R. Bolton, B. Chang, and K. C. Kulander. Observation of nonsequential double ionization of helium with optical tunneling. *Phys. Rev. Lett.* **69**, 2642-2645, 1992.

## Bibliography

- [17] B. Walker, B. Sheehy, L. F. DiMauro, P. Agostini, K. J. Schafer, and K. C. Kulander. Precision Measurement of Strong Field Double Ionization of Helium. *Phys. Rev. Lett.* **73**, 1227-1230, Aug 1994.
- [18] L. V. Keldysh. Ionization in the field of a strong electromagnetic wave. *JETP* **20**, No. 5, 1965.
- [19] N.B. Delone and V.P. Krainov. *Atoms in Strong Light Fields*. Springer-Verlag, Berlin Heidelberg, 1985.
- [20] M. J. Nandor, M. A. Walker, and L. D. van Woerkom. Detailed comparison of above-threshold-ionization spectra from accurate numerical integrations and high-resolution measurements. *Phys. Rev. A* **60**, 1771, 1999.
- [21] N.B. Delone and V.P. Krainov. *Multiphoton Processes in Atoms*. Springer-Verlag, Berlin Heidelberg, 2000.
- [22] J. H. Eberly and J. Javanainen. Above-threshold ionization. *Physics Reports* **204** (5), p. 331-383, 1991.
- [23] Torsten Fliessbach. *Lehrbuch zur Theoretischen Physik II: Elektrodynamik*. Spektrum Akademischer Verlag, Berlin Heidelberg, 2000.
- [24] Diego G. Arbó, Jorge E. Miraglia, and María Silvia Gravielle. Coulomb-Volkov approximation for near-threshold ionization by short laser pulses. *Phys. Rev. A* **77**, 013401, 2008.
- [25] Claude Cohen-Tannoudji, Bernhard Diu, and Franck Laloë. *Quantenmechanik Teil 2*. Walter de Gruyter Berlin, New York, 1999.
- [26] Harald Friedrich. *Theoretische Atomphysik*. Springer-Verlag, Berlin Heidelberg, 1990.
- [27] Howard R. Reiss. Effect of an intense electromagnetic field on a weakly bound system. *Phys. Rev. A* **22**, 5, 1980.
- [28] F. H. M. Faisal. Multiple absorption of laser photons by atoms. *J. Phys. B: Atom. Molec. Phys.* **6**, L89, 1973.
- [29] Zhangjin Chen, Toru Morishita, Anh-Thu Le, M. Wichenhauser, X.M. Tong, and C.D. Lin. Analysis of two-dimensional photoelectron momentum spectra and the effect of the long-range Coulomb potential in single ionization of atoms by intense lasers. *Phys. Rev. A* **74**, 053405, 2006.
- [30] Jingtao Zhang and Takashi Nakajima. Coulomb effects in photoionization of H atoms irradiated by intense laser fields. *Phys. Rev. A* **75**, 043403, 2007.
- [31] N. L. Manakov, V.D. Ovsiannikov, and L.P. Rapoport. Atoms in a laser field. *Physics Reports* **141** (6), p. 319-433, 1986.
- [32] Timo Eirola, Ville Havu, Antti-Pekka Jauho, and Jan von Pfaler. Computational problems in physics 2005, Group Reports: Propagators for Quantum Systems. *Helsinki University of Technology, Institute of Mathematics Research Reports C018*, 2005.
- [33] W. Press, W. Vetterling, S. Teukolsky, and B. Flannery. *Numerical Recipes*. Cambridge University Press, 2002.

- [34] W. van Dijk and F. M. Toyama. Accurate numerical solutions of the time-dependent Schrödinger equation. *preprint arXiv:physics/0701150v1*, 2007.
- [35] K. Boucke, H. Schmitz, and H.-J. Kull. Radiation conditions for the time-dependent Schrödinger equation: Application to strong-field photoionization. *Phys. Rev. A* **56**, 763, 1997.
- [36] D. Bauer and P. Koval. QPROP: A Schrödinger-solver for intense-laser atom interaction. *Comp. Phys. Comm.* **174**, 396-421, 2005.
- [37] D. Neuhauser and M. Baer. The time-dependent Schrödinger equation: Application of absorbing boundary conditions. *Journal of Chemical Physics* **90** p. 4351-4355, 1989.
- [38] A. Vibok and G. G. Balint-Kurti. Parametrization of Complex Absorbing Potentials for Time-Dependent Quantum Dynamics. *Journal of Physical Chemistry* **96**, p. 8712-8719, 1992.
- [39] Xue-Shen Liu, Xiao-Yan Liu, Zhong-Yuan Zhou, Pei-Zhu Ding, and Shou-Fu Pan. Numerical solution of one-dimensional time-independent Schrödinger equation by using symplectic schemes. *Int. Journal of Quantum Chemistry* **79**, 343-349, 2000.
- [40] Walter C. Henneberger. Perturbation method for atoms in intense light beams. *Phys. Rev. Lett.* **21**, 838, 1968.
- [41] H. A. Kramers. Collected scientific papers. *Amsterdam: North-Holland* p. 866, 1956.
- [42] V. C. Reed and K. Burnett. Harmonic generation in the Kramers-Henneberger stabilization regime. *Phys. Rev. A* **47** No. 1, 1993.
- [43] Sebastian Bauch and Michael Bonitz. Quantenmechanische Bewegung von Teilchen in äußeren Feldern. *Educational Poster for Max Planck Anniversary*, 2007.
- [44] Sebastian Bauch. Motion of gaussian wave packets. *Personal note on scattering on Gaussian wells and steps to compare with tomographic methods from Prof. V. Filinov (Moscow). Both methods show very good agreement.*, 2007.
- [45] Claude Cohen-Tannoudji, Bernhard Diu, and Franck Laloë. *Quantenmechanik Teil 1*. Walter de Gruyter Berlin, New York, 1999.
- [46] R. Loudon. One-Dimensional Hydrogen Atom. *Am. J. Phys.* **27**, 649, 1959.
- [47] Charles E. Mortimer and Ulrich Müller. *Chemie*. Thieme Verlag, Stuttgart, 2003.
- [48] J. H. D. Eland. *Photoelectron Spectroscopy - An introduction to ultraviolet photoelectron spectroscopy in the gas phase*. Butterworths, London, 1974.
- [49] Sebastian Bauch and Michael Bonitz. Angle-resolved multi-photon ionization. *to be published*, 2008.
- [50] Sebastian Bauch and Michael Bonitz. Coulomb scattering in strong laser fields. *Poster for the DPG Meeting "Amop" in Düsseldorf*, 2007.
- [51] Sebastian Bauch and Michael Bonitz. Coulomb scattering and ionization in strong laser fields. *Poster for the DPG Meeting "Amop" in Darmstadt*, 2008.

## Bibliography

- [52] Sebastian Bauch and Michael Bonitz. Fast electron generation by Coulomb scattering on spatially correlated ions in a strong laser field. *to be published*, 2008.
- [53] Torsten Fliessbach. *Lehrbuch zur Theoretischen Physik I: Mechanik*. Spektrum Akademischer Verlag, Berlin Heidelberg, 2003.
- [54] Earl W. McDaniel. *Atomic Collisions: Electron and Photon Projectiles*. John Wiley and Sons, New York, 1989.
- [55] Wolfgang Demtröder. *Experimentalphysik 2 - Elektrizität und Optik*. Springer-Verlag, Berlin Heidelberg, 1999.
- [56] Lutz Kipp. Proposal of an experiment during the discussion of the present thesis.
- [57] Michael Romanovsky. Remark, while discussing the spectra of correlated electron-ion collisions.
- [58] Yuri Lozovik. Proposal of a possible microscopic setup for correlated collisions of electrons to resolve high energies during the presentation of the results obtained within this work.

## Acknowledgements

First of all I have to thank my supervisor, Prof. Dr. Michael Bonitz, who is a very committed person in teaching as well as in research. It is due to his personal activity that I was introduced to actual research issues early during my university education. Especially the possibility to work on a subject unaffiliated, but of course with profound helpful comments, gave me the opportunity to acquire the ability for independent scientific work.

Furthermore I express thanks to several persons with whom I talked about the present thesis. During these discussions a lot of ideas arose. Especially, Prof. Dr. Lutz Kipp and Prof. Dr. Michael Bauer, both at the institute for experimental and applied physics (IEAP) at the CAU Kiel and Prof. Dr. H.-J. Kull, RWTH Aachen, should be mentioned.

I also have to thank the whole work group for a nice and helpful working atmosphere with lots of discussions — on physical issues, but also on many other subjects. A considerable part in the final realization of this work belongs to Karsten Balzer for lots of discussions on physics, Jens Böning for his profound Latex and Gnu-plot knowledge, Thorben Ott, Hanno Kählert and David Hochstuhl for their patience in reading the manuscript of this work and Patrick Ludwig who accompanied me in spending long evenings and weekends in the office.

Finally, many thanks belong to my family and my girlfriend Eva.

## Eidesstattliche Erklärung

Die vorliegende Arbeit ist von mir selbständig und nur unter Zuhilfenahme der angegebenen Quellen und Hilfsmittel angefertigt worden.

---

*(Ort, Datum)*

---

*(Unterschrift)*